Ore formation during Jurassic subduction of the Tethys along the Eurasian margin: Constraints from the Kapan district, Lesser Caucasus, southern Armenia

Johannes Mederer[a 1 2], Robert Moritz[a], Massimo Chiaradia[a], Richard Spikings[a], Jorge E. Spangenberg[b], David Selby[c,d],

[a]*Department of Earth Sciences, University of Geneva, Rue des Maraîchers 13, 1205 Geneva, Switzerland*

[b]*Institute of Earth Surface Dynamics, University of Lausanne, Géoopolis, 1015 Lausanne, Switzerland*

[c]*Department of Earth Sciences, Durham University, Durham DH1 3LE, UK*

[d]*State Key Laboratory of Geological Processes and Mineral Resources, School of Earth Resources, China University of Geosciences, Wuhan, China, 430074*

Abstract

The Kapan mining district in the southernmost Lesser Caucasus is one of the unique locations along the Central metallogenic Tethyan belt where ore-forming processes were associated with magmatic arc growth during Jurassic Neotethys subduction along the Eurasian margin. Three ore deposits of the Kapan district were investigated in this study, including Centralni West, Centralni East and Shahumyan. The ore deposits are hosted by Middle Jurassic andesitic to dacitic volcanic and volcaniclastic rocks of tholeiitic to transitional affinities below a late Oxfordian unconformity, which is covered by calc-alkaline to transitional Late Jurassic-Early Cretaceous volcanic rocks interlayered with sedimentary rocks.

The mineralization consists of veins, subsidiary stockwork and partial matrix-replacement of breccia host rocks, with chalcopyrite, pyrite, tennantite-tetrahedrite, sphalerite and galena as the main ore minerals. Centralni West is a dominantly Cu deposit, and its host rocks are altered to chlorite, carbonate, epidote and sericite. At Centralni East, Au is associated with Cu, and the Shahumyan deposit is enriched in Pb and Zn as well as precious metals. Both deposits contain high-sulfidation state mineral assemblages with enargite and luzonite. Dickite, sericite and diaspore prevail in altered host rocks in the Centralni East deposit. At the Shahumyan deposit, phyllic to argillic alteration with sericite, quartz, pyrite and dickite is dominant along polymetallic veins, and advanced argillic alteration with residual quartz is locally developed.

The lead isotopic composition of sulfides and alunite ($^{206}Pb/^{204}Pb$ = 18.17-18.32, $^{207}Pb/^{204}Pb$ = 15.57-15.61, $^{208}Pb/^{204}Pb$ = 38.17 - 38.41) indicates a common metal source for the three deposits, and suggests that metals were derived from magmatic fluids that were exsolved upon crystallization of Middle Jurassic intrusive rocks or leached from Middle Jurassic country rocks. The $\delta^{18}O$ values of hydrothermal quartz (8.3 to 16.4‰) and the $\delta^{34}S$ values of sulfides (2.0 to 6.5‰) reveal a dominantly magmatic source at all three deposits. Combined oxygen, carbon and strontium isotopic compositions of hydrothermal calcite ($\delta^{18}O$ = 7.7 to 15.4‰, $\delta^{13}C$ = -3.4 to 0.7‰, $^{87}Sr/^{86}Sr$ = 0.70537

[1] Corresponding author: e-mail johannes.mederer@lafargeholcim.com

[2] Current address: Reserves and Mining, LafargeHolcim, Switzerland, Tel.: + 41 79 651 6414

to 0.70586) support mixing of magmatic-derived fluids with seawater during the last stages of ore formation at Shahumyan and Centralni West.

$^{40}Ar/^{39}Ar$ dating of hydrothermal muscovite at Centralni West and of magmatic-hydrothermal alunite at Shahumyan yield, respectively, a robust plateau age of 161.78±0.79 Ma and a disturbed plateau age of 156.14±0.79 Ma. Re-Os dating of pyrite from the Centralni East deposit yields an isochron age of 144.7±4.2 Ma, and a weighted average age of the model dates of 146.2±3.4 Ma, which are younger than the age of the immediate host rocks. Two different models are offered depending on the reliability attributed to the disturbed $^{40}Ar/^{39}Ar$ alunite age and the young Re-Os age. The preferred interpretation is that the Centralni West Cu deposit is a volcanogenic massive sulfide deposit, and that the Shahumyan and Centralni East deposits are parts of porphyry-epithermal systems, the three deposits being broadly coeval or being formed within a short time interval in a nascent magmatic arc setting, before the late Oxfordian. Alternatively, but less likely, the three deposits could represent different mineralization styles successively emplaced during evolution and growth of a magmatic arc during a longer time frame between the Middle and Late Jurassic.

Introduction

The Lesser Caucasus is a segment of the Tethys belt (Jankovic, 1977, 1997; Richards, 2015) that records a complex geological evolution from the Jurassic to the Cenozoic, including several subduction, accretion and collision events (Golonka, 2004; Adamia et al., 2011; Cowgill et al., 2016; Rolland, 2017). Ore deposits were formed during its entire geodynamic evolution (Moritz et al., 2016a). The Lesser Caucasus is one of the unique locations along the Central Tethyan belt, which offers the possibility to study ore deposits formed during the early stages of magmatic arc construction related to Neotethys subduction along the Eurasian margin. Indeed, a limited number of ore deposits and prospects are hosted by Middle to Late Jurassic volcano-sedimentary sequences of the Lesser Caucasus at the Alaverdi and the Kapan mining districts (Fig. 1; Maghakyan, 1954; Khachaturyan, 1977; Achikgiozyan et al., 1987; Zohrabyan and Melkonyan, 1999; Kekelia et al., 2004; Calder, 2014; Mederer et al., 2014).

The Kapan mining district of the southernmost Lesser Caucasus hosts several important past-producing base metal mines at Centralni West (formerly known as 7-10 and Katar mines) and Centralni East (formerly named 1-2, 6 and Kavart mines), and one active mine at the Shahumyan precious and base metal deposit (Figs. 2 and 3; Table 1). Industrial mining in the Kapan district dates back to the Mid-19th century and different state and private companies have been operating the deposits since then. Reliable production records are not available and have to be estimated. Considering all available data, at least 370,000 tons of Cu have been mined in the Kapan district since 1953 (Wolfe and Gossage, 2009). Production in the open pit and underground workings of Centralni East ceased in 2005 and the Centralni West underground operation closed in 2008. The underground Shahumyan deposit remains the only active mine in the district (Table 1). In 2016, about 290,000 t of ore were processed, producing a total amount of 13.7 Koz of Au, 0.3 Moz of Ag, 615 t of Cu and 2,888 t of Zn. The measured, indicated and inferred resources of the Shahumyan deposit were estimated at 15.0 Mt at 2.7 ppm Au, 48 ppm Ag and 0.5% Cu by Polymetal International

(2017). Because of ongoing exploration and underground exploitation, the Shahumyan polymetallic deposit is more accessible and has been more systematically studied and sampled during this study.

Ore deposits hosted by Middle Jurassic rocks in the Kapan district consist of Cu-enriched massive pyrite bodies, and Cu-Au and polymetallic stratiform, vein-type and stockwork type mineralization, which have been variably interpreted as volcanogenic massive sulfide (VMS) and porphyry-epithermal ore systems (Schmidt et al., 1985; Moon et al., 2001; Kekelia et al., 2004; Wolfe and Gossage, 2009; Mederer et al., 2014). In this contribution we provide new constraints to discuss these genetic controversies for the Kapan district. We present, new descriptions of the geological setting, the hydrothermal alteration and mineralization features of the Centralni West, Centralni East and Shahumyan deposits. This data is discussed with new radiogenic (Pb, Sr) and stable isotope (O, C, S, H) data obtained for various gangue and ore minerals to evaluate the sources of metals and the nature of the fluids involved in the genesis of the different deposits. In the final part of this contribution, we discuss new $^{40}Ar/^{39}Ar$ and Re-Os dates of hydrothermal gangue and opaque minerals, and evaluate them with respect to the regional geological framework, crosscutting relationships, and previously published U-Pb geochronological data obtained for magmatic rocks (Mederer et al., 2013). The combined dataset strongly suggests that the different deposits were formed within a short time frame or were broadly coeval during Middle Jurassic magmatic arc construction.

Geodynamic and Geologic Setting of the Lesser Caucasus

The Lesser Caucasus is a segment of the Tethyan orogenic belt (Fig. 1) that was formed during north- to northeast-verging Jurassic-Cretaceous subduction of the Neotethys beneath Eurasia (Adamia et al., 1977; Kazmin et al., 1986; Rolland et al., 2011), followed by Late Cretaceous collision with the Gondwana-derived South Armenian block (Rolland et al., 2009a). Subsequent east-verging Neotethys subduction during final Cenozoic convergence of Eurasia and Arabia was accompanied by an Eocene magmatic maximum, and followed by collisional to post-collisional Oligocene to Pliocene magmatism (Khain, 1975; Kazmin et al., 1986; Lordkipanidze et al., 1989; Moritz et al., 2016b; Rezeau et al., 2016, 2017).

The Lesser Caucasus consists of three main tectonic elements (Fig. 1), including from east to west: the Eurasian plate margin, the Amasia-Sevan-Akera suture zone, and the South Armenian block (Adamia et al., 1977, 2011; Sosson et al., 2010). The Eurasian plate margin of the Lesser Caucasus is also known as the Transcaucasian microcontinent, and consists of the ~350 km-long Somkheto-Karabakh belt and the ~70 km-long Kapan block (Figs. 1 and 2; Gevorkyan and Aslanyan, 1997; Mederer et al., 2013). Both tectonic zones have similar geologic and tectonic characteristics and are interpreted as a discontinuous Jurassic to Cretaceous island-arc that formed during Neotethyan subduction (Sosson et al., 2010; Adamia et al., 2011), segmented by roughly east-west striking strike-slip faults (Kazmin et al., 1986; Gabrielyan et al. 1989; Fig. 1). Neoproterozoic to Paleozoic basement rocks are exposed in the northern Somkheto-Karabakh range in the Loki, Khrami, Dzirula, and Akhum-Asrikchai massifs (Bagdasaryan et al., 1978; Shengelia et al., 2006;

Zakariadze et al., 2007; Mayringer et al., 2011). Pulsed volcanic arc activity took place during the Bajocian-Bathonian and the Kimmeridgian (Kazmin et al., 1986; Achikgiozyan et al. 1987; Lordkipanidze et al., 1989; Mederer et al., 2013), which was followed by uplift and denudation during the Early Cretaceous (Sosson et al., 2010), and deposition of Late Cretaceous and Paleogene sedimentary and volcanic rocks (Aslanyan, 1958; Achikgiozyan et al. 1987).

The suture zone between the Eurasian Somkheto-Karabakh belt and the Gondwana-derived South Armenian block is outlined by the Amasia-Sevan-Akera ophiolite zone (Fig. 1; Galoyan et al., 2009; Rolland et al., 2010; Hässig et al., 2013a, b). Obduction of the ophiolites occurred between 88 and 83 Ma (Galoyan et al., 2007; Rolland et al., 2010), and final Eurasian - South Armenian block collision took place at 73-71 Ma (Rolland et al., 2009a, b). In the southernmost Lesser Caucasus, the northwest-trending, dextral strike-slip Khustup-Giratakh fault constitutes the tectonic boundary between the Eurasian Kapan block and the Gondwana-derived South Armenian block (Fig. 2). The Khustup-Giratakh fault includes ultramafic rock, gabbro, spilite, andesite and radiolarite of the Zangezur tectonic mélange interpreted as ophiolite remains (Knipper and Khain, 1980; Burtman, 1994), which are imbricated with Late Precambrian to Early Cambrian metamorphic rocks and Devonian and Permian limestone and terrigenous rocks (Belov, 1969; Khain, 1975).

The Gondwana-derived South Armenian block is mainly exposed in southwestern Armenia, Nakhitchevan and the Tsaghkuniats massif, north of Yerevan (Fig. 1; Kazmin et al., 1986; Shengelia et al., 2006; Sosson et al., 2010; Hässig et al., 2015). The South Armenian block consists of Proterozoic metamorphic basement rocks, and an incomplete succession of Devonian to Jurassic sedimentary and volcanogenic rocks, unconformably covered by Cretaceous to Cenozoic sedimentary and volcanic rocks (Belov, 1968; Djrbashyan et al., 1976; Tayan et al., 1976; Sosson et al., 2010), and intruded by Cenozoic plutons along the accretion zone with the Eurasian margin (Moritz et al., 2016b; Rezeau et al., 2016, 2017; Grosjean et al., 2018; see for instance Fig. 2).

Metallogenic Evolution of the Lesser Caucasus

The metallogenic evolution of the Lesser Caucasus and the formation of its diverse inventory of ore deposits were influenced by the complex geodynamic processes of the Central Tethys belt (Moritz et al., 2016a). The initial metallogenic evolution of the Lesser Caucasus is related to the Jurassic-Cretaceous subduction of the Tethys along the Eurasian margin (Mederer et al., 2014; Moritz et al., 2016a). Copper-enriched massive pyrite, Cu-Au and polymetallic stratiform, vein-type and stockwork ore bodies are hosted by Middle Jurassic volcanic and volcano-sedimentary rocks in the Alaverdi, Mehmana and Kapan mining districts (Fig. 1), which are the topic of this contribution. Early Cretaceous porphyry Cu and precious metal epithermal deposits (Moritz et al., 2016a) were emplaced along the Somkheto-Karabakh belt at Teghout (Fig. 1; Amiryan et al., 1987; Calder, 2014), at Gedabek, Gosha and Chovdar (Fig.1; Babazadeh et al., 1990; Hemon et al., 2012), and in the Kapan block at the Shikahogh prospect (Fig. 2; Achikgiozyan et al., 1987). The youngest metallogenic event associated with subduction along the Somkheto-Karabakh belt includes base and

precious metal epithermal deposits and prospects with ambiguous VMS and porphyry relationships of the Bolnisi district hosted by Late Cretaceous volcano-sedimentary rocks (Fig. 1; Gugushvili, 2004; Migineishvili, 2005; Popkhadze et al., 2014). The latter district extends to the west into the Turkish Eastern Pontides, which hosts VMS and porphyry-epithermal systems (Fig. 1; Kekelia et al., 2004; Yigit, 2009; Delibaş et al., 2016). By contrast, the Mesozoic metallogenic belt of the Lesser Caucasus does not extend to the south into Iran (Moritz et al., 2016a), where the NE-oriented Araks fault constitutes a regional stratigraphic and structural limit between the Iranian Alborz and the Lesser Caucasus (Figs. 1 and 2; Sosson et al., 2010).

During the Cenozoic, ore deposit formation was associated with subduction to post-collisional magmatism in the South Armenian block and was spatially associated with the accretionary zone along the Eurasian margin (Moritz et al., 2016a). Important ore mineral centers include the Zod-Sotk (Kozerenko, 2004; Levitan, 2008), Amulsar (Lydian International, 2017) and Meghradzor (Amiryan and Karapetyan, 1964) epithermal gold deposits, and the Hanqavan Cu-Mo prospect (Fig. 1). The most prolific Cenozoic ore deposit cluster is located in the Meghri-Ordubad district of the southernmost Lesser Caucasus (Figs. 1 and 2), where porphyry Cu-Mo deposits and subsidiary epithermal prospects are hosted by the composite Meghri-Ordubad and Bargushat plutons (Karamyan, 1978; Amiryan, 1984; Babazadeh et al., 1990; Moritz et al., 2016b; Rezeau et al., 2016). The Cenozoic Lesser Caucasian ore deposit belt extends to the south into the Alborz and Urumieh-Dokhtar belts of Iran (Fig. 1; e.g., Richards et al., 2006; Daliran, 2008; Aghazadeh et al., 2015; Hassanpour et al., 2015; Mehrabi et al., 2016; Simmonds et al., 2017).

Geological Setting of the Kapan Block

The Kapan district (39°13'N, 46°24'E) is situated in south Armenia,~200 km southeast of Yerevan at an altitude of 800 to 1500 m (Figs. 2 and 3). It forms part of the tectonomagmatic Kapan Zone, which extends about 70 km in a NNW-SSE direction from southern Armenia into northern Iran. Four geological units are distinguished in the Kapan district: the Middle Jurassic, Late Jurassic-Early Cretaceous and Paleogene magmatic complexes, overlain by Quaternary basanite flows (Fig. 4). Each complex consists of coherent lava flows, intrusive rocks, autoclastic, hyaloclastic, pyroclastic and sedimentary deposits with lateral facies variation (Achikgiozyan et al., 1987; Mederer et al., 2013). Together they constitute an almost 6500 meter thick pile of volcanic and volcaniclastic rocks, calcareous sedimentary rocks and limestone (Fig. 4). A similar stratigraphic division was proposed as a working model for mineral exploration (Wood et al., 2008), in which Late Cretaceous limestone and sequences A, B and C are distinguished. Sequences B and C comprise rocks from the Middle Jurassic magmatic complex of Achikgiozyan et al. (1987), whereas Sequence A refers to the covering rocks from the Late Jurassic-Early Cretaceous magmatic complex. An absolute stratigraphic reference is missing in this model, therefore we prefer the better-documented stratigraphic division by Achikgiozyan et al. (1987) outlined above.

The oldest rocks in the Kapan district consist of an approximately 1000 m-thick sequence of Bajocian to Bathonian volcanogenic and volcanosedimentary rocks, with a dominantly andesitic to

dacitic and subsidiary basaltic to rhyolitic composition (Akopyan, 1962; Achikgiozyan et al., 1987; Mederer et al., 2013). No older basement rocks are cropping out in the Kapan district. The dominant lithofacies in the lower part of the Middle Jurassic sequence are lava flows, brecciated lava, hyaloclastite, ignimbrite and tuff. Widespread amygdaloidal and porphyritic textures, and subsidiary pillow lava structures are described by Achikgiozyan et al. (1987). District-wide epidote alteration is characteristic for the base of the Jurassic section and becomes less intensive towards the upper part of the Middle Jurassic magmatic complex. Both subaqueous and subaerial deposited tuff, ignimbrite and lava flows as well as hyaloclastite with andesitic to dacitic composition are characteristic for the upper part of the Middle Jurassic magmatic complex (Cholahyan and Sarkisyan, 1972; Achikgiozyan et al., 1987). A dominantly subvolcanic quartz-dacite that yielded a K-Ar age of 162±5 Ma (Sarkisyan, 1970) and referred to as Barabatoom Formation (Fig. 3), crosscuts Bathonian units, and also contains hyaloclastite and lava flows interlayered with ash fall deposits (Zohrabyan, 2005). Callovian tuff, limestone and calcareous rocks unconformably cover Bathonian and Bajocian rocks (Achikgiozyan et al., 1987; Zohrabyan, 2005). Gabbro-diorite bodies were intersected by drill holes at a depth of 390 m below the town of Kapan (Tumanyan, 1992). Rounded tonalite fragments from polymict pebble dikes hosted by Middle Jurassic rocks have a U-Pb zircon age of 165.6±1.4 Ma (Mederer et al., 2013). Based on their geochemical composition, the Middle Jurassic magmatic rocks were generated in a subduction environment (Mederer et al., 2013), and have a predominantly tholeiitic to transitional affinity (Fig. 5).

The Middle Jurassic magmatic complex was partially eroded and unconformably covered by rocks of the Late Jurassic-Early Cretaceous magmatic complex (Fig. 4). Late Oxfordian to Late Aptian basaltic, andesitic and dacitic tuff, hyaloclastite, brecciated lava and lava flows are interlayered with fossil-bearing calcareous sandstone and limestone units (Akopyan, 1962; Achikgiozyan et al., 1987), and were intruded by Early Cretaceous granodiorite, quartz-monzodiorite, gabbro, diorite, granodiorite, monzonite and granite, with U-Pb zircon ages ranging between 139 and 128 Ma (Mederer et al., 2013, Melkonyan et al., 2016). Abundant steeply dipping north- and southeast-oriented diabase dikes crosscut Middle Jurassic rocks, and are traced across the unconformity between the Middle Jurassic and Late Jurassic-Early Cretaceous magmatic complexes. Therefore, they are attributed to the Late Jurassic-Early Cretaceous magmatic complex. The thickness of dikes generally ranges between 0.5 and 3 m, but can reach up to 20 m. Plagioclase and clinopyroxene phenocrysts occur within the fine-grained matrix of diabase dikes. The Late Jurassic to Early Cretaceous magmatic rocks were also linked to subduction (Mederer et al., 2013), but in contrast to the Middle Jurassic rocks, they have a mostly calc-alkaline to partly transitional composition (Fig. 5), likely reflecting magmatic arc growth. The Late Jurassic to Early Cretaceous magmatic rocks have more primitive Sr and Nd isotopic compositions compared to the Late Jurassic magmatic rocks, which was interpreted as asthenospheric mantle upwelling as a consequence of slab roll-back during the younger magmatic arc evolution (Mederer et al., 2013).

Paleogene andesitic to rhyolitic brecciated lava, lava flows, tuff and ignimbrite with interlayered Eocene limestone dominate in the western part of the Kapan zone, where they unconformably overlie the Late Jurassic-Early Cretaceous magmatic complex. Subsidiary gabbroic and

monzogabbroic intrusions are emplaced within the Paleogene magmatic complex. One gabbro has a U-Pb zircon age of 50.8±0.5 Ma (Mederer et al., 2013), and is coeval with the beginning of Eocene magmatic activity recorded in the composite Meghri-Ordubad pluton of the adjacent South Armenian block (Fig. 2; Moritz et al., 2016b; Rezeau et al., 2016). The youngest magmatic event of the Kapan zone consists of columnar-jointed Quaternary basanite flows (Fig. 3).

Recent structural studies in the Kapan district (Davis, 2006; Wood et al., 2008) revealed a complex deformational history with repeated reactivation of preexisting faults. Bedding is well preserved in the volcano-sedimentary and volcanic sequence of the Late Jurassic-Early Cretaceous magmatic complex, but is difficult to trace in the Middle Jurassic magmatic complex, where lateral facies variation impedes the definition of stratigraphic marker horizons. Where observable, the flat lying beds dip preferentially towards the north-northeast, whereas in the southwestern part of the district bedding preferentially dips towards the west. Steeply dipping east-west striking extensional faults are the predominant structures in the Middle Jurassic magmatic complex. They formed early during the deformational history and are the host to mineralized veins in the Kapan district. Kinematic indicators on moderately northeastwards dipping thrust faults indicate a top to the west displacement. Thrusting typically occurred along the contact between the Middle and Late Jurassic-Early Cretaceous magmatic complexes, but also within the Middle Jurassic sequence (Fig. 6a). These faults define the large-scale duplex-style geometry and control stratigraphic repetition in the district (Wood et al., 2008). Late north-south-oriented and steeply dipping normal faults and northwest-oriented strike-slip faults crosscut the thrust faults and the mineralized east-west striking extensional faults.

Mineralization in the Kapan District

Economic mineralization in the Kapan district consists of Cu-, Cu±Au, polymetallic and precious metal vein- and stockwork type deposits hosted by the Middle Jurassic magmatic complex. The most important ore deposits are the Centralni West Cu deposit, the Centralni East Cu-Au deposit and the Shahumyan polymetallic Cu-Au-Ag-Zn±Pb deposit (Figs. 3-4 and 6a, b; Table 1). Several other ore occurrences and minor deposits have been exploited during the last two centuries in the Kapan district, but many of the old underground workings are not accessible anymore.

Local hydrothermal alteration and sulfide veining are also hosted by the Late Jurassic-Early Cretaceous and Paleogene magmatic complexes. Polymetallic vein-type mineralization at the Bartsravan exploration project, 25 km northwest of Kapan, is hosted by volcanic and subvolcanic rocks (Figs. 2 and 4; Zohrabyan et al. 2003), and stockwork-type Cu-Au-Mo mineralization at the Shikahogh prospect, 20 km south of Kapan, occurs at the contact of the Early Cretaceous Tsav intrusion within Late Jurassic and Early Cretaceous rocks (Figs. 2 and 4; Achikgiozyan et al., 1987).

The Centralni West Cu deposit

The Centralni West Cu deposit is situated in the western part of the Kapan district (Fig. 3). Mineralization is hosted by Middle Jurassic brecciated lava, bedded hyaloclastite and lava flows of basaltic to andesitic composition (Fig. 4). East-west-oriented and steeply south-dipping veins (60° to

80°) are the dominant mineralization style in the deposit (Fig. 7a). The matrix of the brecciated lava host rock consists in places of ore and gangue minerals (Fig. 7b). Hydraulic breccia textures with fragmented pyrite are typical in individual veins, which generally show an extensional character with unstrained margins and sulfide and gangue mineral growth perpendicular to the host rock walls. Wood et al. (2008) described one vein with a 10° to 20° dip towards the south, with shear fabrics and kinematic thrust fault indicators along its margins. The main ore minerals of the intermediate-sulfidation state assemblage are chalcopyrite and pyrite, with minor sphalerite, tennantite-tetrahedrite and galena (Fig. 7c). Trace minerals include marcasite, tellurobismuthite (Bi_2Te_3), hessite (Ag_2Te), petzite (Ag_3AuTe_2), tetradymite (Bi_2Te_2S), wittichenite (Cu_3BiS_3), emplectite ($CuBiS_2$) and native gold (Achikgiozyan et al., 1987). The host rock adjacent to mineralization in the Centralni West deposit is pervasively altered to chlorite, carbonate and epidote (Fig. 7d), and sericite/muscovite occurs in proximity to mineralization and in the shallow parts of the deposit. High-grade veins with up to 10 wt. % Cu and replacement type mineralization in brecciated host rocks are characterized by similar ore and gangue minerals, which support a common origin.

The Centralni East Cu-Au deposit

The Centralni East Cu-Au deposit is situated in the central part of the Kapan district (Fig. 3). Towards the west and south, the deposit is limited by gypsum-bearing faults, whereas an andesitic dike limits mineralization towards the east (Beaumont, 2006). The dominant mineralization style in the upper part of the Centralni East deposit is of stockwork-type (Fig. 8a) that changes with depth to roughly east-west-oriented veins, which dip between 65° and 85° to the south. Silicification, residual quartz alteration and phyllic alteration with sericite, dickite and diaspore as typical alteration minerals affect the andesitic to dacitic host rocks. Vein-type ore bodies dominate over stockwork-style mineralization with increasing depth (Achikgiozyan et al., 1987). An intermediate- to high-sulfidation state mineral paragenesis is characteristic for the Centralni East deposit, including pyrite, colusite ($Cu_{12}VAs_3S_{16}$), tennantite-tetrahedrite, chalcopyrite and specular hematite as main ore minerals, and minor luzonite and galena (Fig. 8b, c). Enargite, bornite, sphalerite, covellite, renierite ($(Cu,Zn)_{11}(Ge,As)_2Fe_4S_{16}$), germanite ($Cu_{26}Ge_4Fe_4S_{32}$) and minor native silver and tellurides have been described (Achikgiozyan et al. 1987). Quartz is the dominant gangue mineral with minor barite and gypsum. Clast-supported breccia with angular fragments of argillically altered and silicified dacite within a matrix of fine-grained quartz, gypsum, pyrite, hematite, minor sphalerite, chalcopyrite and native gold (up to 20 μm) have been reported from waste dump samples of the Centralni East deposit (Beaumont, 2006).

The Shahumyan polymetallic Cu-Au-Ag-Zn±Pb deposit

The Shahumyan polymetallic Cu-Au-Ag-Zn±Pb deposit is situated in the eastern part of the Kapan district (Fig. 3). Mineralization is hosted by the dominantly porphyritic subvolcanic quartz-dacite of the Middle Jurassic Barabatoom Formation that also consists of hyaloclastite and lava flows interlayered with ash fall deposits. The quartz-dacite contains abundant, up to 5 cm-sized,

plagioclase, amphibole and bipyramidal quartz phenocrysts. More than 100 steeply north- and south-dipping (75° - 85°) east-west-oriented veins (Fig. 6b) occur within an area of about 1.5 x 2.5 km^2. Individual veins can be traced for up to several hundred meters along strike with a vertical extent generally between 100 and 400 m. The extensional veins with unstrained margins and gangue and ore mineral orientation perpendicular to the vein walls are outcropping at surface and are cut by the Late Jurassic-Early Cretaceous magmatic complex that overlies Middle Jurassic rocks. The veins are generally zoned with an early barren quartz-pyrite stage, rimmed by a polymetallic stage and filled by a late carbonate stage (Fig. 9a). The host rock is affected by hydrothermal brecciation with clasts cemented by ore and gangue minerals (Fig. 9b). In other places, pseudo-breccia is developed with alteration along micro-fractures (Fig. 9b). The thickness of the veins varies from about 1 cm to several meters with an average width between 0.7 and 1.5 m.

The mineral assemblage in the Shahumyan deposit is typical of an intermediate-sulfidation state fluid composition, with pyrite, chalcopyrite, sphalerite, tennantite-tetrahedrite and galena being the most abundant ore minerals (Fig. 9c). Minor arsenopyrite is associated with the late carbonate stage. Minerals of higher sulfidation state fluid composition, such as enargite, digenite, bornite and chalcocite occur as up to 40 µm-sized inclusions in pyrite (Fig. 9d). The occurrence of gold and silver is controlled by Au-Ag tellurides, including calaverite ($AuTe_2$), krennerite ($(Au_{0.8}Ag_{0.2})Te_2$), sylvanite ($AuAgTe_4$), petzite (Ag_3AuTe_2) and hessite (Ag_2Te). Altaite (PbTe) is common and native tellurium can be found as inclusions in pyrite. Coloradoite (HgTe) was described by Matveev et al. (2006), and Achikgiozyan et al. (1987) reported native gold. Tellurides are observed as droplet-shaped inclusions in virtually sulfide-free quartz-veins, where telluride deposition is associated with sericitic alteration and a second generation of quartz (Fig. 9e). Telluride assemblages also occur as polyphase inclusions in pyrite (Fig. 9f), along grain boundaries between sulfide minerals, as elongated aggregates along healed microcracks or to a minor extent, disseminated within the late carbonate stage. Quartz is the most common gangue mineral and carbonate minerals (including calcite, rhodochrosite and kutnohorite ($CaMn[CO_3]_2$)) formed late in the paragenesis (Fig. 10). Hydrothermal apatite crystallized in clusters towards the end of the polymetallic stage and as disseminated crystals in the late carbonate stage. Hydrothermal fluorite occurs in places in Shahumyan. Distal propylitic alteration surrounds the deposit, where chlorite, epidote, carbonate and pyrite are typical alteration minerals. In proximity to the ore bodies, phyllic alteration with sericite, quartz and pyrite prevails. With decreasing depth, the phyllic alteration grades into an argillic alteration assemblage with dickite, quartz, pyrite and ± sericite.

Advanced argillic alteration and poorly developed residual quartz alteration within Middle Jurassic quartz-dacite can be found at surface in the northeastern part of the Shahumyan deposit (Fig. 3), where two different types of alunite can be distinguished. Nearly monomineralic east-west striking and steeply dipping alunite veins are composed of coarse-grained of up to 500 µm bladed pink alunite, associated with minor amounts of hematite, pyrite and quartz (sample 5-77; Fig. 11a). Up to 150 µm-sized, disseminated, transparent to pinkish bladed alunite crystals are associated with advanced argillic and residual quartz alteration. Alunite together with kaolinite and dickite replace plagioclase phenocrysts of the quartz-dacite host rock (sample 3-63-1; Fig. 11b). Achikgiozyan et al.

(1987) described with increasing distance from the most altered rocks, alunite, diaspore, dickite and sericite occurring with minor pyrite, hematite and supergene limonite. Advanced argillic altered quartz-dacite with disseminated alunite (sample 3-63-1; Fig. 11b) contains 0.24 ppm Au and 103 ppm As (Mederer, 2013), which is significantly enriched compared with an average of 3.6 ppm As in silicic volcanic rocks (Onishi and Sandell, 1955). By contrast, alunite from banded veins and its direct host rock (sample 5-77; Fig. 11a) contain only 0.02 ppm and 0.048 ppm Au, respectively, whereas the As content in vein alunite and host rock is 22 ppm and 12 ppm, respectively (Mederer, 2013).

Crosscutting relationships between dikes and mineralization in the Kapan deposits

Abundant dikes crosscut mineralized veins in the deposits of the Kapan district. The relative timing of dike emplacement with respect to mineralization in the Kapan deposits has been widely discussed and both pre- and post-mineralization scenarios have been proposed (see Achikgiozyan et al., 1987 and references therein). East-west-oriented and steeply dipping felsic dikes in the Centralni deposits are offset by sinistral strike-slip faults, whereas mineralized veins subparallel to the felsic dikes remain unaffected by the faults (Achikgiozyan et al., 1987). This relationship was used to attribute a pre-mineralization age to the felsic dikes (Achikgiozyan et al., 1987).

By contrast, diabase dikes postdate the mineralized veins of the Kapan district. The relative timing is clearly documented by dikes crosscutting banded polymetallic veins (Fig. 12a), ductile deformation affecting mineralized veins along the contact with crosscutting dike (Fig. 12b), and well-developed continuous chilled margins of the crosscutting dike along the contacts with adjacent Middle Jurassic host rock and a mineralized vein (Fig. 12c). In addition, diabase dikes crosscut the unconformity between the Middle Jurassic and Late Jurassic-Early Cretaceous magmatic complexes, whereas the mineralized veins are restricted to Middle Jurassic host rocks.

Analytical Techniques

Radiogenic and stable isotope analyses

The Pb isotopic composition of pyrite, galena, chalcopyrite and alunite was determined at the University of Geneva, Switzerland. A few milligrams of pyrite and chalcopyrite samples were digested in a mixture of 6*N* HCl and 14*N* HNO_3 (2:1), and alunite in a mixture of concentrated HF and 14*N* HNO_3 (3:1), whereas galena was digested in 14*N* HNO_3. The samples were converted to bromide form and Pb was separated by ion exchange chromatography. Lead was loaded on single Re filaments using the silica gel technique (Gerstenberger and Haase, 1997). The samples and SRM981 standards were analyzed at a pyrometer-controlled temperature of 1220°C on a Thermo TRITON mass spectrometer on Faraday cups in static mode. Lead isotope ratios were corrected for instrumental fractionation by a factor of 0.1% per amu based on more than 100 measurements of the SRM981 standard using the values of Todt et al. (1996). External reproducibilities (2σ) of the standard ratios are 0.05% for $^{206}Pb/^{204}Pb$, 0.08% for $^{207}Pb/^{204}Pb$ and 0.10% for $^{208}Pb/^{204}Pb$.

The strontium isotopic compositions of calcite samples were obtained at the University of Geneva, Switzerland. About 60 mg of calcite powder was dissolved in 2*N* HCl and Sr was separated by ion chromatography in hydrochloric medium. Strontium was loaded on single Re filaments with a

Ta-oxide solution and measured at a temperature of 1490°C on a Thermo TRITON mass spectrometer on Faraday cups in static mode. $^{87}Sr/^{86}Sr$ ratios were internally corrected for fractionation using a $^{88}Sr/^{86}Sr$ ratio of 8.375209. Raw values were further corrected for external fractionation by a value of +0.03‰, determined by repeated measurements of the SRM987 standard ($^{87}Sr/^{86}Sr$=0.710250). External reproducibility (1σ) of the SRM987 standard is 6 ppm.

For stable isotope analyses, monomineralic separates were obtained by careful handpicking under the binocular microscope. Isotopic compositions are expressed as δ values, in per mil (‰) deviations relative to the Vienna Standard Mean Ocean Water (VSMOW) for O and H, the Canyon Diablo Troilite (CDT) for S, and the Vienna Peedee Belemnite (VPDB) for C. The sulfur isotopic composition of sulfides and sulfates was measured using a Carlo Erba 1108 elemental analyzer connected to a Finnigan MAT Delta-S mass spectrometer at the University of Lausanne, Switzerland, following the analytical protocol described by Giesemann et al. (1994). 150-200 µg of powdered sulfide or 250 µg of sulfate sample were wrapped in tin capsules. Samples were combusted at 1020°C with Vanadium oxide serving as a catalyst/reactant and all gases produced during combustion were transported in a stream of helium to the reduction furnace (at 650°C). Water was subsequently removed in a water trap. Other gases like NO_2 and CO_2 were separated in a gas chromatography column (heated at 50°C) from SO_2, which was analyzed in the mass spectrometer. A reference gas SO_2 for isotopic calibration was introduced into the carrier gas stream via a CONFLO III. The standards during runs of sulfides included NBS 123 sphalerite ($\delta^{34}S$ = +17.4‰); Py-E pyrite ($\delta^{34}S$ = -7‰), and IAEA-S1 silver sulfide ($\delta^{34}S$ = -0.3‰), and barium sulfate ($\delta^{34}S$ = +20.3‰). External precision for the isotopic compositions was better than 0.2‰.

The dissolution-reprecipitation method (Wasserman et al., 1992) was applied to analyze the oxygen isotopic composition in the tetrahedral site of alunite. As not enough sample material was available from disseminated alunite, only vein alunite was treated by this method. About 120 mg of alunite were dissolved in a 0.5*N* NaOH solution and heated to 80°C (±10°C) for 3h. The solution was filtered and titrated by 10*N* HCl to a pH of 2.85 to avoid the precipitation of $Al(OH)_3$ at intermediate pH. By the addition of 5 ml of 0.5*N* $BaCl_2$ to the solution, the dissolved $(SO_4)^{2-}$ anions were precipitated as barite ($BaSO_4$). This barite precipitate was subsequently analyzed for its oxygen isotopic composition together with naturally occurring barite from the Centralni East deposit. 350 to 450 µg of sulfate sample were analyzed using a He carrier gas with a high-temperature conversion elemental analyzer (TC-EA) coupled to a DELTAplus XL Isotope-ratio mass spectrometer (IRMS) from ThermoFinnigan according to a method similar to that described in Vennemann and O'Neil (1993). The method is based on reduction by graphite and a buffer of glassy carbon at temperatures higher than 1450°C. The accuracy of analysis was periodically checked by analyses of the international reference barium sulfates NBS-127 (+9.3‰), IAEA SO-5 (+13.05‰) and SO-6 (-10.83‰). $\delta^{18}O$ values are precise within 0.3‰.

The hydrogen isotopic composition of alunite was measured using a high-temperature (1450°C) conversion elemental analyzer (TC-EA) with continuous flow reactor linked to a ThermoFinnigan DELTAplus XL Isotope-ratio mass spectrometer (IRMS), applying methods (Sharp et al., 2001). The in-house kaolinite (Kaol-17, δD = -125‰) and biotite standards (G1, δD = -66‰) were used to

assess measurement reproducibility. The accuracy of the TC/EA/IRMS analysis was checked periodically by analyses of the international reference standard biotite NBS-30 (δD = -65‰ VSMOW). δD values are precise to within 2‰.

The oxygen isotopic composition of quartz was obtained using a CO_2 laser fluorination system (Kasemann et al., 2001). Between 1 and 2 mg of sample were loaded on a Pt sample holder and evacuated to a vacuum of about 10^{-6} mbars. After prefluorination of the samples overnight, they were heated using a CO_2 laser in the presence of about 50 mbars of pure F_2 which was generated by a potassium nickel fluoride salt that was heated at >250°C. The hot mineral reacted quickly with F_2, releasing O_2 from silicate or oxide minerals. Excess F_2 was separated from O_2 by exchange with KCl at 150°C. The extracted O_2 was collected on a molecular sieve (13X) and subsequently expanded into the inlet of a Finnigan MAT 253 isotope mass ratio spectrometer. The in-house standard LS-1 ($\delta^{18}O$ = +18.1‰) was used for the normalization of the results. Replicate oxygen isotope analyses generally had an average precision of ±0.2‰.

The carbon and oxygen isotopic composition of calcite from the Shahumyan and Centralni West deposits was obtained according to Spötl and Vennemann (2003). CO_2 was released by the reaction of calcite with H_3PO_4, which was then transported by He after several cleaning steps into a continuous flow Gas Bench and analyzed by a ThermoFinnigan DELTAplus XL mass spectrometer. Samples were normalized to an in-house calcite standard (CM-STD; $\delta^{13}C_{VPDB}$ = +1.95±0.0.06‰; $\delta^{18}O_{VPDB}$ = -1.70±0.05‰) which has been calibrated relative to the international standard material NBS-19 ($\delta^{13}C_{VPDB}$ = +1.95‰; $\delta^{18}O_{VPDB}$= -2.20±0.05‰). Precision for the analyses is better than ±0.1 and ±0.15‰ for $\delta^{13}C$ and $\delta^{18}O$, respectively.

$^{40}Ar/^{39}Ar$ geochronology

$^{40}Ar/^{39}Ar$ incremental-heating analyses of one muscovite and two alunite samples (Fig. 11a-c), respectively, from the Centralni West and Shahumyan deposits were conducted. One plagioclase separate from the subvolcanic Barabatoom quartz-dacite was also analyzed (Fig. 11d). 6.3 mg of magmatic-hydrothermal alunite (100 µm in size) was extracted from cavities within sample 3-63-1, and handpicked under a binocular microscope. Magmatic-steam alunite from the massive vein sample 5-77 was crushed and 7 mg of alunite (2 mm in size) were separated. Sample JM016 was crushed by a hydraulic press and sieved before muscovite (9.2 mg, 10-100 µm) was handpicked using the binocular microscope. Sample 5-16 (Fig. 11d), which contains plagioclase phenocrysts of up to 1 cm in size was crushed and sieved, and 6.7 mg of plagioclase was gravitationally separated from quartz using sodium polytungstate and a centrifuge. The analyzed plagioclase had a grain size of ~2 mm and only the least altered fragments from the originally larger phenocrysts were selected. The four mineral separates were cleaned for 10 min in deionized water in an ultrasonic bath. Sample separates were packed in Cu foil, mounted in a glass silica tube and subsequently irradiated for 30 h in the CLICIT facility of the TRIGA reactor at Oregon State University, U.S.A. J-values were interpolated from samples of the 28.02±0.28 Ma old Fish Canyon Tuff sanidine (Renne et al., 1998), which was used as a flux monitor and were separated by distances of <1 cm in the columnar

irradiation package. Step-wise heating was performed using a 55 W IR-CO_2 laser, and a stainless-steel extraction line coupled with a multi-collector Argus mass spectrometer (GV Instruments) at the University of Geneva, Switzerland. The instrument was equipped with four high-gain (10^{12} Ω) Faraday cups for the measurement of ^{36}Ar, ^{37}Ar, ^{38}Ar, and ^{39}Ar, and a single 10^{11} Ω Faraday cup for ^{40}Ar measurements. One SAES AP10 getter and one water-cooled SAES GP50-ST101 getter are integrated in the automated UHV stainless steel gas extraction line. The isotopic composition of the gas was measured on the Faraday collectors and time-zero regressions were fitted to data collected from 12 cycles. Peak heights and backgrounds were corrected for baselines, mass discrimination, isotopic decay of ^{39}Ar and ^{37}Ar, and interfering nucleogenic Ca-, K-and Cl-derived isotopes. Error calculations include the errors on mass discrimination measurement and the J value. ^{40}Ar, ^{39}Ar, ^{38}Ar, ^{37}Ar, and ^{36}Ar blanks were calculated before every new sample and after every three heating steps. ^{40}Ar blanks were between 6.5E-16 and 1.0E-15 moles. Blank values for m/e 39 to 36 were all less than 6.5E-17 moles. Age plateaus were determined using the criteria of Dalrymple and Lanphere (1974) unless otherwise indicated, and data reduction utilized ArArCalc (Koppers, 2002).

Re-Os isochron dating of pyrite

Re-Os isotope analyses were obtained on pyrite samples from Centralni West and Centralni East. Pure pyrite separates of about 400 to 600 mg were separated at the University of Geneva by handpicking under the binocular microscope, cleaned ultrasonically in ethanol for 10 minutes and crushed to 5 mm. The Re and Os isotope analyses were carried out at Durham University, U.K., as described by Selby et al. (2009; and references therein). The accurately weighted samples were loaded into a Carius tube with a known amount of mixed Re-Os tracer solution containing ^{185}Re and ^{190}Os. The sample and tracer solution were digested and equilibrated using a mix of 11*N* HCl (3 ml) and 15.5*N* HNO_3 (8 ml) at 220°C during 48 h. Rhenium and Os were isolated by solvent extraction ($CHCl_3$), microdistillation, and anion column and single-bead chromatography methods. The purified Re and Os solutions were loaded onto Ni and Pt filaments, respectively, and analyzed by negative thermal ionization mass spectrometry on a Thermo Scientific TRITON mass spectrometer. The measured isotopic compositions were corrected for oxide and blank contribution, and fractionation. Total procedural blanks were 3.3±0.3 pg/g (Re) and 0.27±0.21 pg/g (Os), with an average ^{187}Os/^{188}Os ratio of 0.25 (n=3). All uncertainties are determined by propagation of uncertainties in the mass spectrometer measurements, blank abundances and isotopic compositions, spike calibrations, weighing of sample and spike, and the results from analyses of a Re-Os standard.

Results

Radiogenic isotopes

The Pb isotopic compositions of sulfides and alunite from the Kapan district range between 18.17-18.32 for ^{206}Pb/^{204}Pb, 15.57-15.61 for ^{207}Pb/^{204}Pb and 38.17-38.41 for ^{208}Pb/^{204}Pb (Table 2; Fig. 13). The ^{87}Sr/^{86}Sr ratios of hydrothermal calcite samples from the Centralni West and Shahumyan deposits fall in a narrow range between 0.70537 and 0.70586 (Table 3; Fig. 14).

Stable isotopes

The 32 analyzed sulfide samples from the Kapan district have sulfur isotopic compositions that fall in a narrow range between 2.0 and 6.5‰ (Table 4, Fig. 15). Pyrite has the highest $\delta^{34}S$ values at 4.5 to 6.4‰ except for one outlier at 2.5‰. Sphalerite, chalcopyrite and galena from the Shahumyan deposit have the lowest $\delta^{34}S$ values at 3.6 to 5.1‰. The pyrite $\delta^{34}S$ values from the Centralni East deposit range between 3.3 and 6.5‰, overlapping those of pyrite from the Shahumyan deposit (Fig. 15). The sulfide $\delta^{34}S$ values in the deposits cannot be ascribed to discrete mineralization stages. For example, in the Shahumyan deposit, pyrite from the main and late main stages can be characterized by either a high or low $\delta^{34}S$ value (Table 4). Gypsum from gypsum-pyrite veins and fault-related gypsum have $\delta^{34}S$ values of 19.5 and 18.0‰, respectively. One barite sample, which is in places associated with the main stage mineralization in the Centralni East deposit has a sulfur isotopic composition of 17.4‰ and a $\delta^{18}O$ value of 10.5‰ (Table 3). $\delta^{34}S$ values of chalcopyrite from the Centralni West deposit range between 2.0 and 4.4‰, whereas pyrite from this deposit is characterized by higher values between 4.9 and 6.1‰. Alunite from the massive alunite±hematite±quartz veins (Fig. 11a) from the northeastern limb of the Shahumyan deposit (Fig. 3) has a $\delta^{34}S$ value of 7.9‰ and a δD value of 34‰. $\delta^{18}O_{SO4}$ and $\delta^{18}O_{OH}$ of vein alunite are 14.4 and 10.9‰, respectively (Table 3). Disseminated alunite (Fig. 11b), which is associated with argillic alteration and minor pyrite along the northeastern limb of the Shahumyan deposit (Fig. 3) has a $\delta^{34}S$ value of 27.0‰, a δD value of -43‰ and a $\delta^{18}O_{tot}$ of 14.1‰.

Hydrothermal quartz samples from the Centralni West and Centralni East deposits yield, respectively, $\delta^{18}O$ values of 8.3 to 10.9‰ and 9.1 to 12.7‰ (Table 3, Fig. 16). The $\delta^{18}O$ values of hydrothermal quartz from the Shahumyan deposit range from 10.6 to 16.4‰. In all three deposits, the $\delta^{18}O$ values of hydrothermal quartz increase progressively with later mineralization stages. Pre-mineralization and main-stage quartz is generally more depleted in ^{18}O relative to late stage and post-mineralization quartz (Fig. 16). Igneous quartz from quartz-dacite of the Middle Jurassic Barabatoom Formation has a $\delta^{18}O$ value of 7.5‰ (Table 3, Fig. 16).

The isotopic composition of hydrothermal calcite from the Centralni West deposit ranges from 11.7 to 13.4‰ for $\delta^{18}O$ and from –3.4 to –2.1‰ for $\delta^{13}C$ (Table 3, Fig. 17a). The isotopic composition of calcite from the Shahumyan deposit is more variable and ranges from 7.7 to 15.4‰ for $\delta^{18}O$ and from –3.0 to 0.7‰ for $\delta^{13}C$. Positive correlation trends in $\delta^{13}C$ vs. $\delta^{18}O$ space can be observed in both deposits (Fig. 17a). The calcite data from the Shahumyan deposit also yield a positive correlation trend between $^{87}Sr/^{86}Sr$ and $\delta^{18}O$ values, whereas in the Centralni West deposit, higher $^{87}Sr/^{86}Sr$ ratios are uncorrelated with $\delta^{18}O$ values (Fig. 17b). The correlation arrays in hydrothermal calcite from the Kapan district are independent of depth or geographical distribution in the Centralni West and Shahumyan deposits.

$^{40}Ar/^{39}Ar$ geochronology

Hydrothermal muscovite from the Centralni West deposit (sample JM016; Fig. 11c) from the

western part of the Kapan district (Fig. 3) yields a $^{40}Ar/^{39}Ar$ plateau age of 161.78±0.79 Ma for 50% of the released gas, which overlaps with the inverse isochron age of 162.73±0.92 Ma with a MSWD of 0.99 (Fig. 18a, Tables 5 and 6). The age spectrum shows a typical argon loss profile, with successively older ages at higher temperature during successive step-heating.

The magmatic-hydrothermal alunite sample (sample 3-63-1; Fig. 11b) from the Shahumyan deposit (Fig. 3) yields a slightly disturbed age spectrum (Fig. 18b), which may be a consequence of ^{39}Ar recoil in the higher temperature steps (Onstott et al., 1995). A weighted mean age of 156.14±0.79 Ma has been calculated for a region of the age spectrum where the ages are indistinguishable, although they only span 40.4% of the ^{39}Ar released. The weighted mean age is indistinguishable from the inverse isochron age of 157.87±1.19 Ma (MSWD = 0.50). An argon loss profile can also be observed in the age spectrum, with a minimum step $^{40}Ar/^{39}Ar$ age of ~150 Ma.

The age spectra of plagioclase sample 5-16 (Fig. 11d) is highly disturbed, although it is characterized by ages that increase with increasing temperature of the heating steps (Fig. 18c). There are no plateau regions and the ages of single heating steps range between 132 and 170 Ma, with the highest temperature heating steps yielding ages of 164.89±2.80 and 165.17±5.27 Ma.

The magmatic-steam alunite sample (5-77; Fig. 11a) reveals a disturbed spectra and no plateau age can be defined (Fig. 18d). The initial two steps yielded elevated ages, perhaps due to the presence of excess ^{40}Ar, whereas the remaining steps yielded progressively increasing ages, which may be indicative of Ar loss.

Re-Os geochronology of pyrite

Total Re and Os contents in pyrite from the deposits in the Kapan district are low and range from 1.3 to 3.6 ppb and 2.2 to 11.9 ppt, respectively (Table 7). The $^{187}Re/^{188}Os$ ratios are very high (4620 to 74850), and the $^{187}Os/^{188}Os$ compositions are highly radiogenic (13 to 243; Table 7). The elevated $^{187}Re/^{188}Os$ ratio indicates the near absence of common Os, and therefore allows us to classify the sulfides as Low Level Highly Radiogenic (LLHR; Stein et al., 2000). Traditional $^{187}Re/^{188}Os$ (x-axis) vs. $^{187}Os/^{188}Os$ (y-axis) plots show highly correlated uncertainties as a consequence of the poorly determined, but extremely low concentration of ^{188}Os. For that reason, the data are plotted with the associated uncertainty correlation value, named rho (Ludwig, 1980), which allows a conventional best fit of the data (e.g., Stein et al., 2000; Selby et al., 2009). However, due to the virtual absence of common ^{188}Os and the highly radiogenic character of pyrite samples from the Kapan district, a direct regression of parent isotope ^{187}Re vs. the daughter isotope ^{187}Os can give meaningful and precise age information (e.g., Stein et al., 2000; Selby et al., 2009; Kerr and Selby, 2012). As in the case of molybdenite, single mineral ^{187}Re-^{187}Os model ages can be calculated for each individual LLHR sulfide sample (Stein et al., 2000; Selby et al., 2009).

Regression of the $^{187}Re/^{188}Os$ vs. $^{187}Os/^{188}Os$ data of four pyrite separates from the Centralni West deposit yield a model 3 Re-Os age of 215.7±9.2 Ma (MSWD = 6.9; Fig. 19a), with an initial $^{187}Os/^{188}Os$ ratio of 1.3±3.6. Using the initial $^{187}Os/^{188}Os$ composition of 1.3±3.6, ~92.5 to 99.4 % of the ^{187}Os in the pyrite samples is radiogenic. A model 1 age of 207±24 Ma is determined from the

^{187}Re vs. ^{187}Os^{r} data (initial ^{187}Os^{r} = 0.31±0.83; MSWD = 0.21; Fig. 19b). Four calculated single mineral Re-Os model ages range from ~202 to 221 Ma, with a weighted average of 215.7±4.2 Ma (MSWD = 0.32; Fig. 19c). All three ages are the same within uncertainty, but the more precise weighted average model age is our preferred solution.

The traditional ^{187}Re/^{188}Os vs. ^{187}Os/^{188}Os isochron regression of five pyrite separates from the Centralni East deposit yield a model 1 Re-Os age of 144.7±4.2 Ma with a MSWD of 0.099 (Fig. 19d). An initial ^{187}Os/^{188}Os value of 1.41±0.57 was obtained from the isochron. Using this initial ^{187}Os/^{188}Os composition, ~88.4 to 98.0% of the ^{187}Os in the pyrite samples is radiogenic. The best fit of ^{187}Re vs. ^{187}Os^{r} yields a less precise model 1 age of 148±11 Ma (initial ^{187}Os^{r} = -0.03±0.22; MSWD = 0.31; Fig. 19e). Calculated single mineral model ages from the five pyrite analyses range from 144.5 to 148.4 Ma, with a weighted average of 146.2±3.4 Ma (MSWD = 0.25; Fig. 19f). The three ages are the same within uncertainty, the more precise weighted average model age is our preferred solution.

Discussion

Source of metals

The Pb isotopic composition of hydrothermal minerals from the Centralni West, Centralni East and Shahumyan deposits overlap (Fig. 13), which indicates a common metal source broadly tapped at the same time. The overlap of the Pb isotopic compositions of sulfide minerals and alunite from the ore deposits with age-corrected (161-145 Ma) Middle Jurassic igneous rocks (Fig. 13) suggests that Pb was leached by hydrothermal fluids from the host Middle Jurassic magmatic rocks, or was derived by direct exsolution of a magmatic-hydrothermal fluid from Middle Jurassic intrusions at depth. By extension, this interpretation also applies to the other base and precious metals of the Kapan deposits.

Nature of hydrothermal fluids involved in ore formation: evidence from Sr, O and C isotopes

As calcite generally does not incorporate Rb in its crystal lattice, its ^{87}Sr/^{86}Sr ratio reflects the Sr isotopic composition of the precipitating fluid (Ruiz et al., 1984). The Sr isotopic composition of hydrothermal calcite from the Shahumyan and Centralni West deposits is slightly more radiogenic in comparison with age-corrected (161-145 Ma) ^{87}Sr/^{86}Sr ratios of Middle Jurassic magmatic rocks (Fig. 14). In the Kapan district, no lithological units with ^{87}Sr/^{86}Sr ratios higher than the ones of the Middle Jurassic magmatic complex have been observed (Mederer et al., 2013). The only local reservoir with an elevated radiogenic Sr isotopic composition was Middle Jurassic seawater with ^{87}Sr/^{86}Sr ratios between 0.7067 and 0.7073 at 170-140 Ma (Jones et al., 1994). Such a seawater environment is supported by the presence of subaqueous volcaniclastic and volcanic rocks within the Middle Jurassic magmatic complex (Achikgiozyan et al., 1987; Mederer et al., 2013). Therefore, we conclude that seawater was involved during the late carbonate stage, and we interpret their Sr isotopic composition to reflect mixing of seawater-derived Sr and Sr leached or exsolved from

Middle Jurassic igneous rocks.

Temperatures between 140 and 433°C were calculated using oxygen isotope data of four quartz-calcite pairs from the late carbonate stage in the Shahumyan deposit (Table 3) according to the equation of Zheng (1993). The large temperature spread indicates that equilibrium conditions were not attained between the two minerals. No more precise temperature estimates are available for the precipitation of gangue and ore minerals in the Kapan district deposits. Therefore, the oxygen isotopic composition of fluids in equilibrium with early-stage hydrothermal quartz and late-stage calcite was calculated using the equations of Zheng (1993; 1999) for temperatures between 400 and 200°C, and 300 and 150°C, respectively (Table 3). Such temperature ranges are typical for polymetallic veins (e.g., Rusk et al., 2008; Catchpole et al., 2011). The calculated oxygen isotopic compositions range between –5.4 and 11.9‰ (Fig. 20a). Depending on the precipitation temperature of quartz and calcite, the $\delta^{18}O_{H2O}$ values overlap with the field for primary magmatic fluids (Taylor, 1988; PMW range in Fig. 20a) or are shifted towards the seawater $\delta^{18}O$ value ($\delta^{18}O$ = 0‰; SMOW in Fig. 20a) or negative $\delta^{18}O$ values characteristic of meteoric fluids (Hoefs, 2009). Assuming cooling during successive mineralization stages (gray arrows in Fig. 20a), early hot fluids are characterized by higher $\delta^{18}O_{H2O}$ values, whereas late and cooler fluids are more depleted in ^{18}O. In the case of the polymetallic Shahumyan deposit, an early pre-mineralization fluid of 300-400°C would be characterized by $\delta^{18}O_{H2O}$ values between 3.6 and 7.2‰, whereas late carbonate stage fluids would range between –5.4 and 5.6‰ (Table 3; Fig. 20a). Such a difference between the isotopic composition of pre- and post-mineralization fluids can be explained by both cooling of a magmatic-derived fluid and progressive mixing with seawater or meteoric water.

The positive correlation of $\delta^{18}O$ and $\delta^{13}C$ values of calcite from the Centralni West and Shahumyan deposits (Fig. 17a) could be consistent with: (1) precipitation during fluid cooling, as the fractionation factors for oxygen between calcite and H_2O and carbon between CO_2 and calcite are linearly correlated with temperature (Ohmoto and Rye, 1979), (2) CO_2 degassing or boiling (Zheng, 1990), and (3) fluid/rock interaction or fluid mixing (Zheng and Hoefs, 1993). Calcite solubility in hydrothermal fluids increases with decreasing temperature (Holland and Malinin, 1979), therefore precipitation of calcite cannot be explained by simple cooling alone. Solely boiling also cannot explain increasing $^{87}Sr/^{86}Sr$ ratios at higher or constant $\delta^{18}O$ values in hydrothermal calcite (Fig. 17b), because boiling would have no effect on the $^{87}Sr/^{86}Sr$ ratio of a hydrothermal fluid. Finally, the $^{87}Sr/^{86}Sr$ ratios of hydrothermal calcite, which are more radiogenic than those of the immediate Middle Jurassic magmatic rocks (Fig. 14), are inconsistent with fluid-rock interaction as the sole mechanism to explain the positive correlation of $\delta^{18}O$ and $\delta^{13}C$ values of calcite. Therefore, mixing of a magmatic-derived fluid and seawater can explain both, the variability in the Sr isotopic composition and the correlation in $\delta^{18}O$ and $\delta^{13}C$ space, with the stable isotopes being additionally controlled by temperature-dependent fractionation (Zheng and Hoefs, 1993; Zheng, 1999).

Source of sulfur and implications from sulfur isotopes

The sulfur isotopic composition of sulfides from the Kapan deposits ranges from 2.0 to 6.5‰ (Fig. 15), which is compatible with a magmatic source for sulfur, either directly derived from an igneous

source or by leaching of sulfur-bearing minerals in igneous rocks (Ohmoto, 1986). Using the sulfur isotope geothermometry equations of Kajiwara and Krouse (1971), a temperature range of 96 to 381°C was calculated for pyrite-sphalerite, sphalerite-chalcopyrite and pyrite-chalcopyrite pairs from the main stage mineralization at Shahumyan (Table 4). Temperatures calculated from the isotopic composition of pyrite-chalcopyrite pairs from the Centralni West deposit range between 93 and 592°C (Table 4). Pyrite-barite and pyrite-gypsum pairs from the Centralni East deposit indicate precipitation temperatures of 395 and 357°C (Table 4), respectively, using the fractionation equations of Ohmoto and Lasaga (1982).

The wide range of temperatures questions the reliability of calculated results, and suggests disequilibrium between the minerals. Such disequilibrium conditions can be attributed to fluid mixing (Zheng, 1991), which is consistent with the conclusions based on the Sr, O and C isotopes. The $\delta^{34}S$ values of 17.4‰ of barite and the ones of 18.0 to 19.5‰ of gypsum from the Centralni East deposit overlap with or are slightly more enriched relative to the $\delta^{34}S$ value of 14.5 to 17.5‰ of Jurassic seawater sulfate (Fig. 15; Claypool et al., 1980). Therefore, the sulfur isotope data of minerals from the Kapan deposits are also consistent with mixing of a hydrothermal fluid dominated by sulfur of magmatic origin and seawater. In such a fluid-mixing scenario, the isotopic composition of sulfide minerals is inherited from the isotopic composition of sulfur in the hydrothermal fluid of magmatic origin prior to mixing (Zheng, 1991), whereas the $\delta^{34}S$ values of sulfate minerals are similar to or slightly higher than contemporaneous seawater (Çagatay and Eastoe, 1995; Ohmoto and Goldhaber, 1997).

Hypogene alunite at the Shahumyan deposit

Oxygen and hydrogen isotopic compositions for the two alunite samples hosted in Middle Jurassic quartz-dacite from the northeastern limb of the Shahumyan deposit (Figs. 3 and 11a, b) are given in Figure 20b. Fluid compositions in equilibrium with alunite were calculated from equations of Stoffregen et al. (1994) over a temperature range of 400 to 150°C (Table 3, Fig. 20b), which are typical for temperatures related to magmatic vapor condensation and magmatic steam processes (Rye et al., 1992; Rye, 1993, 2005). The calculated fluid compositions (Fig. 20b) overlap with those of typical felsic magmatic fluids (Taylor, 1988) and the range of water compositions discharged from high-temperature fumaroles, i.e. volcanic vapor (Giggenbach, 1992). This indicates a predominant magmatic component in the source fluids for both alunite samples. However, the rather wide field of alunite fluid compositions in Figure 20b (caused in part due to the poorly defined precipitation temperatures as limited by the paragenesis) suggests mixing of a magmatic fluid with meteoric water or seawater. Finally, an equilibrium temperature of 59°C has been calculated from $\Delta^{34}S_{SO4\text{-}OH}$ from the equation of Stoffregen et al. (1994). This is an unreasonably low depositional temperature for alunite in a magmatic environment, and is best explained by retrograde isotopic exchange of hydrogen and oxygen from the OH site in alunite with later meteoric water (Rye, 2005).

Based on its sulfur isotopic composition of 27‰ (Table 4), its advanced argillic alteration assemblage (quartz-alunite±kaolinite and dickite) and its metal-enriched character (with 0.24 ppm Au and 103 ppm As; Mederer, 2013), we interpret the disseminated alunite of sample 3-63-1 (Fig.

11b) as belonging to the magmatic-hydrothermal type with sulfate derived from disproportionation of magmatic SO_2 to H_2S and H_2SO_4 (Rye et al., 1992; Rye, 1993). The presence of dickite indicates formation temperatures of less than 250-200°C (Hemley et al., 1980).

Vein alunite of sample 5-77 (Fig. 11a) is interpreted as magmatic-steam alunite (Rye et al., 1992) based on its coarse-grained nature, its occurrence in an extensional vein, its association with hematite and minor pyrite, and its $\delta^{34}S$ value of 7.9‰. Hypogene magmatic-steam alunite typically precipitates during expansion of ascending SO_2-rich vapor under disequilibrium conditions without significant disproportionation of SO_2 and reequilibration with the host rock (Rye et al., 1992). Coarsely banded alunite veins are almost monomineralic with only minor associated hematite and pyrite (e.g., Alunite Ridge, Utah; Cunningham et al., 1984; Rye, 1993), and are interpreted to form during rapid episodic degassing of an underlying magma in an extensional setting.

Timing and cooling ages of hydrothermal events

Figure 21 summarizes the Re-Os and $^{40}Ar/^{39}Ar$ ages obtained in this study together with dated magmatic events in the Kapan district (Mederer et al., 2013), and the sequence of significant geological events of the Kapan district. Previously, Bagdasaryan et al. (1969) obtained whole-rock K-Ar ages ranging from 137 to 152 Ma for altered host rocks in contact with mineralization. However they will not be considered any further, because the accuracy of such whole-rock K-Ar ages, especially in the case of altered samples, is questionable (Kelley, 2002). Below, we discuss the meaning and the reliability of the Re-Os pyrite and the $^{40}Ar/^{39}Ar$ muscovite ages obtained in the course of this study.

The subvolcanic Barabatoom quartz-dacite, which hosts the Shahumyan deposit, cuts early Bathonian strata (~168-166 Ma) and is unconformably overlain by Callovian (~166-163.5 Ma) fossil-bearing limestone (Achikgiozyan et al., 1987; Zohrabyan, 2005). A plagioclase separate from the Barabatoom quartz-dacite yielded a disturbed $^{40}Ar/^{39}Ar$ spectra (sample 5-16; Fig. 18c). Nevertheless, the two oldest heating steps yield ages between 160-170 Ma, which support a Middle Jurassic age for the Barabatoom quartz-dacite based on cross-cutting relationships. The Ar-loss profile in the plagioclase is attributed to thermal disturbance after the rock had crystallized, but at a temperature not surpassing the plagioclase argon partial retention zone (160-375°C; Chew and Spikings, 2015), as the sample still records a Middle Jurassic age in the most retentive parts of the grains.

The $^{40}Ar/^{39}Ar$ muscovite plateau age of 161.78±0.79 Ma obtained from the Centralni West deposit (sample JM016; Fig. 18a) records cooling after hydrothermal alteration and documents the earliest ore-forming event in the Kapan district. This is the most robust and reliable age of hydrothermal ore formation in the Kapan district obtained in the course of our study, and is consistent with our geological observations. The Ar-loss profile during the lower temperature steps of the age spectra may be due to secondary alteration, or younger heating events to temperatures within the muscovite partial retention zone (310-435°C; Chew and Spikings, 2015).

The partially disturbed $^{40}Ar/^{39}Ar$ age spectra of the magmatic hydrothermal alunite from the

Shahumyan deposit (sample 3-63-1) must be interpreted with caution, since the longest plateau only consists of 40.4% of the total released gas (Fig. 18b). The partially disturbed age spectra maybe a consequence of secondary fluid circulation or thermal events that post-date alunite precipitation. Its weighted mean $^{40}Ar/^{39}Ar$ age of 156.14±0.79 Ma is inconsistent with our geological field observations, indicating that the mineralized veins at Shahumyan are restricted to the Middle Jurassic magmatic complex and do not extend across the late Oxfordian unconformity (Fig. 4).

The same applies to the Re-Os isochron age of 144.7±4.2 Ma (MSWD = 0.099), and the weighted average age of 146.2±3.4 Ma yielded by pyrite samples from the Centralni East deposit (Fig.19d-f). Indeed, the Centralni East ore bodies are also confined to Middle Jurassic magmatic rocks below the late Oxfordian unconformity (Fig. 4). Furthermore, the initial $^{187}Os/^{188}Os$ ratio of 1.41±0.57 obtained for the sulfide mineralization in the Centralni East deposit is similar to the composition of average continental crust at 145 Ma ($^{187}Os/^{188}Os$ = 1.4±0.3; Peucker-Ehrenbrink and Jahn, 2001), and is significantly more radiogenic than a primitive mantle source ($^{187}Os/^{188}Os$ of CHUR at 145 Ma = 0.12761±0.00046; Chen et al., 1998). The initial $^{187}Os/^{188}Os$ composition is inconsistent with the primitive, mantle-dominated Pb, Sr and Nd isotopic composition reported for Late Jurassic-Early Cretaceous magmatic rocks in the Kapan district (Mederer et al., 2013). The only possible explanation for such a discrepancy could be related to the elevated sensitivity to crustal contamination of the Re/Os system (Shirey and Walker, 1998; Ruiz and Mathur, 1999), whereby the high initial $^{187}Os/^{188}Os$ ratio of 1.41±0.57 might indicate interaction of mineralizing hydrothermal fluids with hidden basement units at depth, that remain unrecognized so far. The more likely interpretation is that the Re-Os isotopic system in pyrite was disturbed by younger thermal events (e.g., Stein et al., 1998; Mathur et al., 1999). Therefore, the Re-Os pyrite isochron age from the Centralni East deposit must be treated with great caution.

The Re-Os isochron age of 215.7±9.2 Ma and the weighted average model age of 215.7±4.2 Ma yielded by pyrite sampled at the the Centralni West deposit (Fig. 19a-c) are at least 45 m.y. older than the Middle Jurassic host rocks of the deposit (Fig. 4). Based on this contradiction, the high uncertainty associated with the initial $^{187}Os/^{188}Os$ ratio of the sulfide ore (1.3±3.6) and the high MSWD of 6.9 for the best fit of the Re-Os data, we conclude that the Re-Os isotopic system in pyrite of the Centralni West deposit must have been disturbed after it was precipitated. Considering the independently obtained $^{40}Ar/^{39}Ar$ muscovite age of 161.78±0.79 Ma for the Centralni West deposit (sample JM016; Fig. 18a), we interpret the Late Triassic Re-Os age to be geologically meaningless.

Further radiometric dating to determine the timing of ore-forming hydrothermal pulses and related igneous events has not been possible in the Kapan district, because suitable minerals were not available. Volcanic, subvolcanic and volcanosedimentary host rocks and the diabase dikes that cross-cut mineralization did not yield any zircons during mineral separation, and igneous minerals that contain potassium are generally altered, even in the peripheries of the deposits, where propylitic alteration prevails.

In the Kapan district, overprinting events, which could explain the disturbed $^{40}Ar/^{39}Ar$ age spectra (Fig. 18b-d) and the disturbed Re-Os ages (Fig. 19), include Early Cretaceous intrusive activity

within the Kapan block at Shikahogh (Figs. 2, 4 and 21; Mederer et al., 2013, Melkonyan et al., 2016), Cretaceous collision of the South Armenian and the Kapan blocks (e.g. Rolland et al., 2009a), final Cenozoic Arabia-Eurasia collision, and/or Cenozoic magmatic activity in the western Kapan district (Fig. 2), which was related to emplacement of the composite Meghri-Ordubad and Bargushat plutons (Moritz et al., 2016b; Rezeau et al., 2016, 2017).

Middle Jurassic to Early Cretaceous metallogenic evolution of the Kapan district

The main Mesozoic geologic and metallogenic events of the Kapan district are summarized in Figure 21 and depicted in Figure 22, including remaining ambiguities. Lithogeochemistry (Fig. 5) and radiogenic isotope data of the igneous rocks (Mederer et al., 2013) indicate that the Kapan block is the result of progressive magmatic arc construction along a convergent margin (Fig. 22), starting with tholeiitic to transitional magmatism during the Middle Jurassic, which then evolved to a Late Jurassic-Early Cretaceous mature magmatic arc stage, characterized by transitional to calc-alkaline compositions, coeval with slab roll-back and asthenospheric upwelling (Mederer et al., 2013; Fig. 22). Hyaloclastite and subsidiary pillow lava in the volcanic and volcanoclastic rocks interlayered with reef limestone and carbonaceous sandstone are evidence for predominantly shallow water depths during the Middle Jurassic in the Kapan zone (Cholahyan and Sarkisyan, 1972; Achikgiozyan et al., 1987; Mederer et al., 2013). The Middle Jurassic rocks were partly eroded during or before the late Oxfordian (Fig. 22; Akopyan, 1962; Achikgiozyan et al., 1987; Mederer et al., 2013), and Late Jurassic-Early Cretaceous volcanic rocks were deposited on top of the unconformity in both subaqueous and subaerial environments (Cholahyan and Sarkisyan, 1972; Achikgiozyan et al., 1987).

The 161.78±0.79 Ma $^{40}Ar/^{39}Ar$ plateau age of muscovite from the Centralni West deposit (sample JM016; Fig. 18a) provides the most robust and reliable age of hydrothermal ore formation in the Kapan district. It documents the earliest ore formation event in this district and overlaps with the Middle Jurassic age of the immediate host rocks (Fig. 21). The hydrothermal alteration including chlorite, carbonate, quartz, epidote, pyrite and sericite, the submarine host rock setting, and the Cu-dominant metal association, are consistent with an ore-forming system within a submarine environment during the Middle Jurassic, comparable to VMS type deposits (e.g. Galley et al., 2007). Tonalite clasts sampled from subvertical polymict pebble dikes yielding a U-Pb zircon age of 165.6±1.4 Ma (Mederer et al., 2013), together with gabbro-diorite intersected by drill-holes below Kapan (Tumanyan, 1992), provide evidence of intrusive activity at depth during Middle Jurassic arc construction, predating mineralization at the Centralni West deposit by at least 1.6 m.y. The later intrusive association together with the tholeiitic to transitional composition of the Middle Jurassic volcanic complex (Fig. 5) is comparable to composite, synvolcanic gabbro-diorite-tonalite clusters underlying eruptive centers, interpreted as the heat engines sustaining hydrothermal systems in typical VMS districts (e.g. Galley, 2003; Galley et al., 2007). Moreover, the district-wide epidote alteration at the base of the Middle Jurassic complex in the Kapan area, reported by Cholahyan and Sarkisyan (1972) and Achikgiozyan et al. (1987), is reminiscent of semi-conformable epidote-dominated hydrothermal alteration zones typically described at depth in many VMS districts,

immediately at the top of synvolcanic gabbro-diorite-tonalite intrusions (e.g. Galley, 1993; Fig. 14 in Galley et al., 2007). The submarine setting is supported by the Sr and stable isotope systematics of different hydrothermal minerals sampled at Centralni West (Figs. 14 and 15). We conclude that during the Middle Jurassic to Late Jurassic transition (Fig. 22), the Kapan zone corresponded to a nascent volcanic arc with submarine magmatic-hydrothermal ore formation at Centralni West, and is comparable to other magmatic-hydrothermal and VMS systems associated with submarine volcanic arcs along subduction settings (de Ronde et al., 2005, 2011; Hannington et al., 2005). Because Centralni West is the westernmost deposit of the Kapan district, closest to the subduction trench (Fig. 3), it can be speculated whether this ore deposit might have formed in a fore-arc environment (Fig. 22), as documented for instance in the Uralides (Herrington et al., 2005a, b) and the Caribbean (Torró et al., 2016). However, further studies are required to ascertain such an interpretation.

The polymetallic veins at Shahumyan and the stockwork-type mineralization at Centralni East have distinct characteristics with respect to the Centralni West deposit. Centralni East and Shahumyan are comparable to sulfide-rich base-and precious-metal veins associated with epithermal-porphyry systems (e.g. Simmons et al., 2005; Sillitoe, 2010), such as the Main Stage veins in Butte, U.S.A. (Rusk et al., 2008) or the polymetallic veins in Morococha, Peru (Catchpole et al., 2011). The Centralni East and Shahumyan deposits contain high-sulfidation state mineral assemblages (Figs. 8d and 10d) and advanced argillic alteration including hypogene alunite (Fig. 11a, b), which are typically attributed to disproportionation of magmatic SO_2 during mixing with surface waters in subaerial settings (Giggenbach, 1992, 1997; Einaudi et al., 2003), but which are also recognized in submarine hydrothermal systems (e.g. de Ronde et al., 2005; 2011; Huston et al., 2011). Based on Sr and stable isotope systematics a submarine or a transitional subaerial-submarine environment can be envisaged in the Kapan district (Figs. 14 and 15).

The ore bodies at Shahumyan and Centralni East are confined to Middle Jurassic magmatic rocks and do not extend across the late Oxfordian unconformity (Fig 22a). Based on this geological evidence, we conclude that both deposits were formed early during the magmatic arc evolution and before the late Oxfordian (Fig. 22a). In the absence of relative crosscutting relationships, we interpret them as being broadly coeval or having been formed within a short time frame with respect to the Middle Jurassic Centralni West submarine hydrothermal deposit. Such a metallogenic setting would be comparable to similar hybrid or juxtaposed VMS-epithermal-porphyry systems described in island-arc settings in the Pacific and in Australia (e.g. Hannington, 1997, 2011; Large et al., 2001).

This interpretation is contradicted by the Re-Os pyrite weighted average date of 146.2±3.4 Ma (Fig. 19d-f) and the weighted mean $^{40}Ar/^{39}Ar$ age of 156.14±0.79 Ma (Fig. 18b) obtained for pyrite samples from Centralni East and for alunite from Shahumyan, respectively. These ages tell us that both deposits were formed during the Late Jurassic, significantly later than Centralni West and after the late Oxfordian erosion event (Figs. 21 and 22b). Several pieces of evidence speak against such a scenario. As discussed above, both radiometric ages are highly questionable, and the Re-Os and Ar systems were likely disturbed during overprinting thermal events. Furthermore, it would be remarkable that a Late Jurassic magmatic-related and epigenetic ore system forming stockwork and steep veins would remain confined to the Middle Jurassic rock complex below the late Oxfordian

unconformity (Fig. 22b). Finally, the homogeneous Pb isotopic composition of hydrothermal minerals supports a coeval and common metal source for the Centralni West, Centralni East and Shahumyan deposits (Fig. 13), and indicates that Pb and the other metals were solely derived from Middle Jurassic magmatic rocks or magmas. There is no supporting evidence for any metal input from Late Jurassic magmatic rocks or magmas. Therefore, we conclude that the combined field and geochemical dataset supports ore formation within a short time frame at Centralni West, Centralni East and Shahumyan before the late Oxfordian (Fig. 22a), rather than distinct Middle and Late Jurassic ore-forming pulses separated by 5 to 15 m.y. (Fig. 22b).

The Shikahogh Cu-Au-Mo prospect associated with the Tsav intrusion (Fig. 2) shows that after the Jurassic, renewed magmatic activity and ore formation affected the Kapan block during the Early Cretaceous (Figs. 21 and 22). The 139 to 128 Ma U-Pb ages of the Tsav intrusion and the spatially associated Shikahogh prospect coincide with porphyry and epithermal ore formation in the Gedabek district within the Somkheto-Karabagh arc (Fig. 1) at about 133 Ma (Moritz et al., 2016a).

Conclusions

The Kapan district consists of three major ore deposits, including Centralni West, Centralni East and Shahumyan. The three deposits have different metal endowments, ore body geometries, hydrothermal alteration features and opaque mineral assemblages. However, they are all hosted by Middle Jurassic magmatic rocks cut by a late Oxfordian unconformity, and they have lead isotopic compositions indicating derivation of metals from a common Middle Jurassic magma or from the same Middle Jurassic magmatic host rocks. We conclude that the Cu-dominated Centralni West ore deposit was formed along a submarine volcanic arc in a subduction environment, as evidenced by its volcanic host rocks deposited in a subaqueous setting, and its hydrothermal alteration dominated by chlorite, carbonate, quartz, epidote, pyrite and sericite. The submarine setting is also supported by the Sr and stable isotope compositions of hydrothermal minerals. A well-defined $^{40}Ar/^{39}Ar$ plateau age of 161.78±0.79 Ma of hydrothermal muscovite indicates that the Centralni West deposit formed early during Middle Jurassic arc construction dominated by tholeiitic to transitional magmatism.

The Shahumyan polymetallic vein-type and the Centralni East Cu-Au stockwork-type deposits contain intermediate- to high-sulfidation state opaque mineral assemblages and are hosted by magmatic rocks affected by advanced argillic alteration. They are comparable to sulfide-rich base- and precious-metal veins associated with epithermal-porphyry systems. Strontium and stable isotope systematics support a submarine or a transitional subaerial-submarine setting. Since ore bodies at Shahumyan and Centralni East are confined to Middle Jurassic magmatic rocks, do not extend across the late Oxfordian unconformity and are cut by Late Jurassic-Early Cretaceous magmatic rocks, we conclude that both deposits were formed broadly in the same time interval as the Centralni West Cu deposit in a nascent tholeiitic to transitional magmatic arc.

Our metallogenic interpretation for the Kapan district could be questioned by a disturbed $^{40}Ar/^{39}Ar$ plateau age of 156.14±0.79 Ma (only 40% of total released gas) of magmatic-hydrothermal alunite from Shahumyan, and a 146.2±3.4 Ma Re-Os weighted average model age of pyrite samples from the Centralni East deposit. However, both ages are rejected because they contradict geological field

relationships and lead isotope systematics. We conclude that both isotope ages were affected by overprinting events, including Early Cretaceous magmatism within the Kapan block, Cretaceous collision of the South Armenian and the Kapan blocks, final Cenozoic Arabia-Eurasia collision, and Cenozoic magmatic activity in the western Kapan district and the South Armenian block.

Acknowledgements

This study was supported by the Swiss National Science Foundation (grants 200020-121519, 200020-138130 and 200020-168996), the SCOPES project (IZ73ZO-128324) and Dundee Precious Metals, which provided field and logistical support and access to the mine area. J.M. benefited from travel grants by the Augustin Lombard Foundation of the Geneva SPHN Society and a SEG student research grant from the Hugh E. McKinstry Fund. Tamara Beridze is acknowledged for the translation of selected articles from Russian into English and Arman Vardanyan for his support in the field. Michèle Senn-Gerber and Fabio Capponi are thanked for analytical support and technical assistance at the University of Geneva, Benita Putlitz and Kerstin Bauer for their assistance in the stable isotope laboratory at the University of Lausanne. DS acknowledges the TOTAL endowment fund and a Dida Scholarship from CUG, Wuhan. Thanks to Sergej Zohrabyan and Rafael Melkonyan for fruitful discussions about the geology of the Kapan district. Alan Wainwright and Timothy Baker are thanked for their constructive and very helpful reviews, which allowed us to considerably improve this manuscript.

References

Achikgiozyan, S.O., Zohrabyan, S.A., Karapetyan, A.I., Mirzoyan, H.G., Sargisyan, R.A., and Zaryan, R.N., 1987, The Kapan Mining district: Yerevan, Publishing House of the Academy of Sciences of the Armenian SSR, 198 p. (in Russian).

Adamia, Sh.A., Lordkipanidze, M.B., and Zakariadze, G.S., 1977, Evolution of an active continental margin as exemplified by the Alpine history of the Caucasus: Tectonophysics, v. 40, p. 183–199.

Adamia, Sh.A., Zakariadze G., Chkhotua T., Sadradze N., Tsereteli N., Chabukiani A., and Gventsdze A., 2011, Geology of the Caucasus: A Review: Turkish Journal of Earth Sciences, v. 20, p. 489-544.

Aghazadeh, M., Hou, Z., Badrzadeh, Z., and Zhou, L., 2015, Temporal–spatial distribution and tectonic setting of porphyry copper deposits in Iran: Constraints from zircon U–Pb and molybdenite Re–Os geochronology: Ore Geology Reviews, v. 70, p. 385-406.

Akopyan, V.T., 1962, Stratigraphy of Jurassic and Cretaceous suites of South-Eastern Zangezur: Yerevan, Armenian Academy of Sciences SSR, 265 p. (in Russian).

Amiryan, Sh.H., 1984, Gold ore formation of Armenian SSR: Yerevan, Publishing House of the Academy of Sciences of the Armenian SSR, 304 p. (in Russian).

Amiryan, Sh.H., and Karapetyan, A.I., 1964, Mineralogical-geochemical characteristics of the ores of the Meghradzor gold deposit: Proceedings of the National Academy of Sciences of the Republic of Armenia, Earth Sciences, v. 17, p. 37-48 (in Russian).

Amiryan, Sh.H., Pidjyan G.H., and Faramazyan A.S., 1987, Mineralization stages and ore minerals of the Teghout ore deposit: Proceedings of the National Academy of Sciences of the Republic of Armenia, Earth Sciences, v. 40, p. 31-44 (in Russian with English abstract).

Aslanyan, A.T., 1958, Regional geology of Armenia: Yerevan, Haypetrat Edition, 430 p. (in Russian).

Azizi, H., and Moinevaziri, H., 2009, Review of the tectonic setting of Cretaceous to Quaternary volcanism in northwestern Iran: Journal of Geodynamics, v. 47, p. 167–179.

Babazadeh, V.M., Makhmudov, A.I., and Ramazanov, V.G., 1990, Porphyry-copper and molybdenum deposits: Baku, Azerbaijan Publication, 377 p. (In Russian with German and English abstracts).

Bagdasaryan, G.P., Ghoukassyan, R.K., and Karamyan, K.A., 1969, Absolute dating of Armenian ore formations: International Geology Review, v. 11, p. 1166–1172.

Bagdasaryan, G.P., Ghoukassyan, R.K., and Kazaryan, K.B., 1978, Comparative study of the age of old metamorphic schists in the Hakhoum River Basin (Armenian SSR) by means of K-Ar and Rb-Sr techniques, in Gorokhov, I.M., ed.,

Geochronology of the Eastern-European Platform and its Junction with the Caucasian-Carpathian System. Moscow, Nauka, p. 47–58. (in Russian).

Barrett, T.J., and MacLean, W.H., 1994, Chemostratigraphy and hydrothermal alteration in exploration for VHMS deposits in greenstones and younger volcanic rocks: Geological Association of Canada Short Course Notes, v. 11, p. 433–467.

Beaumont, C., 2006, Feasibility study in to the potential exploitation of Gold from the Central Mine open pit waste dumps, Kapan, Southern Armenia: Unpublished MSc Thesis, Exeter, UK, University of Exeter, 59 p.

Belov, A.A., 1968, On the history of tectonic development of the northern margin of the Iranian Elibaykal subplatform on Lesser Caucasus: Izvestia of the Academy of Sciences of SSSR, v. 10, p. 121-129 (in Russian).

Belov, A.A., 1969, Stratigraphy and structure of metamorphic volcanogenic and sedimentary stages of the Hanqavan-Zangezur fault in south-east Armenia: Byulleten Moskovskogo Obshchestva Ispytatelei Prirody (MOIP), Section Geology, v. XIV, p. 65–77 (in Russian).

Burtman, V.S., 1994, Meso-Tethyan oceanic sutures and their deformation: Tectonophysics, v. 234, p. 305-327.

Calder, M., 2014, Geological environment and genetic constraints of the Shamlugh ore deposit, Alaverdi district, Lesser Caucasus, Armenia: Unpublished MSc Thesis, Geneva, Switzerland, University of Geneva, 107 p.

Catchpole, H., Kouzmanov, K., Fontboté, L., Guillong, M., and Heinrich, C.A., 2011, Fluid evolution in zoned Cordilleran polymetallic veins - Insights from microthermometry and LA-ICP-MS of fluid inclusions: Chemical Geology, v. 281, p. 293–304.

Çagatay, M.N., and Eastoe, C.J., 1995, A sulfur isotope study of volcanogenic massive sulfide deposits of the Eastern Black Sea province, Turkey: Mineralium Deposita, v. 30, p. 55–66.

Chen, J., Papanastassiou, D., and Wasserburg, G., 1998. Re-Os systematics in chondrites and the fractionation of the platinum group elements in the early solar system. Geochimica et Cosmochimica Acta 62, 3379–3392.

Chew, D., and Spikings, R., 2015, Geochronology and thermochronology using apatite: Time and temperature, lower crust to surface: Elements, v. 11, p. 189-194.

Cholahyan, L.S., and Sarkisyan, R.A., 1972, About the lithology of volcanoclastic rocks of the upper Bajocian of the left bank or the river Kavart: Proceedings of the National Academy of Sciences of the Republic of Armenia, Earth Sciences, v. 25, p. 36–41 (in Russian).

Claypool, G.E., Holser, W.T., Kaplan, I.R., Sakai, H., and Zak, I., 1980, The age curves of sulfur and oxygen isotopes in marine sulfate and their mutual interpretation: Chemical Geology, v. 28, p. 199–260.

Cowgill, E., Forte, A.M., Niemi, N., Avdeev, B., Tye, A., Trexler, C., Javakhishvili, Z., Elashvili, M., Godoladze, T., 2016. Relict basin closure accommodates continental convergence with minimal crustal shortening or deceleration of plate motion as inferred from detrital zircon provenance in the Caucasus: Tectonics 35:2918–2947.

Craig, H., 1961, Isotopic variations in meteoric waters: Science, v. 133, p. 1702–1703.

Cunningham, C.G., Rye, R.O., Steven, T.A., and Mehnert, H.H., 1984, Origins and exploration significance of replacement and vein-type alunite deposits in the Marysvale volcanic field, west central Utah: Economic Geology, v. 79, p. 50–71.

Daliran, F., 2008, The carbonate rock-hosted epithermal gold deposit of Agdarreh, Takab geothermal field, NW Iran—hydrothermal alteration and mineralization: Mineralium Deposita, v. 43, p. 383-404.

Dalrymple, G.B., and Lanphere, M.A., 1974, $^{40}Ar/^{39}Ar$ age spectra of some undisturbed terrestrial samples: Geochimica et Cosmochimica Acta, v. 38, p. 715–738.

Davis, B.K., 2006, Report on the geology of the Kapan area with a focus on the Shahumyan deposit - Observations and interpretations based on a visit in September 2006: Unpublished report for Dundee Precious Metals, Kapan, Armenia, 48 p.

Delibaş, O., Moritz, R., Ulianov, A., Chiaradia, M., Saraç, C., Revan, M.K., and Göç, D., 2016, Cretaceous subduction-related magmatism and associated porphyry-type Cu-Mo mineralizations in the Eastern Pontides, Turkey: new constraints from geochronology and geochemistry: Lithos, v. 248-251, p. 119-137.

De Ronde, C., Hannington, M.D., Stoffers, P., Wright, I.C., Ditchburn, R.G., Reyes, A.G., Baker, E.T., Massoth, G.J., Lupton, J.E., Walker, S.L., Soong, C.W.R., Ishibashi, J., Lebon, G.T., Bray, C.J., and Resing, J.A., 2005, Evolution of a submarine magmatic-hydrothermal system: Brothers volcano, southern Kermadec arc, New Zealand: Economic Geology, v. 100, p. 1097-1133.

De Ronde, C.E.J., Massoth, G.J., Butterfield, D.A., Christenson, B.W., Ishibashi, J., Ditchburn, R.G., Hannington, M.D., Brathwaite, R.L., Lupton, J.E., Kamenetsky, V.S., Graham, I.J., Zellmer, G.F., Dziak, R.P., Embley, R.W., Dekov, V.M., Munnik, F., Lahr, J., Evans, L.J., and Takai, K., 2011, Submarine hydrothermal activity and gold-rich mineralization at Brothers Volcano, Kermadec Arc, New Zealand: Mineralium Deposita, v. 46, p. 541-584.

Djrbashyan, R.T., Guyumdjyan, H.P., and Tayan, R.N., 1976, Some features of the structure and formation of the Tertiary volcanic and sedimentary sequences of Zangezur (south-eastern part of Armenian SSR), *in* Volcanism and metallogeny of Armenian SSR: Yerevan, Publishing House of the Academy of Sciences of the Armenian SSR, v. 8, p. 60-77.

Einaudi, M.T., Hedenquist, J.W., and Inan, E.E., 2003, Sulfidation state of fluids in active and extinct hydrothermal systems: Transition from porphyry to epithermal environments: Society of Economic Geologists Special Publication, v. 10, p. 285–313.

Gabrielyan, A.A., Nazaretyan, S.N., and Ohannisyan, S.S., 1989, Deep faults of the territory of Armenia: Moscow, Nauka,

Geodynamics of the Caucasus, p. 36-45 (in Russian).

Galley, A.G., 1993, Semi-conformable alteration zones in volcanogenic massive sulphide districts: Journal of Geochemical Exploration, v. 48, p. 175-200.

Galley, A.G., 2003, Composite synvolcanic intrusions associated with Precambrian VMS- related hydrothermal systems: Mineralium Deposita, v. 38, p. 443-473.

Galley, A.G., Hannington, M.D., and Jonasson, I.R., 2007, Volcanogenic massive sulphide deposits. Mineral Deposits of Canada: A Synthesis of Major Deposit-Types, District Metallogeny, the Evolution of Geological Provinces, and Exploration Methods: Geological Association of Canada, Mineral Deposits Division Special Publication, v. 5, p. 141-161.

Galoyan, G., Rolland, Y., Sosson, M., Corsini, M., and Melkonyan, R., 2007. Evidence for superposed MORB, oceanic plateau and volcanic arc series in the Lesser Caucasus (Stepanavan, Armenia): Comptes Rendus Geoscience, v. 339, p. 482–492.

Galoyan, G., Rolland, Y., Sosson, M., Corsini, M., Billo, S., Verati, C., and Melkonyan, R., 2009, Geology, geochemistry and $^{40}Ar/^{39}Ar$ dating of Sevan ophiolites (Lesser Caucasus, Armenia): Evidence for Jurassic back-arc opening and hot spot event between the South Armenian Block and Eurasia: Journal of Asian Earth Sciences, v. 34, p. 135-153.

Gerstenberger, H., and Haase, G., 1997, A highly effective emitter substance for mass spectrometric Pb isotope ratio determinations: Chemical Geology, v. 136, p. 309–312.

Gevorkyan, R., and Aslanyan, A., 1997, Armenia, *in* Moores, E.M., Fairbridge, R.W., eds, Encyclopedia of European and Asian regional geology: London, Chapman and Hall, p. 26–34.

Giesemann, A., Jaeger, H.J., Norman, A.L., Krouse, H.R., and Brand, W.A., 1994, Online sulfur-isotope determination using an elemental analyzer coupled to a mass spectrometer: Analytical Chemistry, v. 66, p. 2816–2819.

Giggenbach, W.F., 1992, Magma degassing and mineral deposition in hydrothermal systems along convergent plate boundaries: Economic Geology, v. 87, p. 1927–1944.

Giggenbach, W.F., 1997, The origin and evolution of fluids in magmatic-hydrothermal systems, in Barnes, H.L., ed., Geochemistry of hydrothermal ore deposits, 3rd ed.: New York, Wiley, p. 737–796.

Golonka, J., 2004, Plate tectonic evolution of the southern margin of Eurasia in the Mesozoic and Cenozoic: Tectonophysics, v. 381, p. 235-273.

Grosjean, M., Moritz, R., Hovakimyan, S., Melkonyan, R., and Ulyanov, A., 2018, Cenozoic subduction to post-collision magmatic evolution of the Lesser Caucasus: new constraints from the Tejsar and Amulsar areas, Armenia: EGU General Assembly 2018 abstract.

Gugushvili, V., 2004, Two types of gold mineralization in the Bolnisi mining district related to Cretaceous volcanism: Proceedings of the Geological Institute of the Georgian Academy of Science New Series, v. 119, p. 749-755.

Hannington, M.D., 1997, The porphyry–epithermal–VMS transition: lessons from the Iskut River Area, British Columbia, and Modern Island Arcs. SEG Newsletter 29, 12–13.

Hannington, M., 2011, Metallogeny of Western Pacific submarine volcanic vents, *in* Barra, F., Reich, M., Campos, E., Tornos, F., eds, Let's talk ore deposits: Biennial SGA Meeting, 11th, Antofagasta, Chile, Proceedings, p. 13-15.

Hannington, M., de Ronde, C., and Petersen, S., 2005, Sea-floor tectonics and submarine hydrothermal systems: Economic Geology 100th Anniversary Volume, p. 111-141.

Hastie, A.R., Kerr, A.C., Pearce, J.A., and Mitchell, S.F., 2007, Classification of altered volcanic island arc rocks using immobile trace elements: development of the Th–Co discrimination diagram: Journal of Petrology, v. 48, p. 2341–2357.

Hassanpour, S., Alirezaei, S., Selby, D., and Sergeev, S., 2015, SHRIMP zircon U–Pb and biotite and hornblende Ar–Ar geochronology of Sungun, Haftcheshmeh, Kighal, and Niaz porphyry Cu–Mo systems: evidence for an early Miocene porphyry-style mineralization in northwest Iran: International Journal of Earth Sciences, v. 104, p. 45-59.

Hässig, M., Rolland, Y., Sosson, M., Galoyan, G., Müller, C., Avagyan, A., and Sahakyan, L., 2013a. New structural and petrological data on the Amasia ophiolites (NW Sevan–Akera suture zone, Lesser Caucasus): Insights for a large-scale obduction in Armenia and NE Turkey: Tectonophysics, v. 588, p. 135–153.

Hässig, M., Rolland, Y., Sosson, M., Galoyan, G., Sahakyan, L., Topuz, G., Celik O.F., Avagyan, A., and Müller, C., 2013b, Linking the NE Anatolian and Lesser Caucasus ophiolites: evidence for large-scale obduction of oceanic crust and implications for the formation of the Lesser Caucasus-Pontides Arc: Geodinamica Acta, v. 26, p. 311-330.

Hässig, M., Rolland, Y., Sahakyan, L., Sosson, M., Galoyan, G., Avagyan, A., Bosch, D., and Müller, C. 2015, Multi-stage metamorphism in the South Armenian Block during the Late Jurassic to Early Cretaceous: Tectonics over south-dipping subduction of Northern branch of Neotethys: Journal of Asian Earth Sciences, v. 102, p. 4-23.

Hemley, J.J., Montoya, J.W., Marinenko, J.W., and Luce, R.W., 1980, Equilibria in the system Al_2O_3-SiO_2-$H_2O$and some general implications for alteration/mineralization processes: Economic Geology, v. 75, p. 210–228.

Hemon, P., Moritz, R., and Ramazanov, V., 2012, The Gedabek epithermal Cu-Au deposit, Lesser Caucasus, Western Azerbaijan: Geology, alterations, petrography and evolution of the sulfidation fluid states [abs.]: SEG Conference, Lima, Peru, Poster 50.

Herrington, R., Maslennikov, V., Zaykov, V., and Seravkin, I., 2005a, VMS Deposits of the South Urals, Russia: Ore Geology Reviews, v. 27, p. 238-239.

Herrington, R., Maslennikov, V., Zaykov, V., Seravkin, I., Kosarev, A., Buschmann, B., Orgeval, J., Holland, N., Tesalina, S., Nimis, P., and Armstrong, R., 2005b, Classification of VMS deposits: Lessons from the South Uralides: Ore Geology Reviews, v. 27, p. 203-237.

Hoefs, J., 2009, Stable Isotope Geochemistry: Berlin, Springer, 286 p.

Holland, H.D., and Malinin, S.D., 1979, The solubility and occurrence of non-ore minerals, in Barnes, H.L., ed., Geochemistry of hydrothermal ore deposits, 2nd ed.: New York, Wiley, p. 461–508.

Huston, D.L., Relvas, J.M.R.S., Gemmell, J.B., and Drieberg, S., 2011, The role of granites in volcanic-hosted massive sulphide ore-forming systems: an assessment of magmatic–hydrothermal contributions: Mineralium Deposita, v. 46, p. 473-507.

Jankovic, S. 1977, The copper deposits and geotectonic setting of the Tethyan Eurasian metallogenic belt: Mineralium Deposita, v. 12, p. 37-47.

Jankovic, S. 1997, The Carpatho-Balkanides and adjacent area: a sector of the Tethyan Eurasian metallogenic belt: Mineralium Deposita, v. 32, p. 426-433.

Jones, C.E., Jenkyns, H.C., Coe, A.L., and Stephen, H.P., 1994, Strontium isotopic variations in Jurassic and Cretaceous seawater: Geochimica et Cosmochimica Acta, v. 58, p. 3061–3074.

Kajiwara, Y., and Krouse, H.R., 1971, Sulfur isotope partitioning in metallic sulfide systems: Canadian Journal of Earth Sciences, v. 8, p. 1397–1408.

Karamyan, K.A., 1978, Geology, structure and condition of formation copper-molybdenum deposits of Zangezur ore region: Yerevan, Publishing House of the Academy of Sciences Armenian SSR, 179 p. (in Russian).

Kasemann, S., Meixner, A., Rocholl, A., Vennemann, T., Rosner, M., Schmitt, A.K., and Wiedenbeck, M., 2001, Boron and oxygen isotope composition of certified reference materials NIST SRM 610/612 and reference materials JB-2 and JR-2: Geostandards Newsletter, v. 25, p. 405–416.

Kazmin, V., Sbortshikov, I., Ricou, L.E., Zonenshain, L., Boulin, J., and Knipper, A., 1986, Volcanic belts as markers of the Mesozoic-Cenozoic active margin of Eurasia: Tectonophysics, v. 123, p. 123–152.

Kekelia, S., Kekelia, M., Otkhmezuri, Z., Ozgür, N., and Moon, C., 2004, Ore-forming systems in volcanogenic-sedimentary sequences by the example of base metal deposits of the Caucasus and East Pontic Metallotect: Bulletin of Mineral Research and Exploration, v. 129, p. 1–16.

Kelley, S., 2002, K-Ar and Ar-Ar dating: Reviews in Mineralogy and Geochemistry, v. 47, p. 785–818.

Kerr, A., and Selby, D., 2012, The timing of epigenetic gold mineralization on the Baie Verte Peninsula, Newfoundland, Canada: new evidence from Re-Os pyrite geochronology: Mineralium Deposita, v. 47, p. 325–337.

Khachaturyan, E.A., 1977, The mineralogy, geochemistry and genesis of ores of pyrite formations of Armenian SSR: Publishing House of the Academy of Sciences of Armenian SSR, Yerevan, 316 p. (in Russian).

Khain, V.E., 1975, Structure and main stages in the tectono-magmatic development of the Caucasus: an attempt at geodynamic interpretation: American Journal of Science, v. 275-A, p. 131-156.

Knipper, A.L., and Khain, E.V., 1980, Structural position of ophiolites of the Caucasus: Ofioliti, v. 2, p. 297-314.

Koppers, A.A., 2002, ArArCALC-software for $^{40}Ar/^{39}Ar$ age calculations: Computers & Geosciences, v. 28, p. 605–619.

Kozerenko, S.V., 2004, Hydrothermal system of the Zod gold sulfide deposit, Armenia: Ore sources and formation conditions: Geochemistry International, v. 42, p. 188-190.

Large, R.R., McPhie, J., Gemmell, J.B., Herrmann, W., and Davidson, G.J., 2001, The spectrum of ore deposit types, volcanic environments, alteration halos, and related exploration vectors in submarine volcanic successions: some examples from Australia: Economic Geology, v. 96, p. 913–938.

Levitan, G., 2008, Gold deposits of the CIS: Bloomington, Indiana, Xlibris corporation, 352 p.

Lordkipanidze, M., Meliksetian, B., and Djarbashian, R., 1989, Mesozoic-Cenozoic magmatic evolution of the Pontian-Crimean-Caucasus region: Mémoire de la Société Géologique de France, v. 154, p. 103–124.

Ludwig, K.R., 1980, Calculation of uncertainties of U-Pb isotope data: Earth and Planetary Science Letters, v. 46, p. 212–220.

Ludwig, K.R., 2008, User's manual for Isoplot 3.70. A geochronological toolkit for Microsoft Excel: Berkeley Geochronology Center Special Publication no. 4, 76 p.

Lydian International, 2017, www.lydianinternational.co.uk.

Maghakyan, I.G., 1954, Metallogeny of Armenia: Yerevan, Publishing House of the Academy of Sciences of the Armenian SSR, 371 p. (in Russian).

Mathur, R., Ruiz, J., and Tornos, F., 1999, Age and sources of the ore at Tharsis and Rio Tinto, Iberian pyrite belt, from Re-Os isotopes: Mineralium Deposita, v. 34, p. 790–793.

Matveev, A., Spiridonov, E., Grigoryan, S., Tabatabaei, S., and Filimonov, S., 2006, Mineralogical and geochemical characteristics and predicted reserves of gold-base metal ore mineralization in southern Armenia and northwestern Iran: Geochemistry International, v. 44, p. 814–824.

Mayringer, F., Treloar, P.J., Gerdes, A., Finger, F., and Shengelia, D., 2011, New age data from the Dzirula Massif, Georgia: Implications for the evolution of the Caucasian Variscides: American Journal of Science, v. 311, p. 404-441.

Mederer, J., 2013, Regional setting, geological context and genetic aspects of polymetallic hydrothermal ore deposits from the Kapan ore district, southern Armenia: a contribution to the Mesozoic island arc metallogeny of the Lesser Caucasus: Geneva, ReproMail, 161 p.

Mederer, J., Moritz, R., Ulianov, A., and Chiaradia, M., 2013, Middle Jurassic to Cenozoic evolution of arc magmatism during Neotethys subduction and arc-continent collision in the Kapan Zone, southern Armenia: Lithos, v. 177, p. 61–78.

Mederer, J., Moritz, R., Zohrabyan, S.A., Vardanyan, A.V., Melkonyan, R.L., and Ulianov, A., 2014, Base and precious metal mineralization in Middle Jurassic rocks of the Lesser Caucasus - A review of geology and metallogeny and new data from the Kapan, Alaverdi and Mehmana districts: Ore Geology Reviews, v. 58, p. 185-207.

Mehrabi, B., Siani, M.G., Goldfarb, R., Azizi, H., Ganerod, M., and Marsh, E.E., 2016, Mineral assemblages, fluid evolution, and genesis of polymetallic epithermal veins, Glojeh district, NW Iran: Ore Geology Reviews, v. 78, p. 41-57.

Melkonyan, R., Chung, S.L., Ghukasyan, R.Kh., Galoyan, G., Khorenyan, R.H., and L.S, Atayan, L.S., 2016, The geology and isotope dating of the Tsav intrusive complex (Southern Armenia, Kapan terrain): Proceedings of the National Academy of Sciences of the Republic of Armenia, Earth Sciences, v. 69, p. 3-23 (in Russian with English abstract).

Migineishvili, R., 2005, Hybrid nature of the Madneuli Cu-Au deposit, Georgia: Geochemistry, Mineralogy and Petrology: Journal of the Bulgarian Academy of Sciences, v. 41, p. 128-132.

Moon, C.J., Gotsiridze, G., Gugushvili, V., Kekelia, M., Kekelia, S., Migineishvili, R., Otkhmezuri, Z., and Özgür, N., 2001, Comparison of mineral deposits between Georgian and Turkish sectors of the Tethyan metallogenic belt, in Piestrzynski, A., et al., eds, Mineral Deposits at the Beginning of the 21st Century, Proceedings 6th Biennial SGA Meeting, Krakow, Poland, p. 309–312.

Moritz, R., Melkonyan, R., Selby, D., Popkhadze, N., Gugushvili, V., Tayan, R., and Ramazanov, V., 2016a, Metallogeny of the Lesser Caucasus: From arc construction to postcollision evolution: Society of Economic Geologists Special Publication, v. 19, p. 157-192.

Moritz, R., Rezeau, H., Ovtcharova, M., Tayan, R., Melkonyan, R., Hovakimyan, S., Ramazanov V., Selby, D., Ulianov, A., Chiaradia, M., and Putlitz, B., 2016b, Long-lived, stationary magmatism and pulsed porphyry systems during Tethyan subduction to post-collision evolution in the southernmost Lesser Caucasus, Armenia and Nakhitchevan: Gondwana Research, v. 37, p. 465-503.

Nabatian, G., Wan, B., and Honarmand, M., 2017, Whole-rock geochemistry, molybdenite Re-Os geochronology, stable isotope and fluid inclusion investigations of the Siah-Kamar deposit, western Alborz-Azarbayjan: New constrains on the porphyry Mo deposit in Iran: Ore Geology Reviews, v. 91, p. 638-659.

Niroomand, S., Goldfarb, R.J., Moore, F Mohajjel, M., and Marsh, E.E., 2011, The Kharapeh orogenic gold deposit: geological, structural, and geochemical controls on epizonal ore formation in West Azerbaijan Province, Northwestern Iran: Mineralium Deposita, v. 46, p. 409-428.

Ohmoto, H., 1986, Stable isotope geochemistry of ore deposits: Reviews in Mineralogy and Geochemistry, v. 16, p. 491–560.

Ohmoto, H., and Lasaga, A.C., 1982, Kinetics of reactions between aqueous sulfates and sulfides in hydrothermal systems: Geochimica et Cosmochimica Acta, v. 46, p. 1727–1745.

Ohmoto, H., and Rye, R.O., 1979, Isotopes of sulfur and carbon, in Barnes, H.L., ed., Geochemistry of hydrothermal ore deposits, 2nd ed.: New York, Wiley, p. 509–567.

Ohmoto, H., and Goldhaber, M., 1997, Sulfur and carbon isotopes, in Barnes, H.L. ed., Geochemistry of hydrothermal ore deposits, 2nd ed.: New York, Wiley, p. 517–611.

Onishi, H., and Sandell, E., 1955, Geochemistry of arsenic: Geochimica et Cosmochimica Acta, v. 7, p. 1–33.

Onstott, T.C., Miller, M.L., Ewing, R.C., Arnold, G.W., Walsh, D.S., 1995, Recoil refinements: Implications for the $^{40}Ar/^{39}Ar$ dating technique: Geochimica et Cosmochimica Acta, v. 59, p. 1821-1834.

Peucker-Ehrenbrink, B., and Jahn, B-M., 2001, Rhenium-osmium isotope systematics and platinum group element concentrations: Loess and the upper continental crust: Geochemistry Geophysics Geosystems 2, 2001GC000172.

Polymetal International, 2017, https://www.polymetalinternational.com/en/assets/where-we-operate/kapan/#Reserves.

Popkhadze, N., Moritz, R., and Gugushvili, V., 2014, Architecture of Upper Cretaceous rhyodacitic hyaloclastite at the polymetallic Madneuli deposit, Lesser Caucasus, Georgia: Central European Journal of Geoscience, v. 6, p. 308-329.

Renne, P.R., Swisher, C.C., Deino, A.L., Karner, D.B., Owens, T.L., and DePaolo, D.J., 1998, Intercalibration of standards, absolute ages and uncertainties in $^{40}Ar/^{39}Ar$ dating: Chemical Geology, v. 145, p. 117–152.

Rezeau, H., Moritz, R., Wotzlaw, J.-F., Tayan, R., Melkonyan, R., Ulianov, A., Selby, D., d'Abzaz, F.-X., and Stern, R., 2016, Temporal and genetic link between incremental pluton assembly and pulsed porphyry Cu-Mo formation in accretionary orogens: Geology, v. 44, p. 627-630.

Rezeau, H., Moritz, R., Leuthold, J., Hovakimyan, S.E., Tayan, R.N, and Chiaradia, M., 2017, 30 Myr of Cenozoic magmatism along the Tethyan margin during Arabia–Eurasia accretionary orogenesis (Meghri–Ordubad pluton, southernmost Lesser Caucasus): Lithos, v. 288-289, p. 108–124.

Richards, J.P. 2015. Tectonic, magmatic, and metallogenic evolution of the Tethyan orogen: From subduction to collision: Ore Geology Reviews, v. 70, 323–345.

Richards, J.P., Wilkinson, D., and Ullrich, T., 2006, Geology of the Sari Gunay epithermal gold deposit, northwest Iran: Economic Geology, v. 101, p. 1455-1496.

Rolland, Y., 2017, Caucasus collisional history: review of data from East Anatolia to West Iran: Gondwana Research, v. 49, p. 130-146.

Rolland, Y., Billo, S., Corsini, M., Sosson, M., and Galoyan, G., 2009a, Blueschists of the Amassia-Stepanavan Suture Zone (Armenia): linking Tethys subduction history from E-Turkey to W-Iran: International Journal of Earth Sciences, v. 98, p. 533–550.

Rolland, Y., Galoyan, G., Bosch, D., Sosson, M., Corsini, M., Fornari, M., and Vérati, C., 2009b, Jurassic Back-arc and hot-spot related series in the Armenian ophiolites – implications for the obduction process: Lithos, v. 112, p. 163–187.

Rolland, Y., Galoyan, G., Sosson, M., Melkonyan, R., and Avagyan, A., 2010, The Armenian ophiolite: insights for Jurassic back-arc formation, Lower Cretaceous hot spot magmatism and Upper Cretaceous obduction over the South Armenian Block: Geological Society London Special publication, v. 340, p. 353-382.

Rolland, Y., Sosson, M., Adamia, Sh., and Sadradze, N., 2011, Prolonged Variscan to Alpine history of an active Eurasian margin (Georgia, Armenia) revealed by $^{40}Ar/^{39}Ar$ dating: Gondwana Research, v. 20, p. 798-815.

Ruiz, J., and Mathur, R., 1999, Metallogenesis in continental margins: Re-Os evidence from porphyry copper deposits in Chile: Reviews in Economic Geology, v. 12, p. 59–72.

Ruiz, J., Jones, L.M., and Kelly, W.C., 1984, Rubidium-strontium dating of ore deposits hosted by Rb-rich rocks, using calcite and other common Sr-bearing minerals: Geology, v. 12, p. 259–262.

Rusk, B.G., Reed, M.H., and Dilles, J.H., 2008, Fluid inclusion evidence for magmatic-hydrothermal fluid evolution in the porphyry copper-molybdenum deposit at Butte, Montana: Economic Geology, v. 103, p. 307–334.

Rye, R.O., 1993, The evolution of magmatic fluids in the epithermal environment; the stable isotope perspective: Economic Geology, v. 88, p. 733–752.

Rye, R.O., 2005, A review of the stable-isotope geochemistry of sulfate minerals in selected igneous environments and related hydrothermal systems: Chemical Geology, v. 215, p. 5–36.

Rye, R.O., Bethke, P.M., and Wasserman, M.D., 1992, The stable isotope geochemistry of acid sulfate alteration: Economic Geology, v. 87, p. 225–262.

Sarkisyan, R.A., 1970, About the presence of different age subvolcanic dacite quartz porphyries in Kapan ore field: Proceedings of the National Academy of Sciences of the Republic of Armenia, Earth Sciences, v. 23, p. 13–17 (in Russian).

Savin, S.M., and Epstein, S., 1970, The oxygen and hydrogen isotope geochemistry of clay minerals: Geochimica et Cosmochimica Acta, v. 34, p. 25–42.

Schmidt, A.I., Sher, L.S., Portnoy, A.L.,and Minyn, D.A., 1985, Perfection of the methods of large scale prognosis of pyrite, copper–molybdenum and gold mineralization on the basis of structural–formational analysis of long-term areas of Kapan ore bearing zone of Armenian SSR. Central Research Institute of Geological Prospecting for Base and Precious Metals (TsNIGRI). Ministry of Natural Resources, Russia, Moscow (in Russian).

Selby, D., Kelley, K.D., Hitzman, M.W., and Zieg, J., 2009, Re-Os sulfide (bornite, chalcopyrite, and pyrite) systematics of the carbonate- hosted copper deposit at Ruby Creek, southern Brooks Range, Alaska: Economic Geology, v. 104, p. 437–444.

Sharp, Z., Atudorei, V., and Durakiewicz, T., 2001, A rapid method for determination of hydrogen and oxygen isotope ratios from water and hydrous minerals: Chemical Geology, v. 178, p. 197–210.

Shengelia, D.M., Tsutsunava, T.N., and Shubitidze, L.G., 2006, New data on structure, composition, and regional metamorphism of the Tsakhkunyats and Akhum-Asrikchai massifs, the Lesser Caucasus: Doklady Earth Sciences, v. 409A, p. 900-904.

Shirey, S.B., and Walker, R.J., 1998, The ReOs isotope system in cosmochemistry and high-temperature geochemistry: Annual Review of Earth and Planetary Sciences, v. 26, p. 423–500.

Sillitoe, R.H., 2010, Porphyry copper systems: Economic Geology, v. 105, p. 3–41.

Simmonds, V., Moazzen, M., and Mathur, R., 2017, Constraining the timing of porphyry mineralization in northwest Iran in relation to Lesser Caucasus and Central Iran; Re-Os age data for Sungun porphyry Cu-Mo deposit: International geology Review, v. 59, p. 1561-1574.

Simmons, S.F., White, N.C., and John, D.A., 2005, Geological characteristics of epithermal precious and base metal deposits: Economic Geology 100th Anniversary Volume, p. 485-522.

Sosson, M., Rolland, Y., Müller, C., Danelian, T., Melkonyan, R., Kekelia, S., Adamia, S., Babazadeh, V., Kangarli, T., Avagyan, A., Galoyan, G., and Mosar, J., 2010, Subductions, obduction and collision in the Lesser Caucasus (Armenia, Azerbaijan, Georgia), new insights: Geological Society of London Special Publications, v. 340, p. 329–352.

Spötl, C., and Vennemann, T.W., 2003, Continuous-flow isotope ratio mass spectrometric analysis of carbonate minerals: Rapid Communications in Mass Spectrometry, v. 17, p. 1004–1006.

Stein, H.J., Sundblad, K., Markey, R.J., Morgan, J.W., and Motuza, G., 1998, Re-Os ages for Archean molybdenite and pyrite, Kuittila-Kivisuo, Finland and Proterozoic molybdenite, Kabeliai, Lithuania: Testing the chronometer in a metamorphic and metasomatic setting: Mineralium Deposita, v. 33, p. 329–345.

Stein, H.J., Morgan, J.W., and Scherstén, A., 2000, Re-Os dating of low-level highly radiogenic (LLHR) sulfides: The Harna¨s gold deposit, southwest Sweden, records continental-scale tectonic events: Economic Geology, v. 95, p. 1657–1671.

Stoffregen, R.E., Rye, R.O., and Wasserman, M.D., 1994, Experimental studies of alunite: I. ^{18}O-^{16}O and D-H fractionation factors between alunite and water at 250-450 °C: Geochimica et Cosmochimica Acta, v. 58, p. 903–916.

Tayan, R.N., Plotnikov, E.P., and Abdurakhmanov, R.U., 1976, Some features of emplacement of geological structure of the Zangezur-Nakhichevan region of Lesser Caucasus: Proceedings of the National Academy of Sciences of the Republic of Armenia, Earth Sciences, v. 29, p. 12-20 (in Russian).

Taylor, B.E., 1988, Degassing of rhyolitic magmas: Hydrogen isotope evidence and implications for magmatic-hydrothermal ore deposits: Canadian Institute of Mining and Mineralogy Special Volume, v. 39, p. 33–49.

Taylor, H.P., 1974, The application of oxygen and hydrogen isotope studies to problems of hydrothermal alteration and ore deposition: Economic Geology, v. 69, p. 843–883.

Todt, W., Cliff, R., Hanser, A., and Hofmann, A., 1996, Evaluation of a ^{202}Pb-^{205}Pb double spike for high-precision lead isotope analysis: Geophysical Monograph Series, v. 95, p. 429-437.

Torró, L., Proenza, J.A., Melgarejo, J.C., Alfonso, P., Farré de Pablo, J., Colomer, J.M., García-Casco, A., Gubern, A., Gallardo, E., Cazañas, X., Chávez, C., Del Carpio, R., Leónf, P., Nelson, C.E., Lewis, J.F., 2016, Mineralogy, geochemistry and sulfur isotope characterization of Cerro de Maimón (Dominican Republic), San Fernando and Antonio (Cuba) lower Cretaceous VMS deposits: Formation during subduction initiation of the proto-Caribbean lithosphere within a fore-arc: Ore Geology Reviews, v. 72, p. 794–817.

Tumanyan, G.A., 1992, Peculiarities of structure and position of Kapan anticlinorium: Proceedings of the National Academy of Sciences of the Republic of Armenia, Earth Sciences, v. 45, p. 3–11 (in Russian).

Vennemann, T., and O'Neil, J., 1993, A simple and inexpensive method of hydrogen isotope and water analyses of minerals and rocks based on zinc reagent: Chemical Geology, v. 103, p. 227–234.

Wasserman, M.D., Rye, R.O., Bethke, P.M., and Arribas, A., Jr., 1992, Methods for separation and total stable isotope analysis of alunite: U.S. Geological Survey Open-File Report 92-9, 20 p.

Wolfe, B., and Gossage, B., 2009, Technical report for the Kapan project, Kapan, Armenia: unpublished report, Perth, Australia, Coffey Mining Pty Ltd on behalf of Deno Gold Mining Company CJSC, 270 p.

Wood, D., Noble, M., Standing, J., and Outhwaite, M., 2008, Observations and interpretations from mapping in the Kapan region, Armenia: Unpublished report, Kapan, Armenia, JIGSAW Geoscience for Dundee Precious Metals, 23 p.

Yigit, O., 2009, Mineral deposits of Turkey in relation to Tethyan metallogeny: Implications for future mineral exploration: Economic Geology, v. 104, p. 19-51.

Zakariadze, G.S., Dilek, Y., Adamia, S.A., Oberhänsli, R.E., Karpenko, S.F., Bazylev, B.A., and Solov'eva, N., 2007, Geochemistry and geochronology of the Neoproterozoic Pan-African Transcaucasian Massif (Republic of Georgia) and implications for island arc evolution of the late Precambrian Arabian-Nubian shield: Gondwana Research, v. 11, p. 92-108.

Zamani, G.B., and Masson, F., 2014, Recent tectonics of East (Iranian) Azerbaijan from stress state reconstructions: Tectonophysics, v. 611, p. 61–82.

Zartman, R., and Doe, B., 1981, Plumbotectonics-the model: Tectonophysics, v. 75, p. 135–162.

Zheng, Y., 1990, Carbon-oxygen isotopic covariation in hydrothermal calcite during degassing of CO_2: Mineralium Deposita, v. 25, p. 246–250.

Zheng, Y., 1991, Sulphur isotopic fractionation between sulphate and sulphide in hydrothermal ore deposits: disequilibrium vs equilibrium processes: Terra Nova, v. 3, p. 510–516.

Zheng, Y., 1993, Calculation of oxygen isotope fractionation in anhydrous silicate minerals: Geochimica et Cosmochimica Acta, v. 57, p. 1079–1091.

Zheng, Y., 1999, Oxygen isotope fractionation in carbonate and sulfate minerals: Geochemical Journal, v. 33, p. 109–126.

Zheng, Y., and Hoefs, J., 1993, Carbon and oxygen isotopic covariations in hydrothermal calcites: Mineralium Deposita, v. 28, p. 79–89.

Zohrabyan, S.A., 2005, New Concepts on Stratigraphy of Middle Jurassic Sediments in Southeastern Zangezur: Proceedings of the National Academy of Sciences of the Republic of Armenia, Earth Sciences, v. 58, p. 17–22 (in Russian with English abstract).

Zohrabyan, S.A., and Melkonyan, R.L., 1999, Role of structural factors in localization of mineralization in pyrite deposits of the Alaverdi–Kapan zone: Proceedings of the National Academy of Sciences, Republic of Armenia, Earth Sciences, v. 52, p. 31–40 (in Russian with English abstract).

Zohrabyan, S.A., Mirzoyan, G.G., and Sarkisyan, N.A., 2003, Bartsravan ore field - geology, structure, ore mineralization: Proceedings of the National Academy of Sciences of the Republic of Armenia, Earth Sciences, v. 56, p. 30–38 (in Russian with English abstract).

Figure Captions

Fig. 1: Geological map of the central part of the Tethyan belt between eastern Turkey and northern Iran modified from Mederer et al. (2014) with additional information from Azizi and Moinevaziri (2009), Hässig et al. (2013a, b), and Zamani and Masson (2014), and location of major ore districts, deposits and prospects. Location of Figure 2 is centered on the Kapan region in the southernmost Lesser Caucasus. The Lesser Caucasus consists of the Somkheto-Karabagh belt along the Eurasian margin, the ophiolites of the Amasia-Sevan-Akera suture zone and the South Armenian block. Abbreviations: ABV-Artvin-Bolnisi volcanic-arc; ATV-Adjara-Trialeti belt; IAES-Izmir-Ankara-Erzinkan suture; KB-Kapan block; KGF-Khustup-Giratagh fault; MOP-Meghri-Ordubad pluton. Sources of location and description of selected ore districts, deposits and prospects: Eastern Pontides and Madenkoy, Turkey from Yigit (2009); Lesser Caucasus from Moritz et al. (2016a); and Iranian sources are Simmonds et al. (2017) for Sungun, Mazraeh and Saheb, Nabatian et al. (2017) for Siah Kamar, Mehrabi et al. (2016) for the Glojeh district, Daliran (2008) for the Zarshuran-Aghdareh district, Richards et al. (2006) for Sari Guney, and Niroomand et al. (2011) for Kharapeh and the Qolqoleh-Karvian district.

Fig. 2: Geological map of the southern part of the Lesser Caucasus (modified from Mederer et al., 2014), showing the location of the study area and of major ore deposits and prospects of the Kapan zone and the adjacent Cenozoic Meghri-Ordubab and Bargushat plutons of the South Armenian block. A - Agarak Cu-Mo porphyry deposit. B - Bartsravan polymetallic prospect. D - Dastakert porphyry Cu-Mo deposit. K - Kadjaran porphyry Cu-Mo deposit. KGF - Khustup-Giratakh fault. P - Paragachay porphyry Cu-Mo deposit. SAB – South Armenian Block (Gondwana derived). S - Shikahogh Cu-Au-Mo prospect.

Fig. 3: Geological map of the Kapan mining district, compiled from the geological maps of Achikgiozyan et al. (1987) and Wood et al. (2008). Veins shown are hosted by volcanic and volcaniclastic rocks of the Middle Jurassic magmatic complex and are projected towards the surface (unpublished data by the Deno Gold geology department, 2010).

Fig. 4: Simplified synthetic lithostratigraphic column of the Kapan district, based on a compilation from Achikgiozyan et al. (1987), Zohrabyan (2005), Wood et al. (2008) and Mederer et al. (2013). The positions of the Shahumyan (SHA) and Centralni (CEN) deposits within Middle Jurassic rocks of the Kapan district and of the Bartsravan polymetallic (BAR) and Shikahogh Cu-Au-Mo (SHI) prospects in Late Jurassic to Early Cretaceous rocks are also shown.

Fig. 5: Compiled geochemical whole rock data for rocks from the Middle Jurassic and Late Jurassic-Early Cretaceous magmatic complexes from the Kapan district (Mederer et al. 2013, 2014). **a –**Th/Yb vs. Ta/Yb discrimination diagram from Hastie et al. (2007) **b –**Zr vs. Y discrimination diagram from Barrett and MacLean (2004).

Fig. 6: **a** - Schematic cross-section of the central part of the Kapan district based on compiled geological maps from Achikgiozyan et al. (1987), Wood et al. (2008) and own field observations. Ages obtained in this study are also shown. The debated Re-Os age obtained from pyrite of the Centralni East deposit as well as the $^{40}Ar/^{39}Ar$ age obtained from alunite of the northeastern limb of the Shahumyan deposit are indicated by a question mark. **b** - Cross-section through the Shahumyan deposit based on historical data, summarized in 2004 by the Deno Gold geology department.

Fig. 7: Mineralization style, textures and mineral associations at the Centralni West deposit. **a –** East-West oriented and 75° south-dipping quartz-chalcopyrite-pyrite vein (photograph kindly provided by Alan Turner, Deno Gold mining engineer). **b -** Pyrite, chalcopyrite, quartz and carbonate constitute the matrix of Middle Jurassic brecciated lava. **c** - Minor galena in chalcopyrite- and pyrite-dominated vein from high-grade (~10 wt. % Cu) copper ore (plain-polarized reflected light microscopy), the sulfides occur within a quartz-carbonate gangue (not shown in the Figure). **d** - Chalcopyrite-pyrite vein in chlorite-carbonate-epidote altered andesitic hyaloclastite host rock. Abbreviations: ccp = chalcopyrite, gn = galena, py = pyrite.

Fig. 8: Mineralization style, textures and mineral associations at the Centralni East deposit. **a -** Stockwork-style mineralization in altered quartz-dacite. **b -** Colusite replacing pyrite. **c** - Galena associated with chalcopyrite and tennantite. b

and c: plain-polarized reflected light microscopy. Abbreviations: ccp = chalcopyrite, col= colusite, gn = galena, py = pyrite, tnt = tennantite-tetrahedrite.

Fig. 9: Mineralization style, textures and mineral associations at the Shahumyan deposit. **a -** Polymetallic vein hosted by altered quartz-dacite of the Barabatoom Formation. **b -** Clast-rotated monomict breccia in a high-grade ore vein of the Shahumyan deposit (see hammer for scale in the bottom left part of the photograph). Bottom part between the orange lines: quartz-dacite clasts are rimmed by cockade bands of sphalerite, quartz and carbonate. Top part, above the orange line: the adjacent wall-rock is irregularly altered along cracks resulting in a pseudo-breccia. **c -** Galena and tennantite-tetrahedrite associated with chalcopyrite. **d -** Inclusions of enargite and chalcopyrite in pyrite. **e -** Telluride droplet-shaped inclusions along fractures in quartz I with sericite and quartz II, and associated krennerite and altaite (plain-polarized transmitted light microscopy). **f -** Altaite, hessite and petzite associated with chalcopyrite and sphalerite in a multiphase inclusion in pyrite. c,d and f: plain-polarized reflected light microscopy. Abbreviations: ccp = chalcopyrite, enr = enargite, gn = galena, py = pyrite, qz = quartz, ser = sericite, sl = sphalerite, tnt = tennantite-tetrahedrite.

Fig. 10: Mineral paragenetic succession for **a -** Centralni West, **b -** Centralni East, **c -** polymetallic veins from the Shahumyan deposit and **d -** the northeastern flank of the Shahumyan deposit. Thick bars indicate increased mineral abundance and dashed lines subsidiary mineral abundance.

Fig. 11: Textures and mineral associations of samples used for $^{40}Ar/^{39}Ar$ dating. **a -** Hand specimen of banded magmatic-steam alunite in contact with altered quartz-dacite. **b -** Magmatic-hydrothermal alunite, which occurs in vugs and in the matrix of altered quartz-dacite. **c -** Hydrothermal muscovite and pyrite in contact with the altered host rock. **d -** Zoned igneous plagioclase. b to d: crossed-polarized transmitted light photographs. Abbreviations: alu = alunite, hem = hematite, ms = muscovite, pl = plagioclase, py = pyrite, qz = quartz.

Fig. 12: Crosscutting relationships between diabase dikes and mineralization in the Kapan district. **a -** Post-mineralization diabase dike cuts a zoned polymetallic vein in the Shahumyan deposit. **b -** Plan view sketch map adapted from Achikgiozyan et al. (1987) from the Centralni East deposit. An enclave of mineralization is hosted by the diabase dike and ductile deformation affects the mineralized vein in proximity to the cross-cutting dike. The direction of ductile deformation is indicated by the red arrow. **c -** Polished sample of chalcopyrite-pyrite-quartz-carbonate mineralization cut by a diabase dike from the Centralni West deposit (sample kindly provided by Sergej Zohrabyan, Yerevan). Note the well-developed and continuous chilled margin of the crosscutting dike along the contact with the Middle Jurassic host rock (brecciated lava) but also along the contact with mineralization. Abbreviations: cb = carbonate, ccp = chalcopyrite, py = pyrite, qz = quartz.

Fig. 13: Lead isotopic compositions of sulfides and alunite from the Kapan mining district. The initial Pb isotopic ratios of igneous rocks from the Kapan district are plotted for reference (age corrected for 161-145 Ma, Mederer et al., 2013). The Pb isotopic evolution curves for the mantle (OR), upper crust (UC) and lower crust (LC) are from Zartman and Doe (1981).

Fig. 14: Initial Nd and Sr isotopic compositions of magmatic rocks from the Late Jurassic-Early Cretaceous magmatic complex and the Middle Jurassic igneous rocks that were age-corrected for 161-145 Ma (data from Mederer et al., 2013). The ranges of Sr isotopic composition of hydrothermal calcite from the Shahumyan and Centralni West deposits and the Sr isotopic composition of 170-140 Ma old seawater are also shown (data from Jones et al., 1994).

Fig. 15: Summary of $\delta^{34}S$ values for sulfides and sulfates from the Kapan mining district. The sulfur isotopic composition of Jurassic marine sulfates (16±1.5‰; Claypool et al., 1980) is displayed for the Centralni East deposit, where barite and gypsum have been analyzed. Abbreviations: alu = alunite, brt = barite, ccp = chalcopyrite, gn = galena, gp = gypsum, py = pyrite, sl = sphalerite.

Fig. 16: Oxygen isotopic composition of quartz from the Kapan district.

Fig. 17: **a -** C- and O- and **b -** Sr- and O-isotopic compositions of calcites from the Centralni West and Shahumyan deposits.

Fig. 18: $^{40}Ar/^{39}Ar$ age spectra for **a -** hydrothermal muscovite from Centralni West, **b -** magmatic-hydrothermal alunite from Shahumyan **c -** igneous plagioclase from Shahumyan host rock **d -** magmatic-steam alunite from Shahumyan.

Fig. 19: $^{187}Re/^{188}Os$ vs. $^{187}Os/^{188}Os$ (**a -**), ^{187}Re vs. $^{187}Os^{r}$ (**b -**) and weighted average model age plots (**c -**) for the Centralni West deposit. $^{187}Re/^{188}Os$ vs. $^{187}Os/^{188}Os$ (**d -**), ^{187}Re vs. $^{187}Os^{r}$ (**e -**) and weighted average model age plots (**f -**) for the Centralni East deposit. All diagrams were generated using the Isoplot v.4.1 Excel macro (Ludwig, 2008) and all uncertainties are shown at 2σ level. See text for discussion and additional information.

Fig 20: **a -** Calculated $\delta^{18}O$ values of fluids in equilibrium with hydrothermal quartz and calcite at temperatures of 400 to 150°C. See text for details. **b -** δD, $\delta^{18}O_{SO4--}$, $\delta^{18}O_{OH-}$ and $\delta^{18}O_{tot}$ values for vein- and disseminated alunite from the Kapan mining district. Fluid compositions (δD_{H2O} and δO_{H2O}) in equilibrium with alunite are calculated from equations of Stoffregen et al. (1994) at 150 to 400°C. Meteoric Water Line from Craig (1961), Kaolinite Line from Savin and Epstein (1970), Primary Magmatic Water box (PMW) from Taylor (1974), Felsic Magmatic Fluids from Taylor (1988), Volcanic Vapor box, i.e. range of water compositions discharged from high-temperature fumaroles, from Giggenbach (1992) and SMOW is standard mean oceanic water (Taylor, 1974; Hoefs, 2003).

Fig. 21: Summary of igneous and hydrothermal events in the Kapan district from Middle Jurassic to Early Cretaceous. The uncertain Re-Os isochron age obtained from pyrite of the Centralni East deposit and the $^{40}Ar/^{39}Ar$ age obtained from alunite of the northeastern limb of the Shahumyan deposit are indicated by a question mark. See text for details.

Fig. 22: Proposed sequences of geological and ore forming events in the Kapan mining district from the Middle Jurassic to the Early Cretaceous. a – Broadly coeval Middle Jurassic metallogenic events with volcanogenic massive sulfide ore formation at Centralni West at 161.78±0.79 Ma and formation of porphyry-epithermal systems at Centralni East and Shahumyan before the late Oxfordian, based on the evidence that ore bodies are only hosted by Middle Jurassic magmatic rocks and do not extend across the late Oxfordian unconformity. b – Middle Jurassic volcanogenic massive sulfide ore formation at Centralni West at 161.78±0.79 Ma, followed by late Oxfordian erosion and Late Jurassic ore formation during arc thickening and slab roll-back at Shahumyan and Centralni East if one accepts the questionable $^{40}Ar/^{39}Ar$ and Re-Os ages from both deposits (see text for discussion). Both scenarios are followed by Late Cretaceous intrusions, including the Tsav intrusion, and stockwork-type Cu-Au-Mo mineralization at the Shikahokh prospect. Scenario a) is considered as more likely based on field relationships.

Figure 1

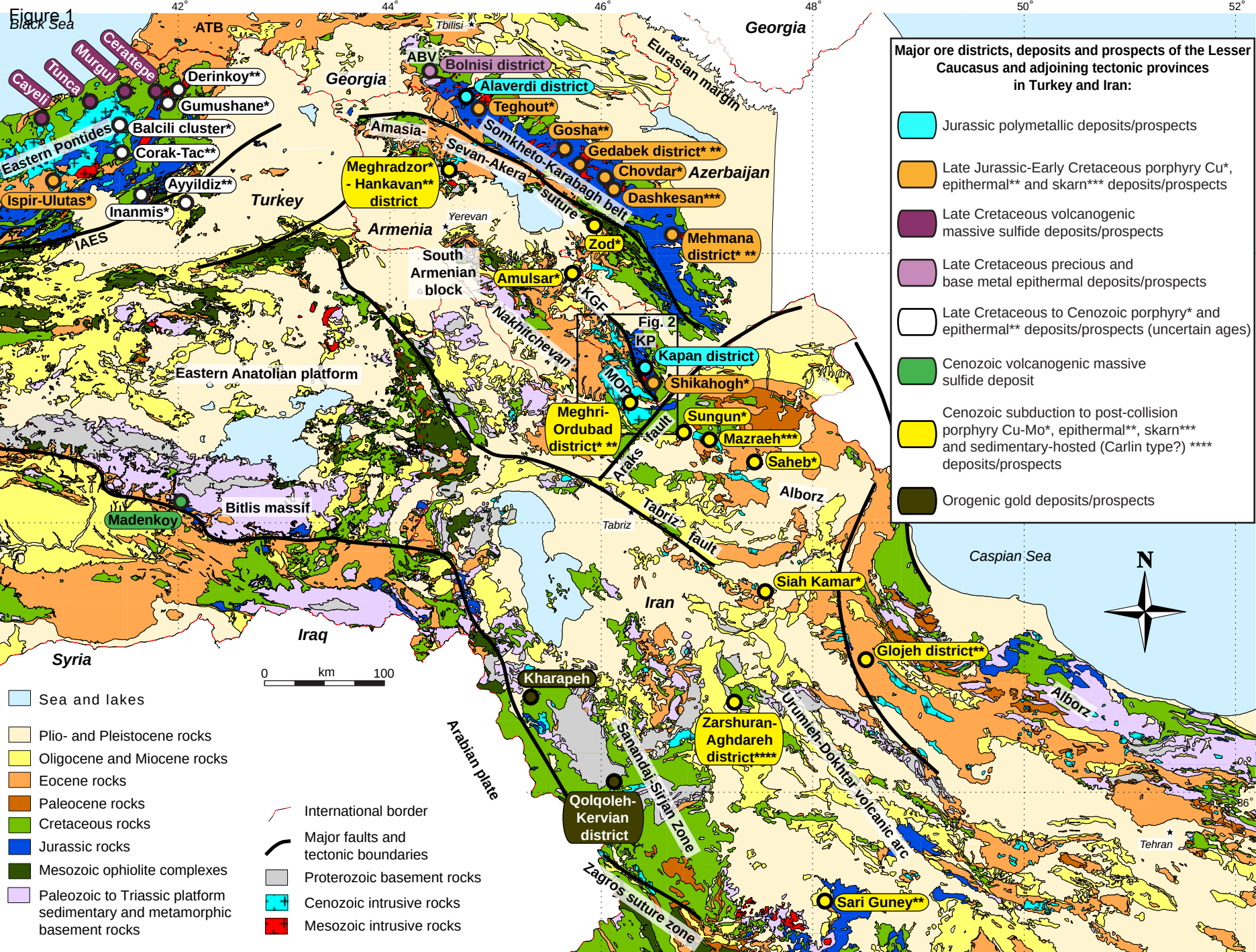
Black Sea
ATB
Tbilisi
Georgia
Eurasian margin
ABV
Bolnisi district
Alaverdi district
Teghout*
Gosha**
Gedabek district* **
Chovdar*
Dashkesan***
Azerbaijan
Somkheto-Karabagh belt
Sevan-Akera suture
Amasia-
Meghradzor* - Hankavan** district
Mehmana district* **
Zod*
Amulsar*
Yerevan
Armenia
South Armenian block
KGF
Nakhitchevan
Fig. 2
KP
Kapan district
Shikahogh*
MOP
Meghri-Ordubad district* **
Sungun*
Mazraeh***
Saheb*
Araks fault
Tabriz fault
Tabriz
Alborz
Caspian Sea
N
Siah Kamar*
Iran
Glojeh district**
Alborz
Urumieh-Dokhtar volcanic arc
Zarshuran-Aghdareh district****
Sanandaj-Sirjan Zone
Kharapeh
Qolqoleh-Kervian district
Arabian plate
Zagros suture zone
Sari Guney**
Tehran
Iraq
Syria
Eastern Anatolian platform
Bitlis massif
Madenkoy
Turkey
Eastern Pontides
Cayeli
Tunca
Murgul
Cerattepe
Derinkoy**
Gumushane*
Balcili cluster*
Corak-Tac**
Ayyildiz**
Inanmis*
Ispir-Ulutas*
IAES
0 km 100
Major ore districts, deposits and prospects of the Lesser Caucasus and adjoining tectonic provinces in Turkey and Iran:
Jurassic polymetallic deposits/prospects
Late Jurassic-Early Cretaceous porphyry Cu*, epithermal** and skarn*** deposits/prospects
Late Cretaceous volcanogenic massive sulfide deposits/prospects
Late Cretaceous precious and base metal epithermal deposits/prospects
Late Cretaceous to Cenozoic porphyry* and epithermal** deposits/prospects (uncertain ages)
Cenozoic volcanogenic massive sulfide deposit
Cenozoic subduction to post-collision porphyry Cu-Mo*, epithermal**, skarn*** and sedimentary-hosted (Carlin type?) **** deposits/prospects
Orogenic gold deposits/prospects
Sea and lakes
Plio- and Pleistocene rocks
Oligocene and Miocene rocks
Eocene rocks
Paleocene rocks
Cretaceous rocks
Jurassic rocks
Mesozoic ophiolite complexes
Paleozoic to Triassic platform sedimentary and metamorphic basement rocks
International border
Major faults and tectonic boundaries
Proterozoic basement rocks
Cenozoic intrusive rocks
Mesozoic intrusive rocks

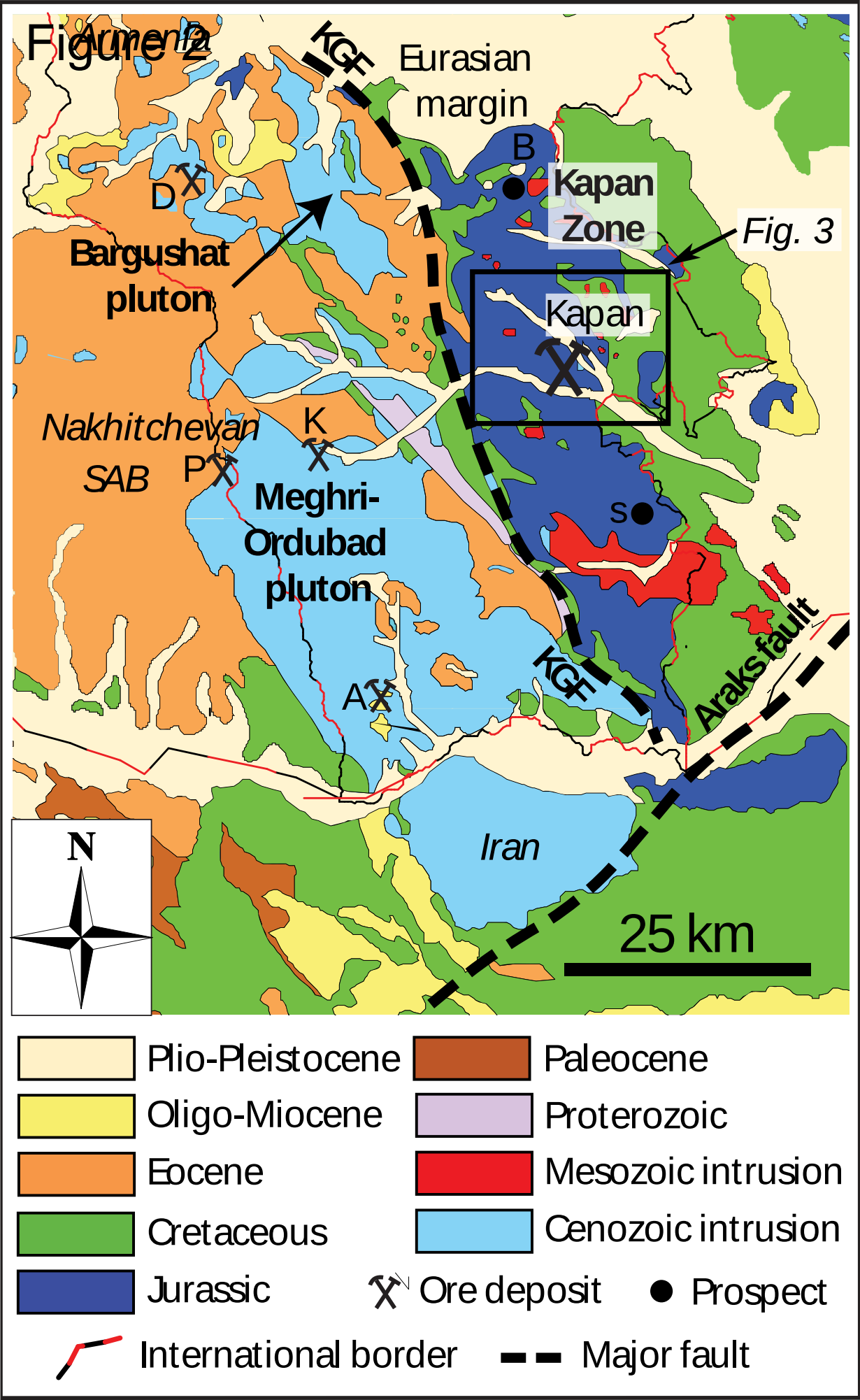
Figure 2
Armenia
KGF
Eurasian margin
B
Kapan Zone
Fig. 3
D
Bargushat pluton
Kapan
Nakhitchevan SAB
K
P
Meghri-Ordubad pluton
S
A
KGF
Araks fault
Iran
N
25 km
Plio-Pleistocene
Oligo-Miocene
Eocene
Cretaceous
Jurassic
Paleocene
Proterozoic
Mesozoic intrusion
Cenozoic intrusion
Ore deposit
Prospect
International border
Major fault

Figure 3

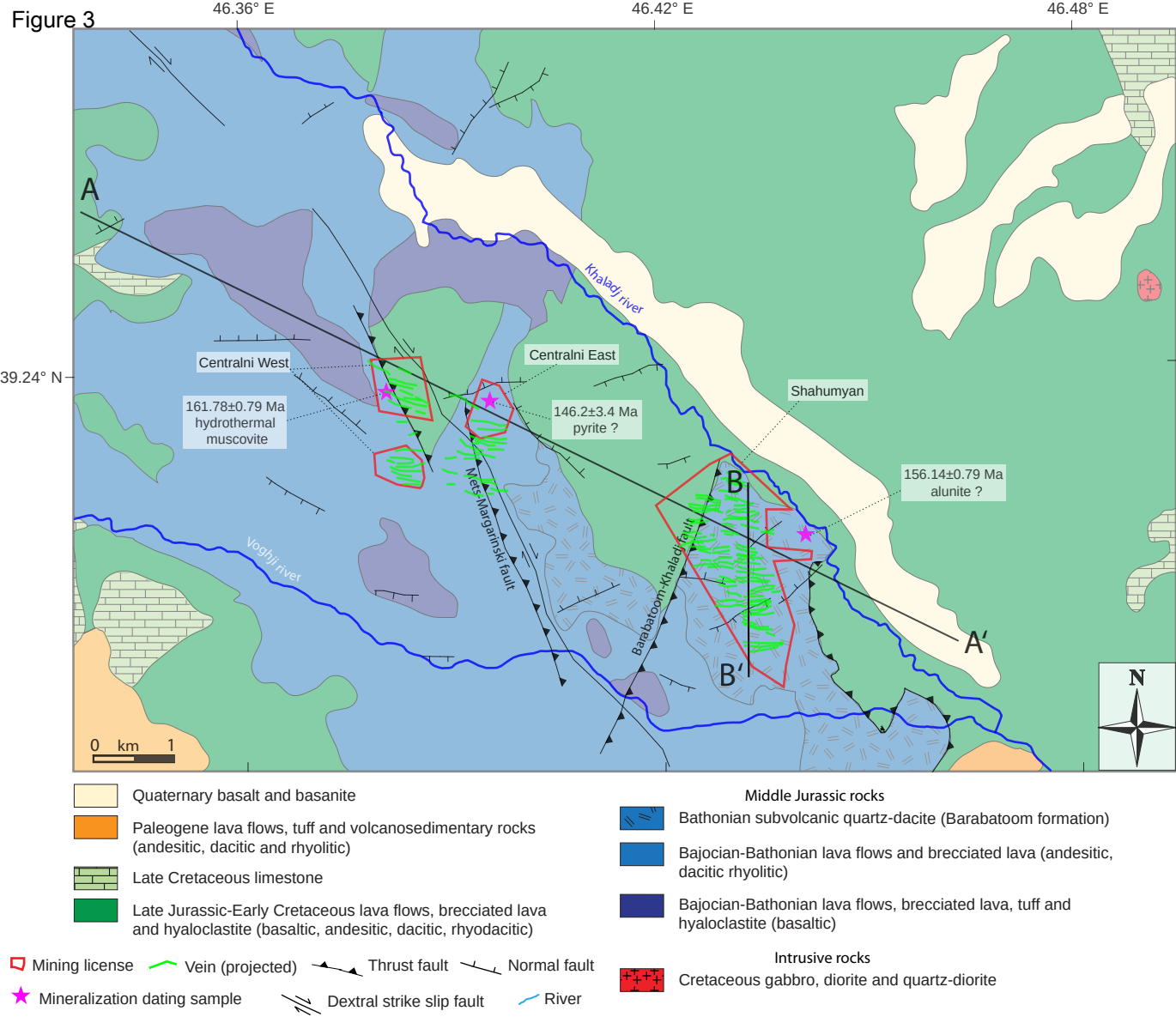
46.36° E
46.42° E
46.48° E
39.24° N
A
A′
B
B′
Khaladj river
Voghji river
Centralni West
Centralni East
Shahumyan
161.78±0.79 Ma
hydrothermal
muscovite
146.2±3.4 Ma
pyrite ?
156.14±0.79 Ma
alunite ?
Mets-Margahnski fault
Barabatoom-Khaladj fault
0 km 1
N
Quaternary basalt and basanite
Paleogene lava flows, tuff and volcanosedimentary rocks (andesitic, dacitic and rhyolitic)
Late Cretaceous limestone
Late Jurassic-Early Cretaceous lava flows, brecciated lava and hyaloclastite (basaltic, andesitic, dacitic, rhyodacitic)
Middle Jurassic rocks
Bathonian subvolcanic quartz-dacite (Barabatoom formation)
Bajocian-Bathonian lava flows and brecciated lava (andesitic, dacitic rhyolitic)
Bajocian-Bathonian lava flows, brecciated lava, tuff and hyaloclastite (basaltic)
Intrusive rocks
Cretaceous gabbro, diorite and quartz-diorite
Mining license
Vein (projected)
Thrust fault
Normal fault
Mineralization dating sample
Dextral strike slip fault
River

Figure 4

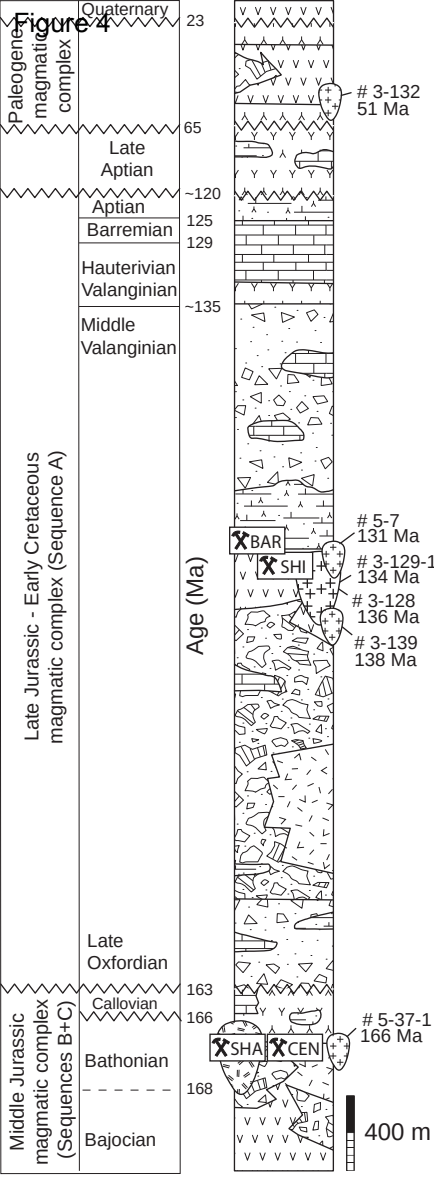

limestone

calcareous sandstone

tuffaceous sandstone, sandstone, mergel and limestone

lava flows

volcanic breccia or agglomerate

hyaloclastite

tuff and volcanosedimentary rock

tuff and ignimbrite

intrusive rock

subvolcanic quartz-dacite (Barabatoom Formation)

unconformity

ore deposit

Figure 5

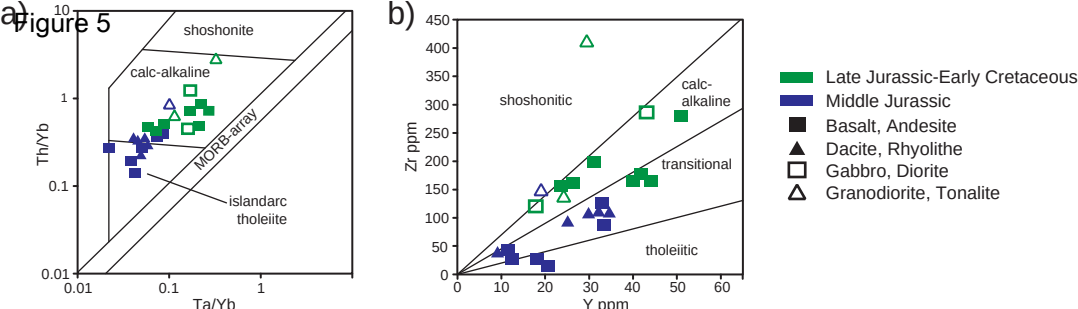
a)
shoshonite
calc-alkaline
MORB-array
islandarc
tholeiite
Th/Yb
Ta/Yb
10
1
0.1
0.01
0.01
0.1
1
b)
shoshonitic
calc-
alkaline
transitional
tholeiitic
Zr ppm
Y ppm
450
400
350
300
250
200
150
100
50
0
0
10
20
30
40
50
60
Late Jurassic-Early Cretaceous
Middle Jurassic
Basalt, Andesite
Dacite, Rhyolithe
Gabbro, Diorite
Granodiorite, Tonalite

Figure 6

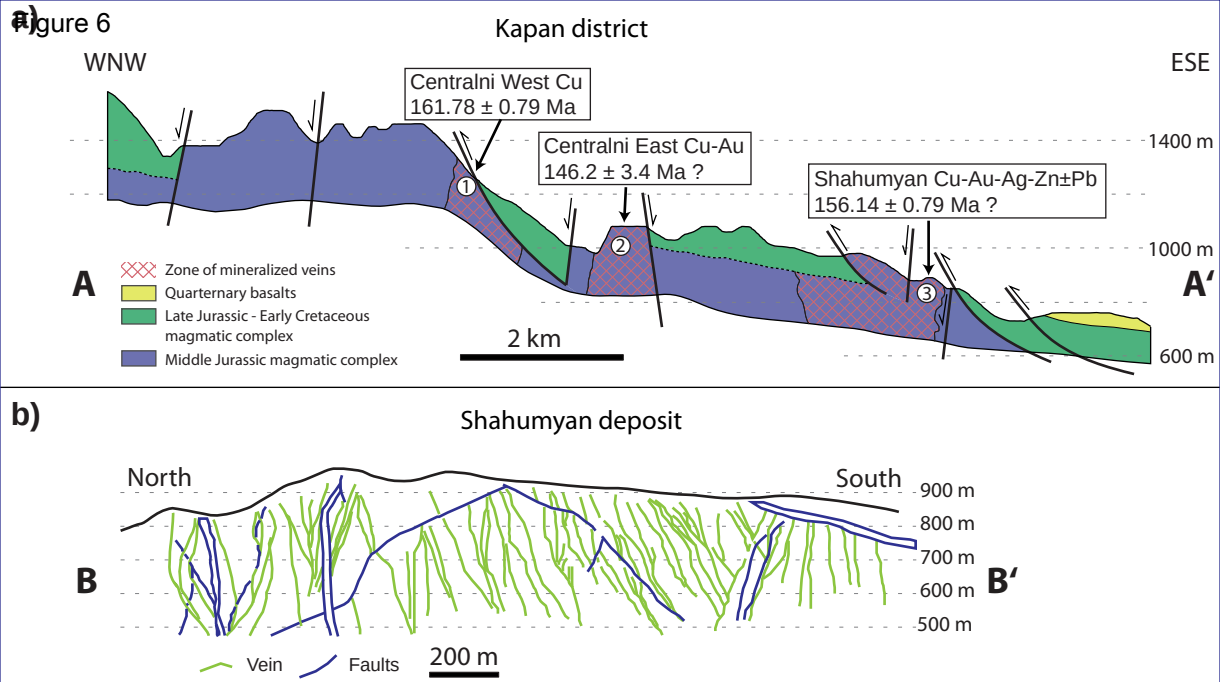
a)
Kapan district
WNW
ESE
Centralni West Cu
161.78 ± 0.79 Ma
Centralni East Cu-Au
146.2 ± 3.4 Ma ?
Shahumyan Cu-Au-Ag-Zn±Pb
156.14 ± 0.79 Ma ?
1400 m
1000 m
600 m
A
A'
Zone of mineralized veins
Quarternary basalts
Late Jurassic - Early Cretaceous magmatic complex
Middle Jurassic magmatic complex
2 km
b)
Shahumyan deposit
North
South
900 m
800 m
700 m
600 m
500 m
B
B'
Vein
Faults
200 m

Figure 7

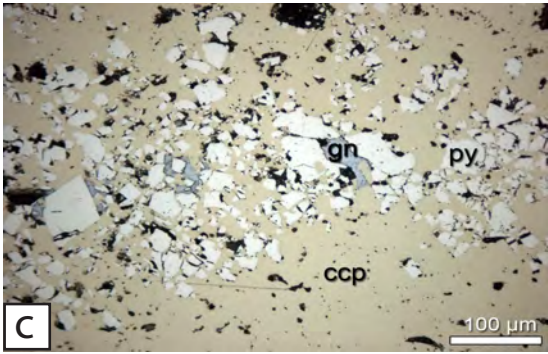

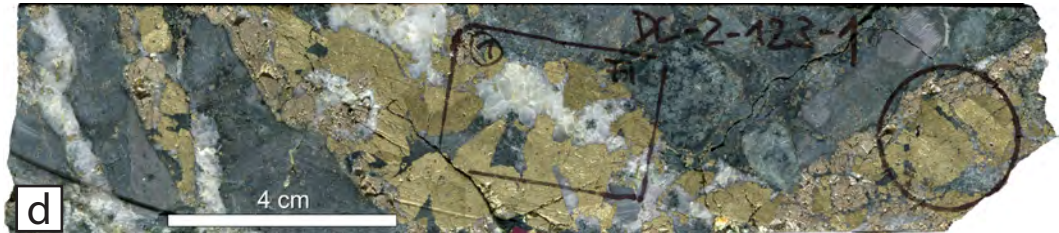

Figure 8

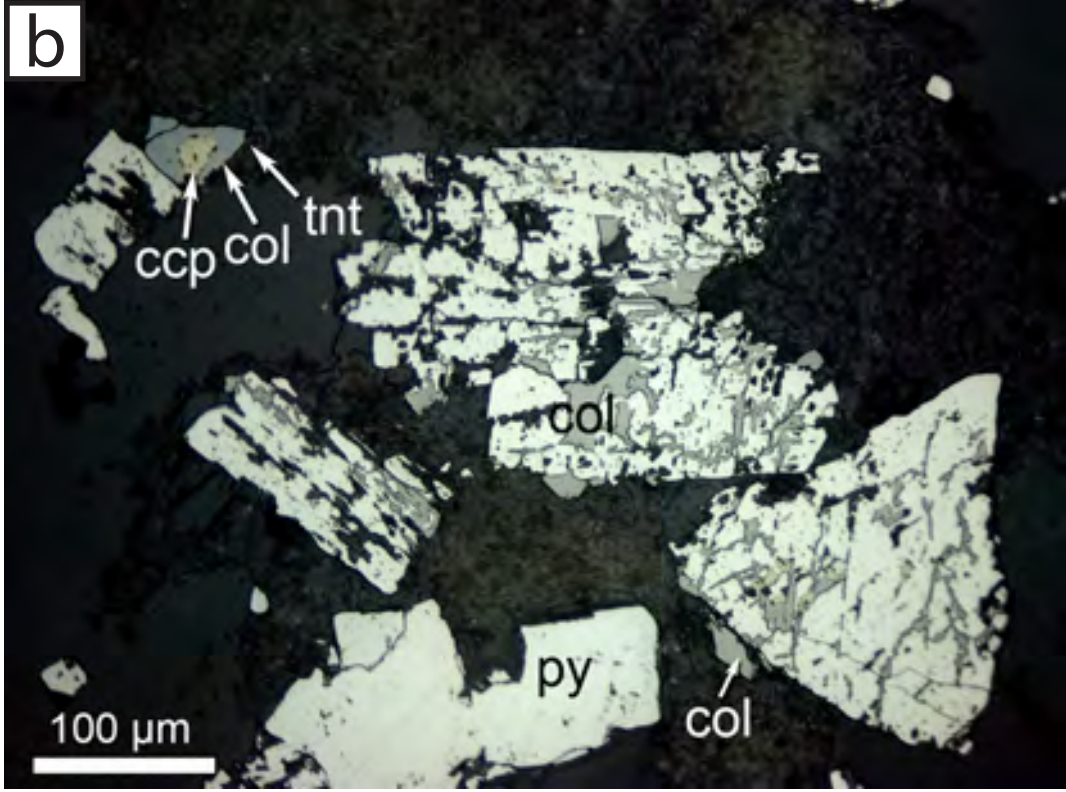

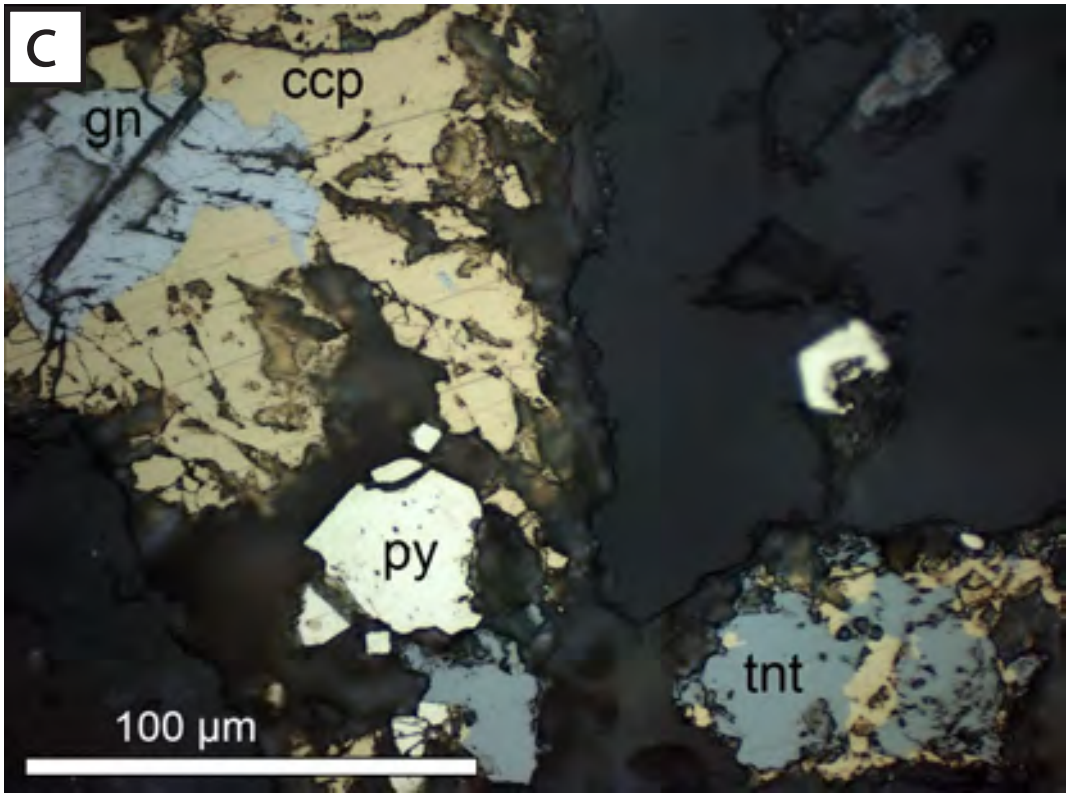

Figure 9

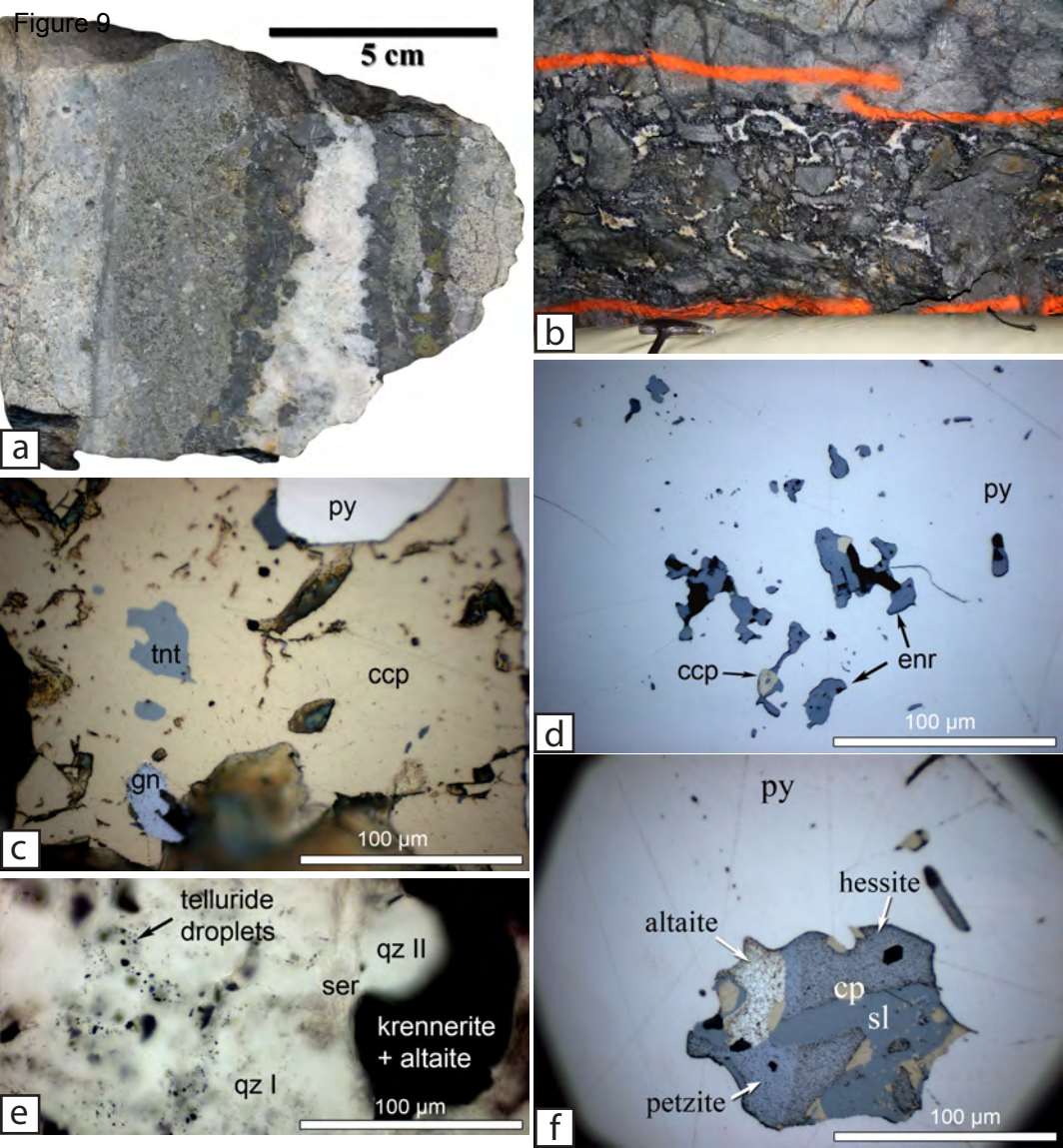
5 cm
a
b
py
tnt
ccp
gn
100 µm
c
py
ccp
enr
100 µm
d
telluride
droplets
qz II
ser
krennerite
+ altaite
qz I
100 µm
e
py
hessite
altaite
cp
sl
petzite
100 µm
f

Figure 10

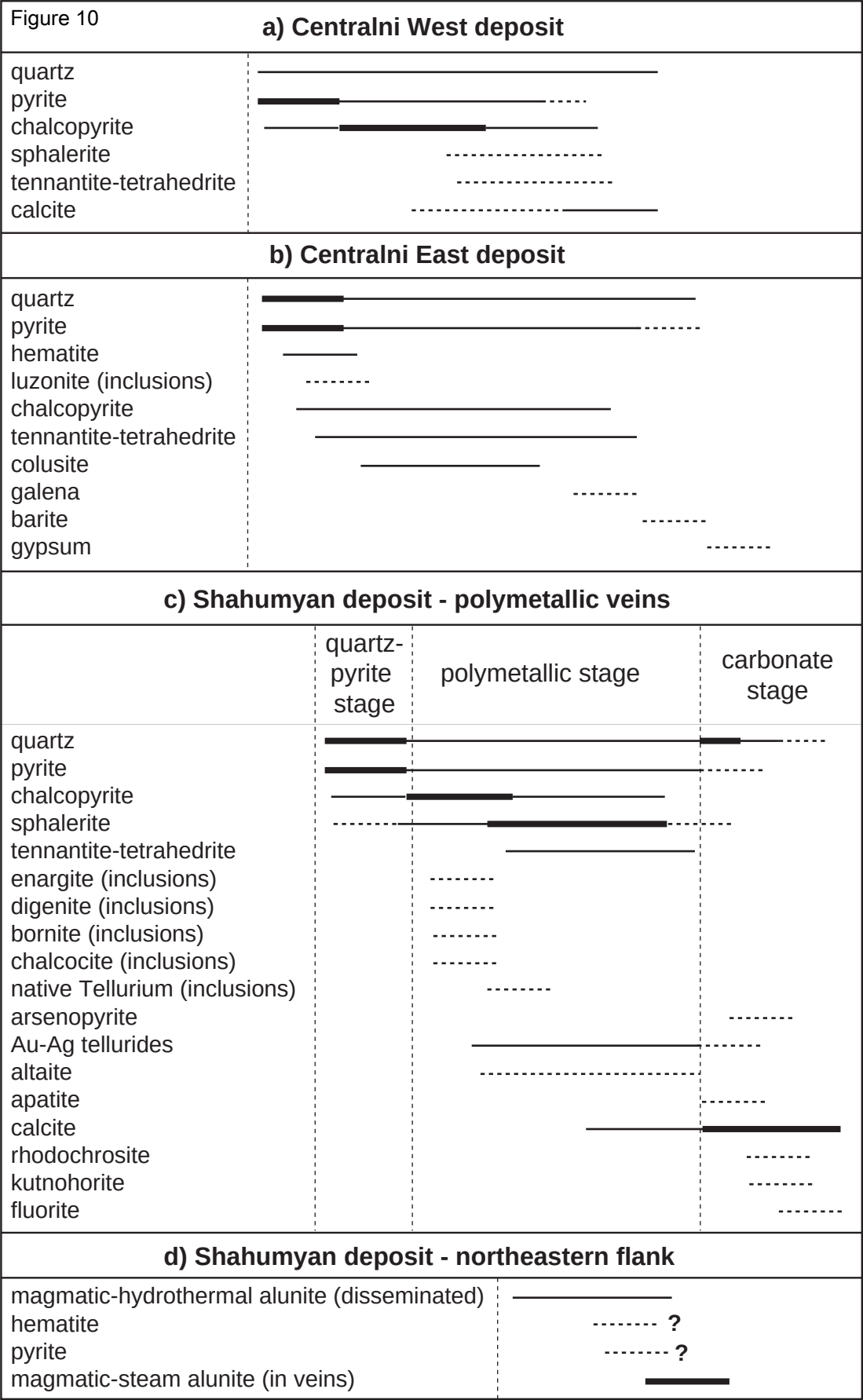
a) Centralni West deposit
quartz
pyrite
chalcopyrite
sphalerite
tennantite-tetrahedrite
calcite
b) Centralni East deposit
quartz
pyrite
hematite
luzonite (inclusions)
chalcopyrite
tennantite-tetrahedrite
colusite
galena
barite
gypsum
c) Shahumyan deposit - polymetallic veins
quartz-pyrite stage
polymetallic stage
carbonate stage
quartz
pyrite
chalcopyrite
sphalerite
tennantite-tetrahedrite
enargite (inclusions)
digenite (inclusions)
bornite (inclusions)
chalcocite (inclusions)
native Tellurium (inclusions)
arsenopyrite
Au-Ag tellurides
altaite
apatite
calcite
rhodochrosite
kutnohorite
fluorite
d) Shahumyan deposit - northeastern flank
magmatic-hydrothermal alunite (disseminated)
hematite
?
pyrite
?
magmatic-steam alunite (in veins)

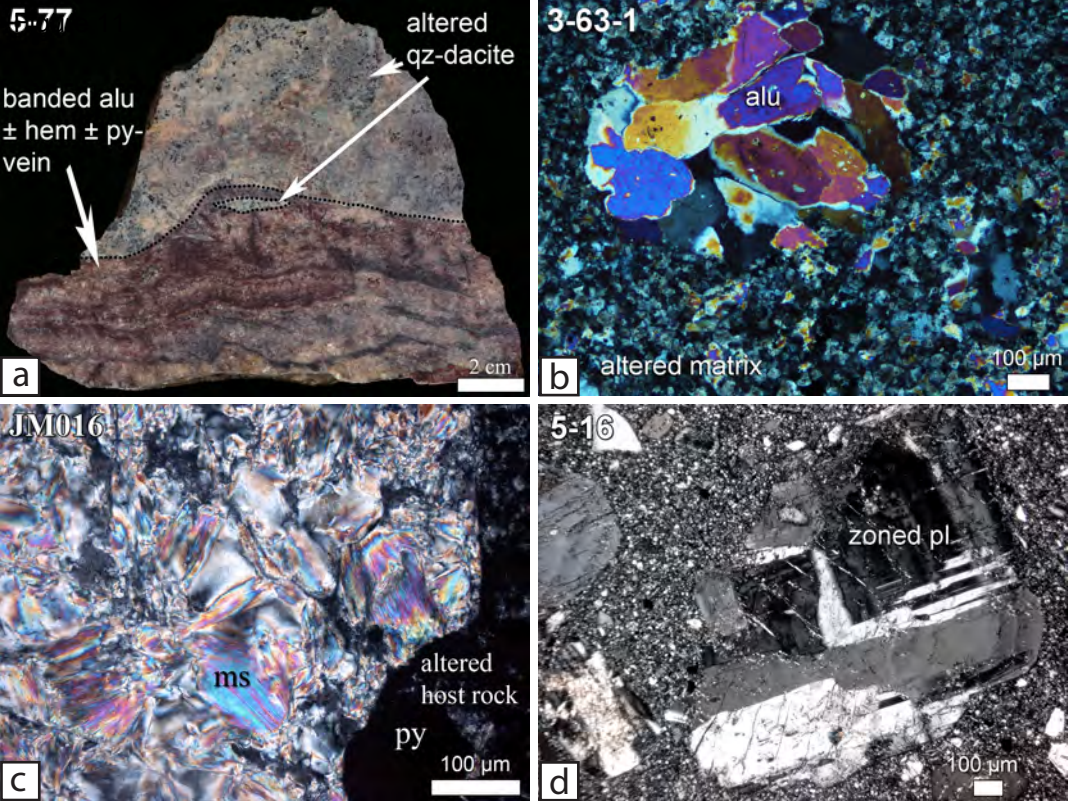
5-77
altered
qz-dacite
banded alu
± hem ± py-
vein
2 cm
a
3-63-1
alu
altered matrix
100 µm
b
JM016
ms
altered
host rock
py
100 µm
c
5-16
zoned pl
100 µm
d

Figure 12


diabase
dike
zoned
vein
a

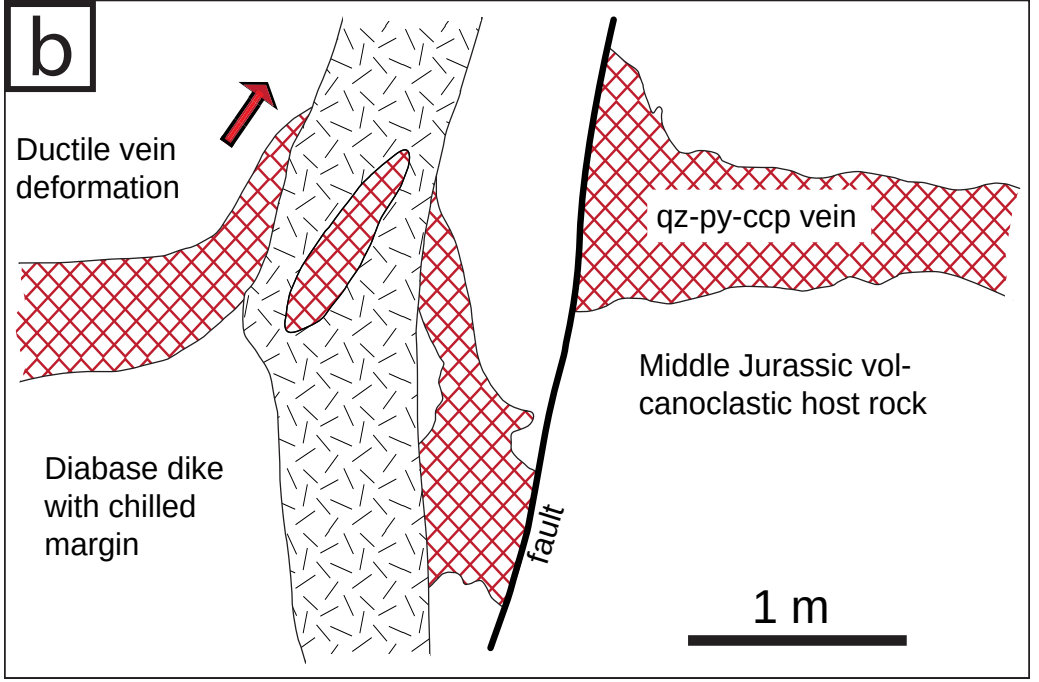
b
Ductile vein
deformation
qz-py-ccp vein
Middle Jurassic vol-
canoclastic host rock
Diabase dike
with chilled
margin
fault
1 m

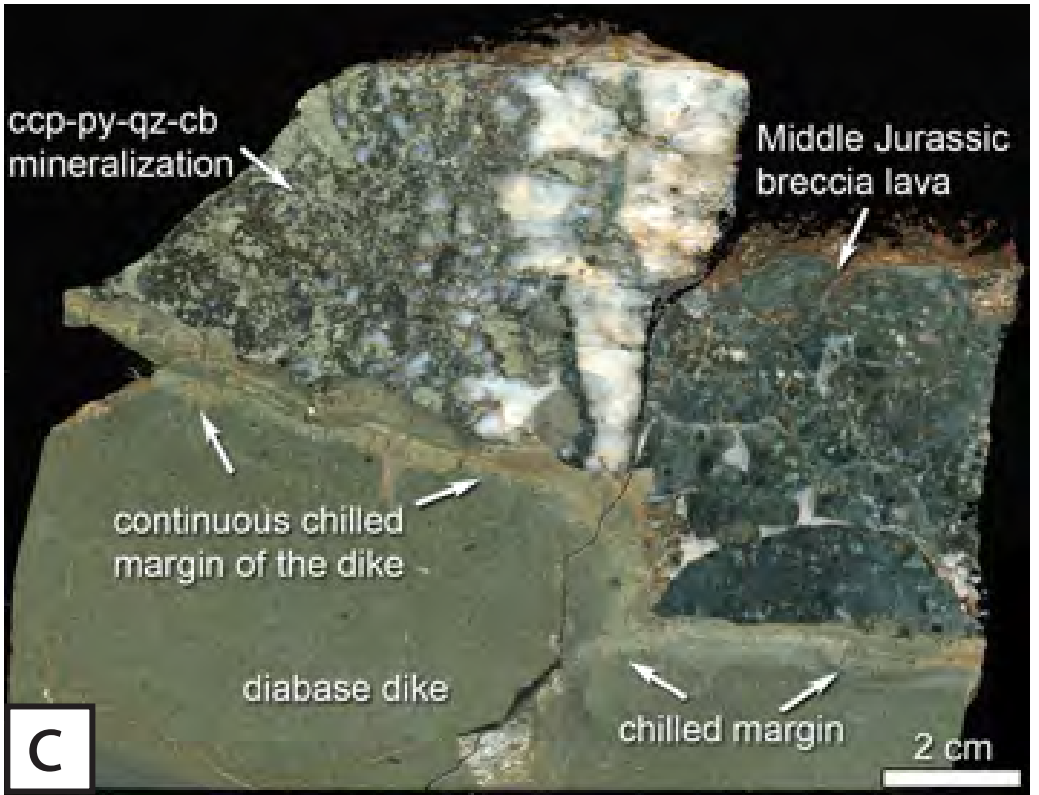
ccp-py-qz-cb
mineralization
Middle Jurassic
breccia lava
continuous chilled
margin of the dike
diabase dike
chilled margin
2 cm
c

Figure 13

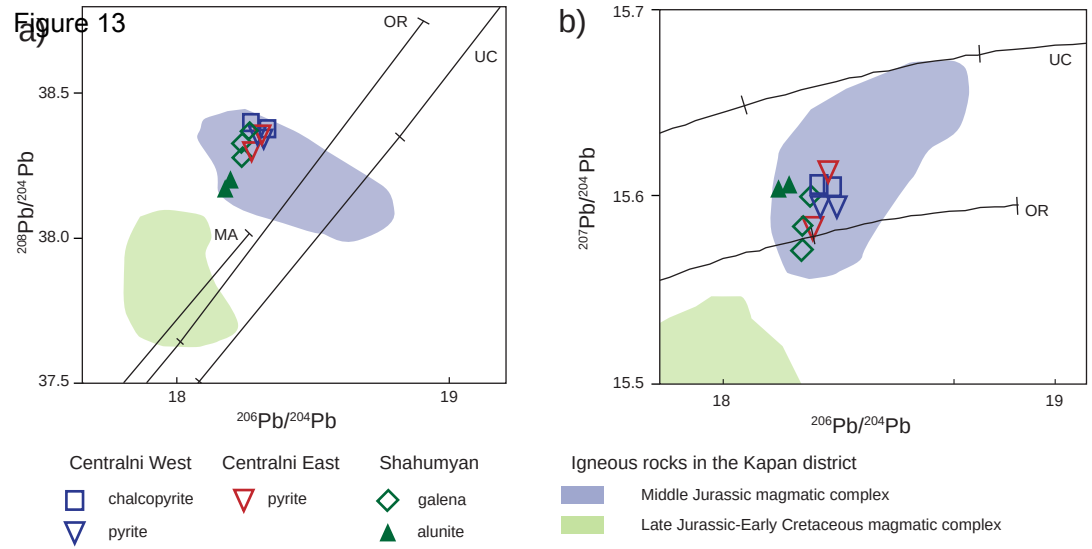
a)
OR
UC
MA
38.5
38.0
37.5
18
19
$^{208}Pb/^{204}Pb$
$^{206}Pb/^{204}Pb$
b)
15.7
15.6
15.5
UC
OR
18
19
$^{207}Pb/^{204}Pb$
$^{206}Pb/^{204}Pb$
Centralni West
chalcopyrite
pyrite
Centralni East
pyrite
Shahumyan
galena
alunite
Igneous rocks in the Kapan district
Middle Jurassic magmatic complex
Late Jurassic-Early Cretaceous magmatic complex

Figure 14

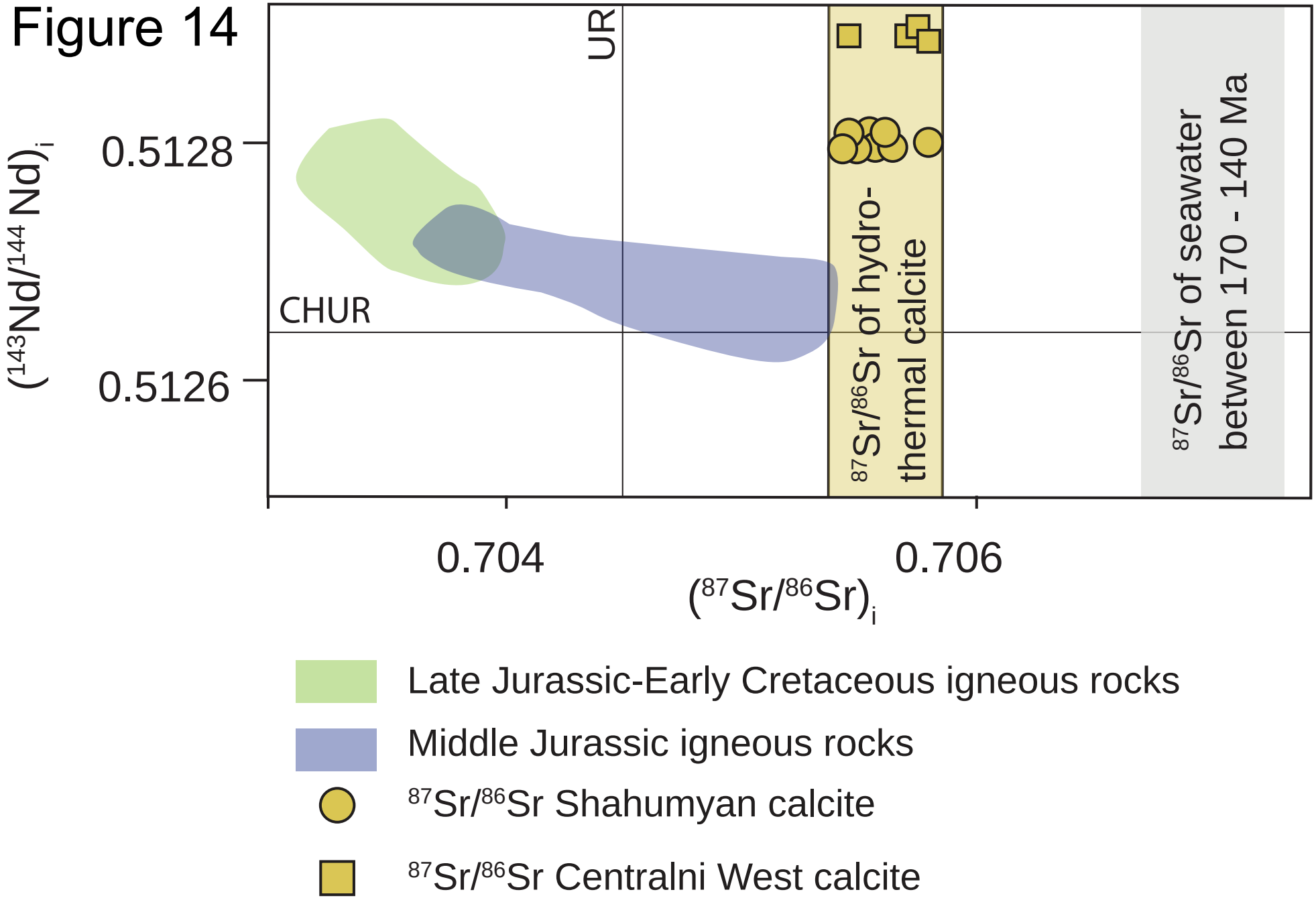
UR
CHUR
0.5128
0.5126
$(^{143}Nd/^{144}Nd)_i$
0.704
0.706
$(^{87}Sr/^{86}Sr)_i$
$^{87}Sr/^{86}Sr$ of hydro-thermal calcite
$^{87}Sr/^{86}Sr$ of seawater between 170 - 140 Ma
Late Jurassic-Early Cretaceous igneous rocks
Middle Jurassic igneous rocks
$^{87}Sr/^{86}Sr$ Shahumyan calcite
$^{87}Sr/^{86}Sr$ Centralni West calcite

Figure 15

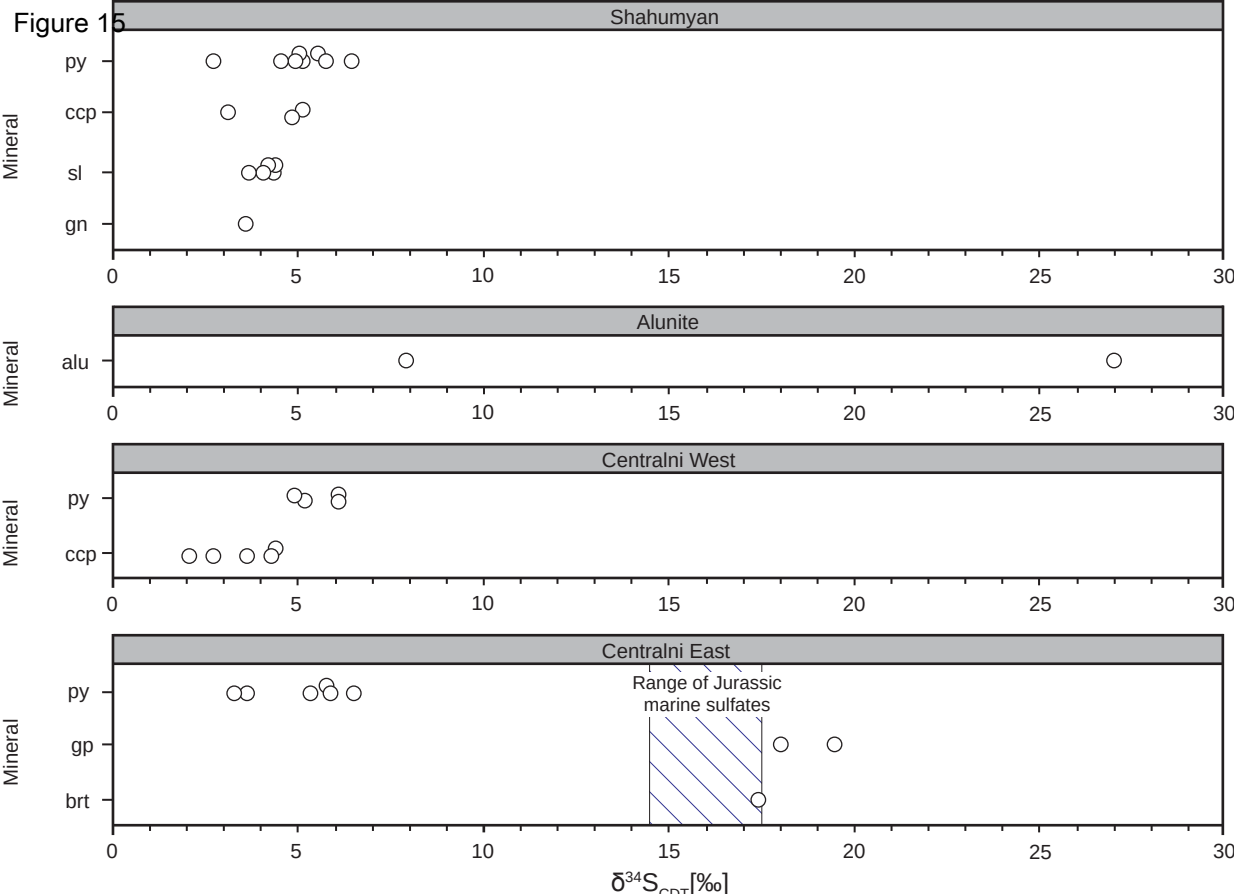
Shahumyan
Mineral
py
ccp
sl
gn
0
5
10
15
20
25
30
Alunite
Mineral
alu
Centralni West
Mineral
py
ccp
Centralni East
Mineral
py
gp
brt
Range of Jurassic
marine sulfates
δ34SCDT[‰]

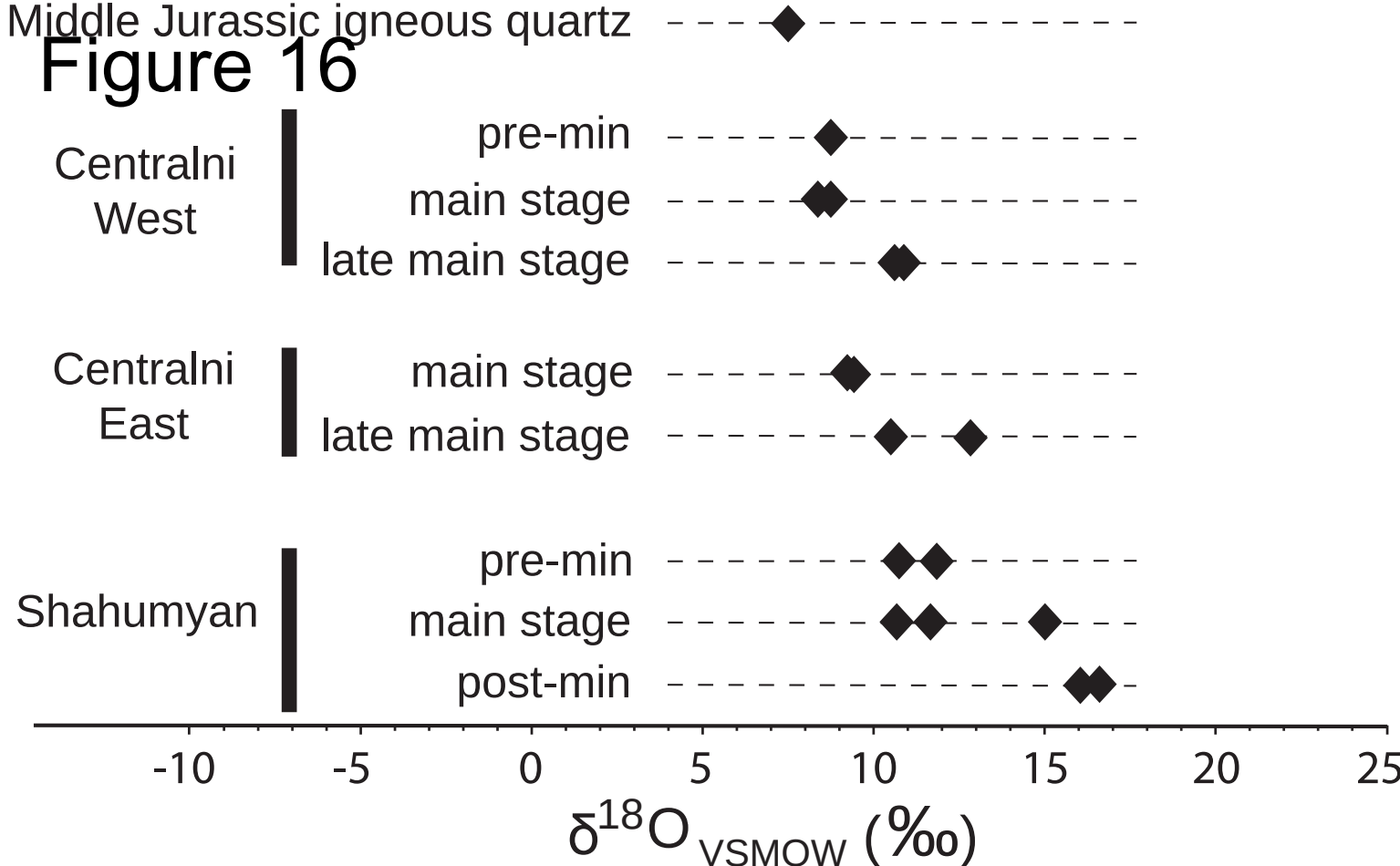
Middle Jurassic igneous quartz
Figure 16
Centralni West
pre-min
main stage
late main stage
Centralni East
main stage
late main stage
Shahumyan
pre-min
main stage
post-min
-10
-5
0
5
10
15
20
25
δ18O VSMOW (‰)

Figure 17

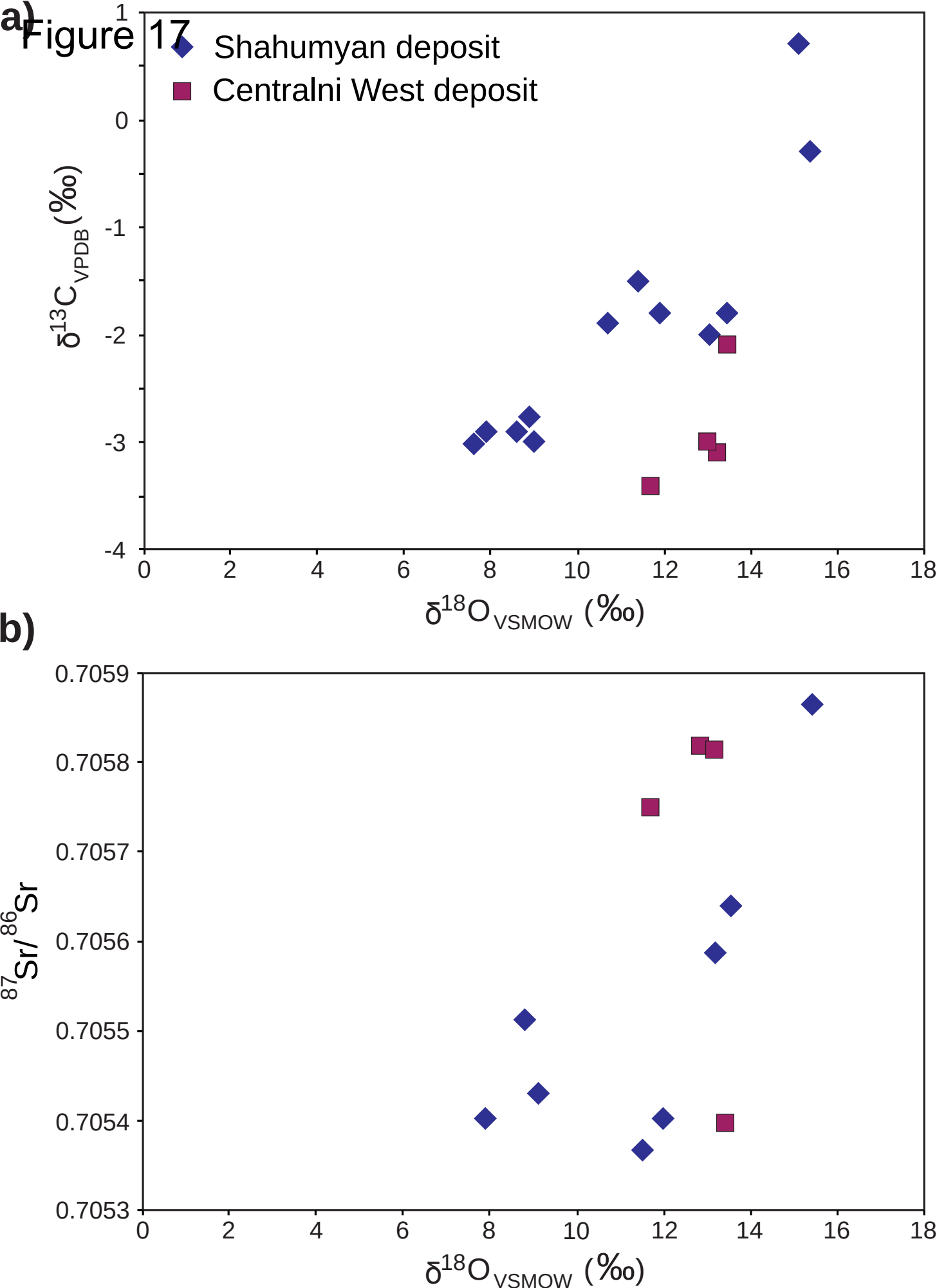
a)
Shahumyan deposit
Centralni West deposit
δ13CVPDB (‰)
δ18OVSMOW (‰)
1
0
-1
-2
-3
-4
0
2
4
6
8
10
12
14
16
18
b)
87Sr/86Sr
0.7059
0.7058
0.7057
0.7056
0.7055
0.7054
0.7053
δ18OVSMOW (‰)

Figure 18

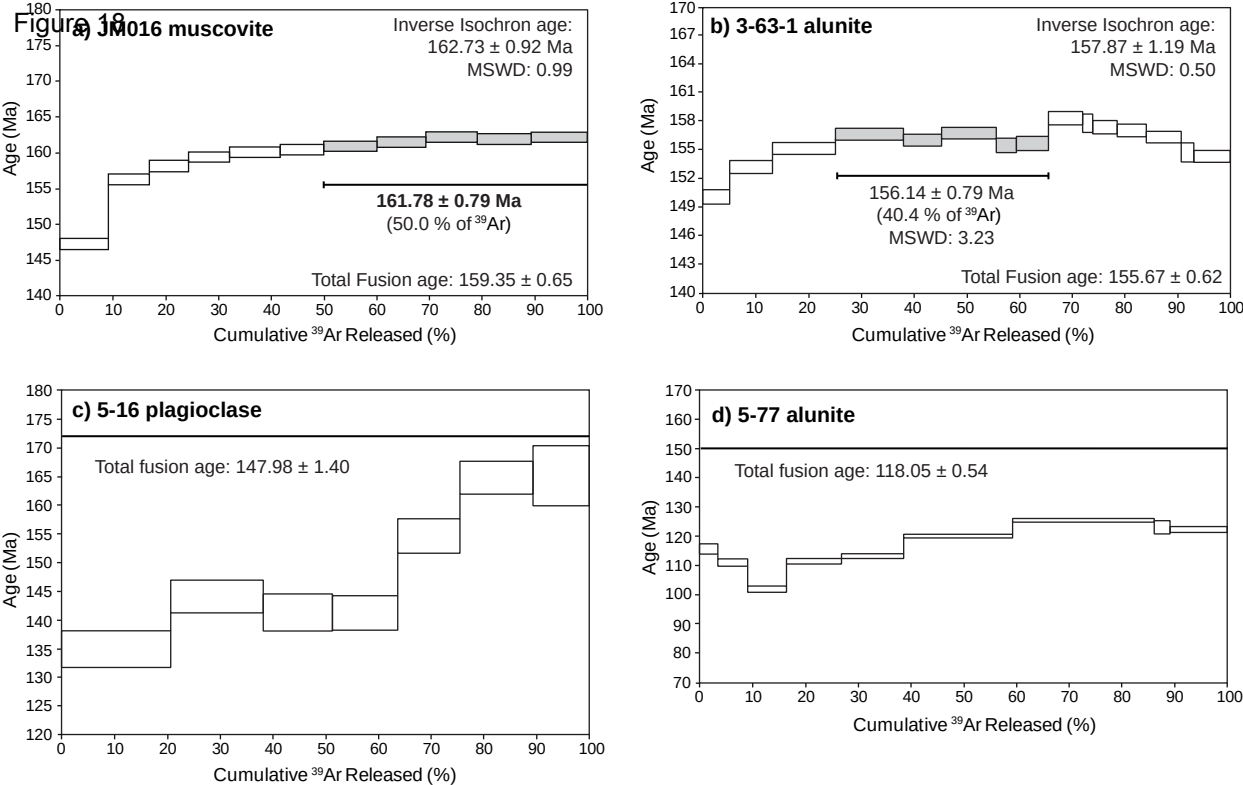
a) JM016 muscovite
Inverse Isochron age:
162.73 ± 0.92 Ma
MSWD: 0.99
161.78 ± 0.79 Ma
(50.0 % of 39Ar)
Total Fusion age: 159.35 ± 0.65
Age (Ma)
Cumulative 39Ar Released (%)
b) 3-63-1 alunite
Inverse Isochron age:
157.87 ± 1.19 Ma
MSWD: 0.50
156.14 ± 0.79 Ma
(40.4 % of 39Ar)
MSWD: 3.23
Total Fusion age: 155.67 ± 0.62
Age (Ma)
Cumulative 39Ar Released (%)
c) 5-16 plagioclase
Total fusion age: 147.98 ± 1.40
Age (Ma)
Cumulative 39Ar Released (%)
d) 5-77 alunite
Total fusion age: 118.05 ± 0.54
Age (Ma)
Cumulative 39Ar Released (%)

Figure 19

Centralni West

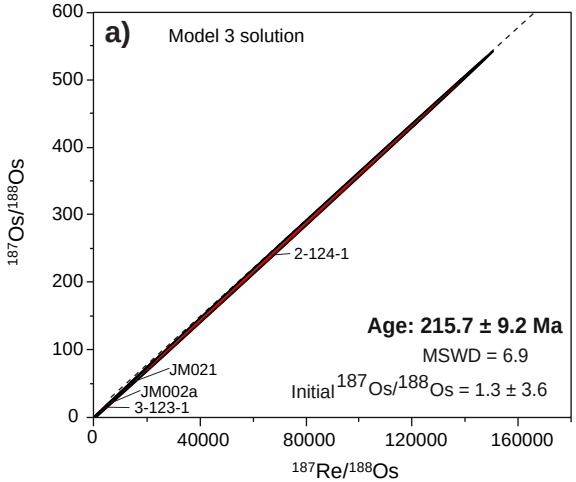

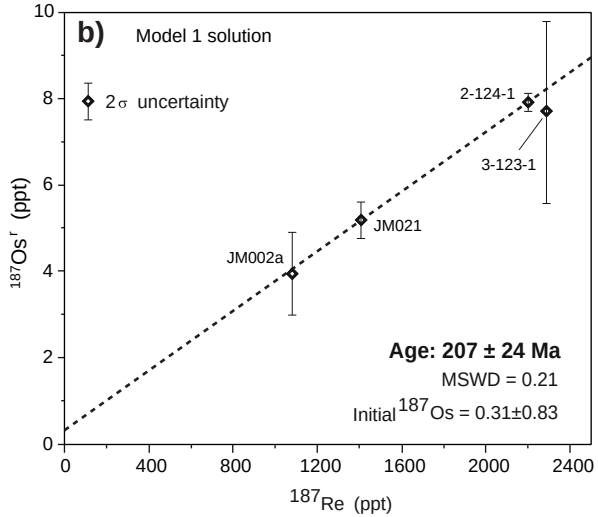

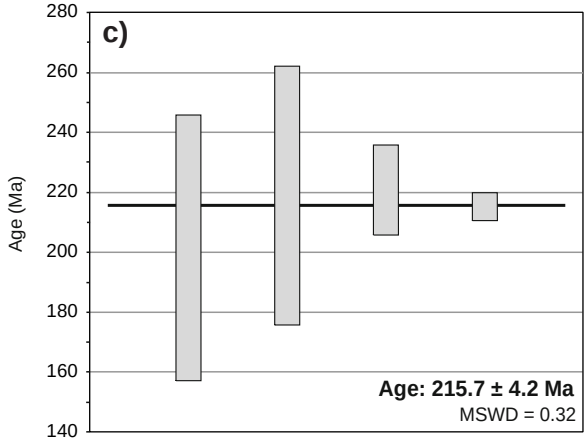

Centralni East

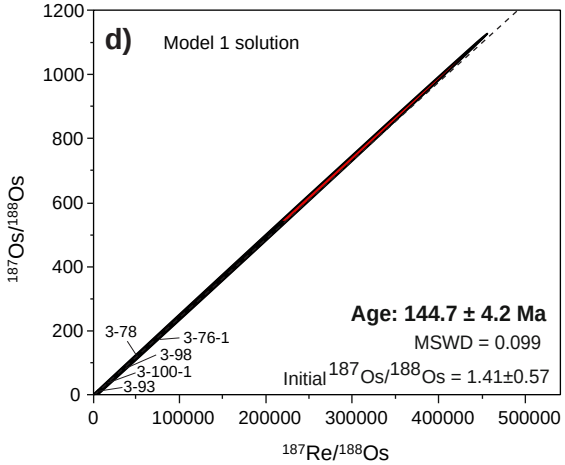

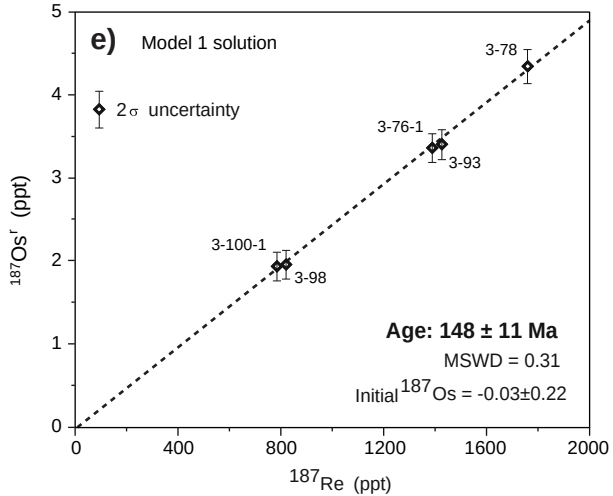

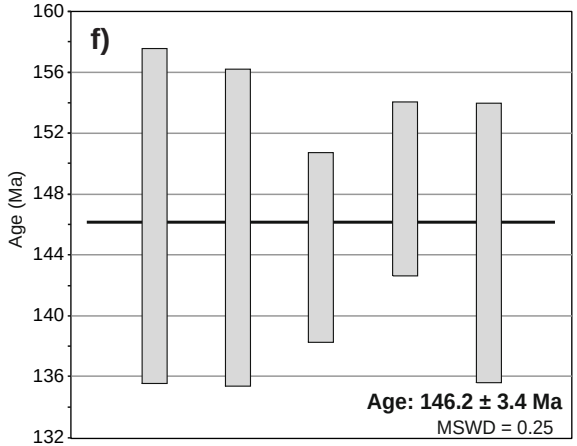

Figure 20

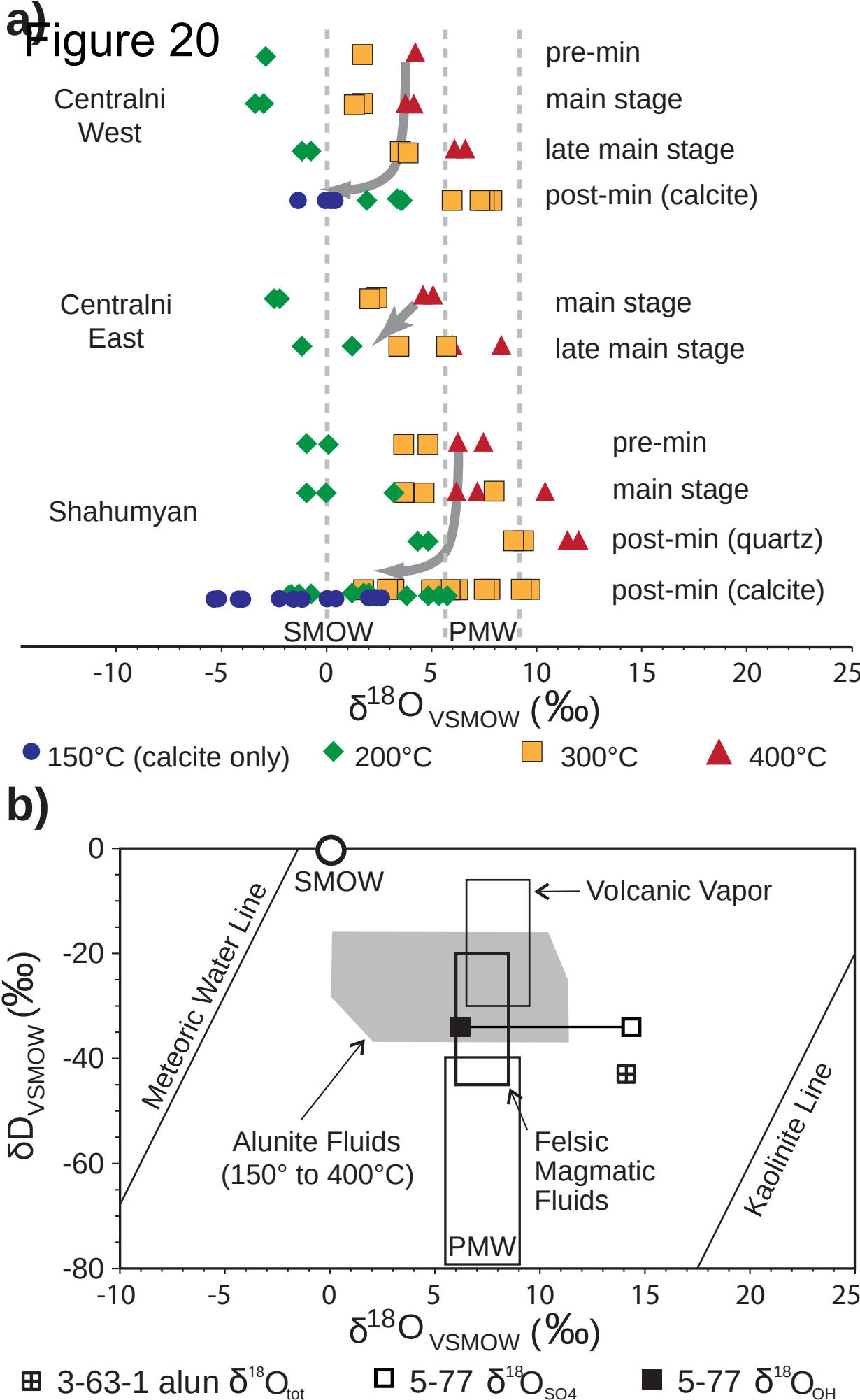
a)
Centralni West
pre-min
main stage
late main stage
post-min (calcite)
Centralni East
main stage
late main stage
Shahumyan
pre-min
main stage
post-min (quartz)
post-min (calcite)
SMOW
PMW
-10
-5
0
5
10
15
20
25
δ18O VSMOW (‰)
150°C (calcite only)
200°C
300°C
400°C
b)
SMOW
Volcanic Vapor
Meteoric Water Line
Kaolinite Line
Alunite Fluids
(150° to 400°C)
Felsic
Magmatic
Fluids
PMW
0
-20
-40
-60
-80
δDVSMOW (‰)
δ18O VSMOW (‰)
3-63-1 alun δ18Otot
5-77 δ18OSO4
5-77 δ18OOH

Figure 21 **Igneous intrusive and hydrothermal events in the Kapan district**

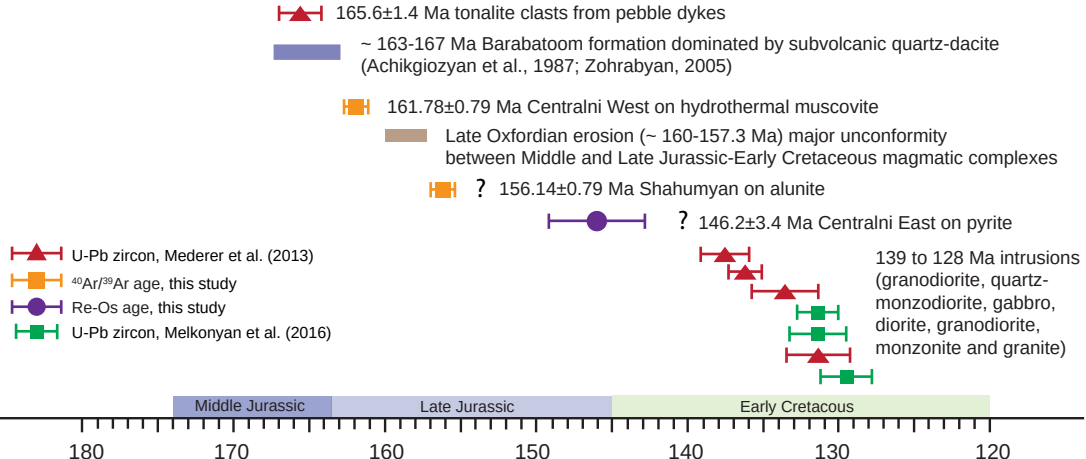

Figure 22

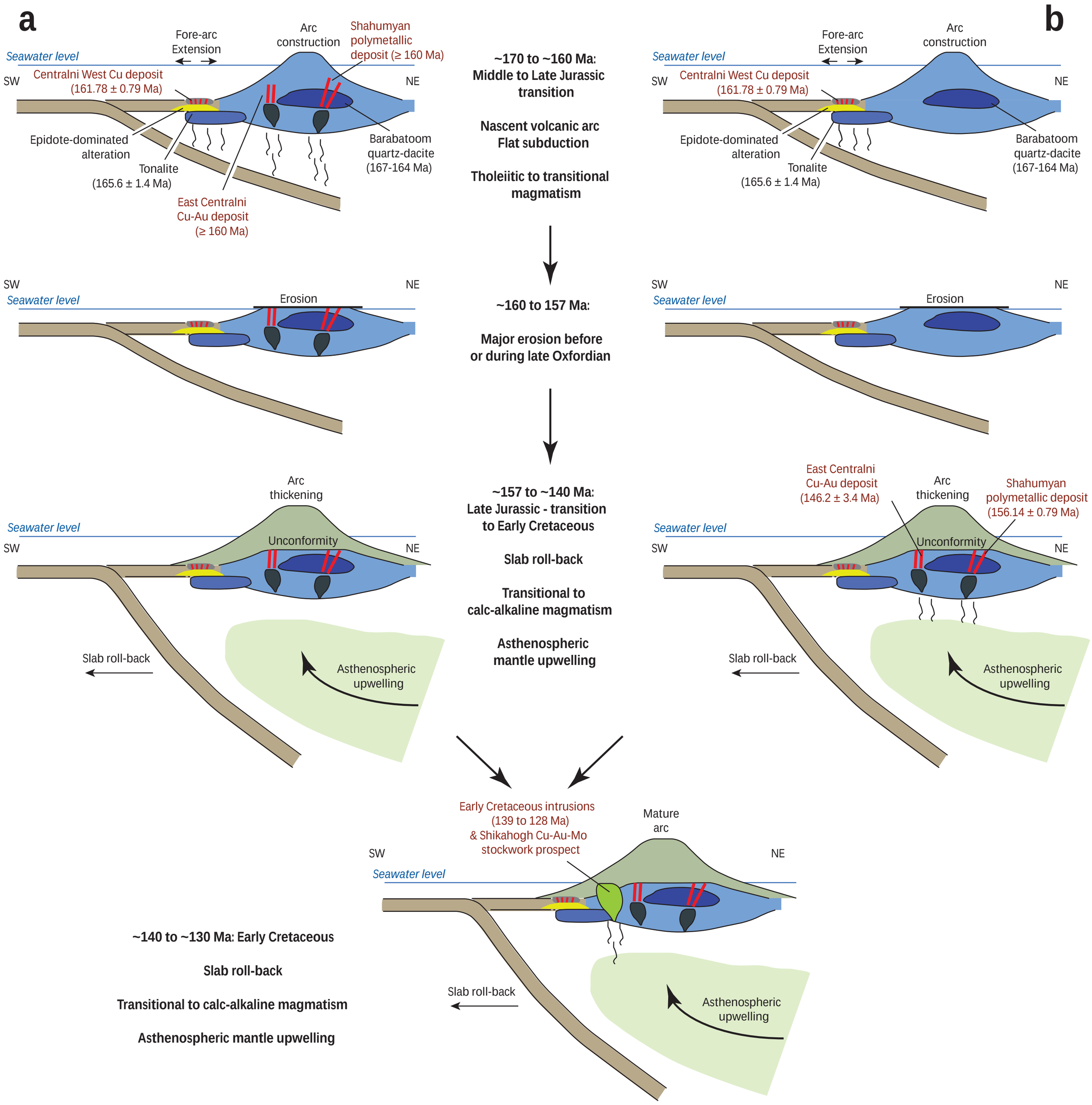
a
b
Seawater level
SW
NE
Fore-arc Extension
Arc construction
Shahumyan polymetallic deposit (≥ 160 Ma)
Centralni West Cu deposit (161.78 ± 0.79 Ma)
Epidote-dominated alteration
Tonalite (165.6 ± 1.4 Ma)
East Centralni Cu-Au deposit (≥ 160 Ma)
Barabatoom quartz-dacite (167-164 Ma)
~170 to ~160 Ma: Middle to Late Jurassic transition
Nascent volcanic arc
Flat subduction
Tholeiitic to transitional magmatism
Erosion
~160 to 157 Ma:
Major erosion before or during late Oxfordian
Arc thickening
Unconformity
East Centralni Cu-Au deposit (146.2 ± 3.4 Ma)
Shahumyan polymetallic deposit (156.14 ± 0.79 Ma)
~157 to ~140 Ma: Late Jurassic - transition to Early Cretaceous
Slab roll-back
Transitional to calc-alkaline magmatism
Asthenospheric mantle upwelling
Early Cretaceous intrusions (139 to 128 Ma) & Shikahogh Cu-Au-Mo stockwork prospect
Mature arc
~140 to ~130 Ma: Early Cretaceous
Slab roll-back
Transitional to calc-alkaline magmatism
Asthenospheric mantle upwelling

Table 1: Summary of main ore deposit characteristics in the Kapan district

Deposit name	Deposit type	Reserves-ore grade	Status	Age	Host-rock geology	Main ore mineralogy	Alteration	Orebody geometry
Centralni West	Cu sulfide-quartz veins	Estimated 30,000 t mined since 1843 @ 1.16% Cu (both Centralni deposits together)	Underground operation closed 2008	161.78 ± 0.79 Ma (Ar/Ar muscovite)	Middle Jurassic brecciated lava, hyalo-clastite, lava flows	Chalcopyrite, pyrite, and minor sphalerite, tennantite-tetrahedrite and galena	Chlorite, carbonate and epidote alteration. Sericite close to ore	EW-oriented veins
Centralni East	Cu-Au, sulfide stockwork and veins	Estimated 30,000 t mined since 1843 @ 1.16% Cu (both Centralni deposits together)	Underground and open pit abandoned in 2004	144.7 ± 4.2 Ma (Re-Os pyrite isochron)	Middle Jurassic andesite and quartz-dacite	Pyrite, colusite, tennantite-tetrahedrite, chalcopyrite and minor luzonite and galena	Silicification, residual quartz alteration and phyllic alteration	Stockwork in the upper part of the deposit, E-W striking veins at depth
Shahumyan	Polymetallic veins	2006–2011 production: 1.8 Mt @ 1.53 ppm Au, 29.8 ppm Ag, 0.24% Cu and 1.52% Zn. Estimated resources in early 2017: 15.0 Mt at 2.7 ppm Au, 48 ppm Ag and 0.5% Cu	Underground mining	156.14 ± 0.79 Ma (Ar/Ar alunite)	Middle Jurassic subvolcanic quartz-dacite	pyrite, chalcopyrite, spalerite, tennantite-tetrahedrite, galena, and minor arsenopyrite, enargite, digenite, bornite, chalcocite, native gold and tellurides	Phyllic and argillic alteration, advanced argillic (alunite) and poorly developed residual quartz alteration in the northeastern part of the deposit	Subvertical EW-oriented veins

Table 2: Lead isotopic data for sulfides and sulfates from the Centralni West, Centralni East and Shahumyan deposits

Sample	Mineral	$^{206/204}Pb$	$^{207/204}Pb$	$^{208/204}Pb$	Sample	Mineral	$^{206/204}Pb$	$^{207/204}Pb$	$^{208/204}Pb$
Centralni West deposit					**Shahumyan deposit**				
DC043	py	18.296	15.602	38.377	JM005	gn	18.248	15.585	38.329
DC043	ccp	18.300	15.604	38.377	JM006	gn	18.273	15.601	38.385
DC-2-123-1	py	18.297	15.598	38.366	3-26	gn	18.238	15.572	38.285
DC-2-123-1	ccp	18.308	15.604	38.387	5-77	alu	18.172	15.606	38.165
Centralni East deposit					3-63-1	alu	18.203	15.608	38.204
3-98	py	18.317	15.613	38.407					
3-100-1	py	18.267	15.583	38.315					

Abbreviations: alu = alunite, ccp = chalcopyrite, gn = galena, py = pyrite

Table 3: Oxygen, carbon, strontium and hydrogen isotopic composition of quartz, calcite, barite and alunite. The isotopic composition of the fluid in equilibrium with the minerals was calculated according to the equations of Zheng (1993) in the case of quartz, Zheng (1999) in the case of calcite and barite and Stoffregen et al. (1994) in the case of alunite. $\delta^{18}O$ and δD are reported relative to VSMOW and δ13C relative to VPDB. Abbreviations: alu = alunite, brt = barite, cal = calcite, qz = quartz.

Part 1: δ18O in igneous and hydrothermal quartz

Sample	Stage	Mineral	$\delta^{18}O$ (‰)	$\delta^{18}O_{H2O}$ 400 °C	300 °C	200 °C
Middle Jurassic igneous quartz (Barabatoom)						
5-16	igneous	qz	7.5			
Centralni West deposit						
DC043	pre-min	qz	8.7	4.1	1.6	-3.0
DC-2-124-1	main stage	qz	8.3	3.8	1.3	-3.3
DC-2-125	main stage	qz	8.6	4.0	1.5	-3.1
JM017	late main stage	qz	10.9	6.4	3.8	-0.8
JM24b	late main stage	qz	10.5	6.0	3.5	-1.1
Centralni East deposit						
OP-3-76	main stage	qz	9.1	4.6	2.0	-2.6
OP001	main stage	qz	9.3	4.7	2.2	-2.4
OP-3-98	late main stage	qz	10.4	5.9	3.4	-1.2
OP-3-98-1	late main stage	qz	12.7	8.1	5.6	1.0
Shahumyan deposit						
3-26-2	pre-min	qz	11.7	7.2	4.7	0.1
3-111	pre-min	qz	10.7	6.2	3.6	-1.0
3-35	main stage	qz	14.8	10.3	7.8	3.2
2-69	main stage	qz	11.6	7.1	4.6	-0.1
2-67	main stage	qz	10.6	6.1	3.6	-1.0
2-114-1	post-min	qz	15.9	11.4	8.9	4.3
5-47	post-min	qz	16.4	11.9	9.4	4.8
3-142	post-min	qz	16.0	11.5	9.0	4.3

Part 2: $\delta^{18}O$, $\delta^{13}C$ and $^{87}Sr/^{86}Sr$ in hydrothermal calcite

Sample	Stage	Mineral	$\delta^{18}O$ ‰	$\delta^{13}C$ (‰)	$^{87}Sr/^{86}Sr$	$\delta^{18}O_{H2O}$ 300 °C	250 °C	200 °C	150 °C
Centralni West deposit									
DC-2-124-1	post-min	cal	13.2	-3.1	0.705815	7.4	5.7	3.4	0.1
DC-2-125	post-min	cal	13.0	-3.0	0.705818	7.2	5.5	3.2	-0.1
JM24	post-min	cal	11.7	-3.4	0.705749	5.9	4.2	1.9	-1.4
JM017	post-min	cal	13.4	-2.1	0.705395	7.6	6.0	3.6	0.3
Shahumyan deposit									
3-142	post-min	cal	13.5	-1.8	0.705640	7.7	6.0	3.7	0.4
2-69	post-min	cal	13.1	-2.0	0.705586	7.3	5.6	3.3	0.0
3-111	post-min	cal	11.9	-1.8	0.705401	6.1	4.4	2.1	-1.2
3-26-1	post-min	cal	7.9	-2.9	0.705403	2.1	0.4	-1.9	-5.2
3-143	post-min	cal	11.4	-1.5	0.705367	5.6	3.9	1.6	-1.7
2-114-3	post-min	cal	8.8	-2.8	0.705515	3.0	1.3	-1.0	-4.3
2-67	post-min	cal	9.0	-3.0	0.705429	3.2	1.5	-0.8	-4.1
5-47	post-min	cal	15.4	-0.3	0.705864	9.6	7.9	5.6	2.3
5-71	post-min	cal	7.7	-3.0		1.9	0.2	-2.1	-5.4
2-114-1	post-min	cal	15.1	0.7		9.3	7.6	5.3	2.0
3-149	post-min	cal	8.8	-2.9		3.0	1.3	-1.0	-4.3
3-26-2	post-min	cal	10.7	-1.9		4.9	3.2	0.9	-2.4

Part 3: δ18O and δD in sulfates

Sample	Stage	Mineral	$\delta^{18}O$ ‰	$\delta^{18}O_{SO4}$ (‰)	$\delta^{18}O_{OH}$ (‰)	δD (‰)	$\delta^{18}O_{H2O}$ 400 °C	300 °C	200 °C	δD_{H2O} 400 °C	300 °C	200 °C
Centralni East deposit												
OP-3-98-1	main stage	brt	10.5				8.0	6.2	2.6			
Shahumyan deposit												
5-77		alu	10.9	14.4	6.2	-34±2	10.5	7.9	3.5	-16	-24	-28
3-63-1		alu	14.1			-43±2	11.4	9.1	5.2	-25	-33	-37

Table 4: δ34S composition of sulfides and sulfates from the Kapan district and calculated temperature estimates from sulfide-sulfide and sulfide-sulfate pairs

		$\delta^{34}S$ (‰ CDT)							
Sample	stage	pyrite	chalcopyrite	sphalerite	galena	barite	gypsum	alunite	Temperature (°C)
Centralni West Deposit									
2-123-1	main stage	4.9	4.3						592
2-125	main stage	5.2	2.0						107
JM024b	main stage	6.1	2.7						93
DC043	main stage	6.1							
JM014	main stage		3.6						
JM016	main stage		4.4						
Centralni East Deposit									
3-100-1	main stage	5.9							
3-76-1	main stage	5.8							
3-80	main stage	3.6					19.5		357
3-98-1	main stage	3.3				17.4			395
3-97	late main stage	5.3							
3-98	late main stage	6.5							
3-78-1	late fault						18.0		
Shahumyan									
3-142	main stage	4.9	3.1	4.2					381[1], 226[2], 96[3]
3-24	main stage	6.4							
3-36	main stage	5.8							
DC057	main stage	5.1		4.3					
DC064a	main stage	4.5							
JM009/1	main stage	5.5		4.3					
2-69	main stage		4.8	3.7					
5-83	main stage			4.1					
DC030	main stage		5.1						
5-77	main stage							7.9	
3-63-1	main stage							27.0	
JM006	late main stage				3.6				
DC-2-78-1	late main stage	2.5							
JM009/2	late main stage	5.1							

Temperatures for the respective sulfide-sulfate pairs were calculated using the equations by Ohmoto and Lasaga (1982) whereas for sulfide-sulfide pairs the equations by Kajiwara and Krouse (1971) were used. The calculated temperatures are questionable due to a high spread within single samples and stages. See text for details.
[1]=pyrite-sphalerite, [2]=pyrite-chalcopyrite, [3]=sphalerite-chalcopyrite.

Table 5: Summary of $^{40}Ar/^{39}Ar$ step-heating ages from the Kapan district

Sample	Mineral	Weighted Plateau age (Ma± 2σ)	% of ^{39}Ar in plateau age	Total Fusion age (Ma ± 2σ)	Inverse isochron age (Ma ± 2σ)	Inverse isochron derived MSWD	Inverse isochron $^{40}Ar/^{39}Ar$ ratio of intercept (± 2σ)
Part 1: istopic ratios and ages							
JM016	muscovite	161.78 ± 0.79	50.0	159.35 ± 0.65	162.73 ± 0.92	0.99	-143.8 ± 149.7
5-16	plagioclase	-	-	147.98 ± 1.40	-	-	-
3-63-1	alunite	**156.14 ± 0.79**	40.4	155.67 ± 0.62	157.87 ± 1.19	0.50	128.8 ± 85.2
5-77	alunite	-	-	118.05 ± 0.54	-	-	-

Part 2: sample location and weight

Sample	Mass (mg)	Sample type and descritption	UTM(E)	UTM(N)
JM016	9.2	Centralni West, vein 12, level 885; altered host rock + mineralization		
5-16	6.7	Shahumyan deposit, propylitically altered quartz-dacite host rock	624297	4340508
3-63-1	6.3	Shahumyan deposit, magmatic-hydrothermal disseminated alunite	624383	4342250
5-77	7.0	Shahumyan deposit, magmatic-steam alunite from banded veins	624415	4342219

Notes: The plateau ages were calculated according to the criteria of Dalrymple and Lanphere (1974); the age in bold is calculated on the basis of less than 50% total released $^{40}Ar/^{39}Ar$.

Table 6: $^{40}Ar/^{39}Ar$ analysis of muscovite, alunite and plagioclase samples from the Kapan district

Incremental step-heating results, JM016 muscovite, J=3.8421E-3±7.7E-6 (2σ)

Step	$^{40}Ar/^{39}Ar$	±1σ	$^{37}Ar/^{39}Ar$	±1σ	$^{36}Ar/^{39}Ar$	±1σ	$^{40}Ar^{*}/^{39}Ar_{k}$	±1σ	$^{40}Ar(mol)$	$^{40}Ar^{*}$ (%)	$^{39}Ar_{K}$ (%)	K/Ca	±2σ	Age (Ma)	±2σ
1	23.24365	0.04679	0.00241	0.00050	0.00369	0.00012	22.151461	0.05738	1.260E-14	95.30	9.14	178.366	74.235	147.36	0.73
2	24.12350	0.04870	0.00172	0.00037	0.00191	0.00008	23.559136	0.05358	1.103E-14	97.66	7.71	250.097	106.460	156.33	0.68
3	24.31916	0.04921	0.00030	0.00035	0.00154	0.00009	23.863426	0.05449	1.081E-14	98.13	7.49	1451.876	3470.100	158.26	0.69
4	24.34986	0.04908	0.00000	0.00046	0.00100	0.00010	24.054225	0.05663	1.098E-14	98.79	7.60	571.718	687.650	159.47	0.72
5	24.38412	0.04938	0.00001	0.00034	0.00074	0.00008	24.163380	0.05446	1.408E-14	99.09	9.73	571.718	687.650	160.16	0.69
6	24.44871	0.04938	0.00001	0.00041	0.00079	0.00008	24.213691	0.05421	1.210E-14	99.04	8.34	571.718	687.650	160.48	0.69
7	24.46273	0.04923	0.00087	0.00033	0.00059	0.00007	24.286806	0.05335	1.470E-14	99.28	10.13	495.867	378.261	**160.95**	**0.68**
8	24.50295	0.04933	0.00217	0.00036	0.00039	0.00007	24.385441	0.05365	1.341E-14	99.52	9.23	198.247	66.582	**161.57**	**0.68**
9	24.53200	0.04942	0.00638	0.00041	0.00015	0.00009	24.488647	0.05595	1.408E-14	99.82	9.68	67.430	8.614	**162.22**	**0.71**
10	24.51018	0.04931	0.00500	0.00036	0.00020	0.00010	24.450991	0.05680	1.494E-14	99.76	10.28	85.956	12.302	**161.99**	**0.72**
11	24.59468	0.04937	0.00439	0.00034	0.00036	0.00007	24.489122	0.05359	1.558E-14	99.57	10.68	97.977	15.036	**162.23**	**0.68**
Weighted Plateau Age:												50.0 % of ^{39}Ar		161.78	0.79
Total Fusion Age:														159.35	0.65

Incremental step-heating results, 3-63-1 alunite, J=3.8421E-3±7.7E-6 (2σ)

Step	$^{40}Ar/^{39}Ar$	±1σ	$^{37}Ar/^{39}Ar$	±1σ	$^{36}Ar/^{39}Ar$	±1σ	$^{40}Ar^{*}/^{39}Ar_{k}$	±1σ	$^{40}Ar(mol)$	$^{40}Ar^{*}$ (%)	$^{39}Ar_{K}$ (%)	K/Ca	±2σ	Age (Ma)	±2σ
1	24.65071	0.04990	0.00001	0.00056	0.00701	0.00012	22.577447	0.05738	1.266E-14	91.59	4.85	2305.801	12474.739	150.08	0.73
2	24.62684	0.04948	0.00001	0.00030	0.00529	0.00007	23.061206	0.05099	2.124E-14	93.64	8.14	2305.801	12474.739	153.16	0.65
3	23.87873	0.04788	0.00017	0.00017	0.00172	0.00004	23.368104	0.04808	3.017E-14	97.86	11.93	2508.098	4958.492	155.11	0.61
4	24.01461	0.04817	0.00001	0.00015	0.00134	0.00003	23.616654	0.04827	3.297E-14	98.34	12.96	2305.801	12474.739	**156.69**	**0.61**
5	24.03299	0.04830	0.00621	0.00023	0.00181	0.00006	23.498795	0.05002	1.840E-14	97.78	7.23	69.285	5.096	**155.94**	**0.64**
6	23.90468	0.04798	0.00962	0.00026	0.00097	0.00004	23.617178	0.04853	2.606E-14	98.80	10.29	44.717	2.462	**156.69**	**0.62**
7	24.04333	0.04864	0.00884	0.00055	0.00213	0.00011	23.413265	0.05823	1.007E-14	97.38	3.96	48.645	6.021	**155.40**	**0.74**
8	24.10546	0.04858	0.00001	0.00031	0.00219	0.00007	23.456530	0.05133	1.528E-14	97.31	5.98	1128.891	2171.447	**155.67**	**0.65**
9	23.97262	0.04834	0.00143	0.00032	0.00035	0.00007	23.868498	0.05197	1.640E-14	99.57	6.46	300.880	133.485	158.29	0.66
10	24.38945	0.05060	0.01994	0.00118	0.00207	0.00020	23.778216	0.07702	5.018E-15	97.49	1.94	21.569	2.547	157.72	0.98
11	24.07376	0.04904	0.00401	0.00044	0.00118	0.00010	23.723665	0.05643	1.196E-14	98.55	4.69	107.306	23.554	157.37	0.72
12	24.05868	0.04850	0.00318	0.00032	0.00135	0.00007	23.657668	0.05168	1.371E-14	98.33	5.38	135.347	26.920	156.95	0.66
13	24.20384	0.04862	0.00319	0.00029	0.00220	0.00007	23.552697	0.05206	1.715E-14	97.31	6.69	134.677	24.815	156.29	0.66
14	23.99601	0.04989	0.00914	0.00085	0.00236	0.00020	23.297588	0.07562	5.974E-15	97.09	2.35	47.056	8.727	154.66	0.96
15	24.02621	0.04828	0.00151	0.00032	0.00268	0.00008	23.234819	0.05174	1.755E-14	96.71	6.89	284.179	119.117	154.26	0.66
Weighted Plateau Age:												40.4 % of ^{39}Ar		156.14	0.79
Total Fusion Age:														155.67	0.62

Continuation of Table 6: $^{40}Ar/^{39}Ar$ analysis of muscovite, alunite and plagioclase samples from the Kapan district

Incremental step-heating results, 5-16 plagioclase, J=3.8421E-3±7.7E-6 (2σ)

Step	$^{40}Ar/^{39}Ar$	±1σ	$^{37}Ar/^{39}Ar$	±1σ	$^{36}Ar/^{39}Ar$	±1σ	$^{40}Ar^{*}/^{39}Ar_{k}$	±1σ	$^{40}Ar(mol)$	$^{40}Ar^{*}$ (%)	$^{39}Ar_{K}$ (%)	K/Ca	±2σ	Age (Ma)	±2σ
1	45.00105	0.11221	0.76426	0.01257	0.08406	0.00087	20.230793	0.25644	5.110E-15	44.93	20.55	0.562	0.019	135.05	3.30
2	37.88368	0.11030	1.97307	0.03221	0.05557	0.00075	21.645625	0.22930	3.679E-15	57.06	17.56	0.218	0.007	144.12	2.93
3	36.37663	0.10522	3.96870	0.06470	0.05251	0.00085	21.224543	0.25788	2.622E-15	58.19	13.01	0.108	0.004	141.43	3.31
4	35.26637	0.12548	5.54169	0.09100	0.04932	0.00076	21.202082	0.23661	2.433E-15	59.90	12.44	0.077	0.003	141.28	3.03
5	34.20395	0.16748	6.71755	0.11240	0.03904	0.00068	23.296247	0.23201	2.241E-15	67.80	11.81	0.064	0.002	154.65	2.95
6	35.02031	0.17684	7.49173	0.12547	0.03661	0.00061	24.910016	0.22149	2.706E-15	70.77	13.92	0.057	0.002	164.89	2.80
7	35.02763	0.29006	9.35278	0.17455	0.03709	0.00117	24.954534	0.41698	2.085E-15	70.79	10.71	0.046	0.002	165.17	5.27
Total Fusion Age:														147.98	1.40

Incremental step-heating results, 5-77 alunite, J=3.8421E-3±7.7E-6 (2σ)

Step	$^{40}Ar/^{39}Ar$	±1σ	$^{37}Ar/^{39}Ar$	±1σ	$^{36}Ar/^{39}Ar$	±1σ	$^{40}Ar^{*}/^{39}Ar_{k}$	±1σ	$^{40}Ar(mol)$	$^{40}Ar^{*}$ (%)	$^{39}Ar_{K}$ (%)	K/Ca	±2σ	Age (Ma)	±2σ
1	20.95084	0.05322	0.03246	0.00219	0.01265	0.00043	17.213619	0.13499	1.968E-15	82.16	3.31	13.247	1.789	115.54	1.76
2	19.22030	0.04262	0.04319	0.00206	0.00923	0.00028	16.495605	0.08902	3.152E-15	85.82	5.78	9.957	0.948	110.86	1.16
3	18.98454	0.03928	0.05971	0.00189	0.01315	0.00023	15.104432	0.07384	3.962E-15	79.56	7.36	7.201	0.456	101.77	0.97
4	20.53557	0.04261	0.05610	0.00138	0.01338	0.00021	16.586270	0.07157	5.999E-15	80.77	10.30	7.665	0.376	111.45	0.93
5	20.79022	0.04201	0.05702	0.00104	0.01344	0.00016	16.821817	0.05683	7.007E-15	80.91	11.89	7.540	0.276	112.99	0.74
6	21.21803	0.04263	0.04131	0.00075	0.01126	0.00012	17.893580	0.05107	1.245E-14	84.33	20.69	10.409	0.377	119.95	0.66
7	19.93594	0.04016	0.03394	0.00062	0.00408	0.00008	18.731508	0.04438	1.517E-14	93.96	26.84	12.668	0.462	125.38	0.57
8	21.49421	0.06671	0.08230	0.00410	0.01065	0.00051	18.354976	0.16197	1.806E-15	85.39	2.96	5.224	0.521	122.94	2.10
9	20.01486	0.04107	0.07861	0.00137	0.00600	0.00017	18.247632	0.06292	6.165E-15	91.17	10.86	5.469	0.191	122.25	0.82
Total Fusion Age:														118.05	0.54

Table 7: Re-Os isotope data for pyrite from the Kapan mining district, Armenia

Sample number	Total Re (ppb)	±	^{187}Re (ppt)	±	Total Os (ppt)	±	^{187}Os^{r} (ppt)	±
Part 1: concentration data								
Centralni West								
2-123-1	3.64	0.01	2288.7	8.6	11.9	0.8	7.7	1.7
JM002a	1.72	0.01	1081.1	4.1	5.9	1.1	4.0	0.8
JM021	2.24	0.01	1407.9	5.3	6.0	3.2	5.2	0.3
2-124-1	3.50	0.01	2201.6	8.3	8.2	11.3	7.9	0.2
Centralni East								
3-100-1	1.26	0.01	792.4	7.2	2.3	6.4	1.9	0.1
3-98	1.28	0.01	806.3	6.9	2.2	11.9	2.0	0.1
3-76-1	2.22	0.01	1394.8	8.3	3.5	25.7	3.4	0.1
3-78	2.79	0.02	1753.7	9.6	4.7	18.3	4.3	0.2
3-93	2.24	0.01	1410.6	8.0	6.1	1.7	3.4	0.2
Part 2: isotopic ratios and model ages								
Sample	% ^{187}Os^{r}	^{187}Re/^{188}Os	±	^{187}Os/^{188}Os	±	rho	Model age Ma	±
Centralni West								
2-123-1	92.5	4818.3	306.5	17.5	1.1	0.989	201.7	44.8
JM002a	93.2	5010.1	919.9	19.6	3.6	0.998	219.3	43.2
JM021	97.5	15136.4	6364.6	57.1	24.0	>0.999	220.9	14.5
2-124-1	99.4	67386.1	67598.8	243.5	244.3	>0.999	215.3	4.6
Centralni East								
3-100-1	96.4	17736.0	39773.1	44.8	100.5	>0.999	146.6	10.1
3-98	96.5	35730.8	151040.4	88.3	373.2	>0.999	145.8	10.3
3-76-1	98.0	74853.9	400686.9	181.8	973.4	>0.999	144.5	6.3
3-78	97.8	47215.8	139079.7	118.3	348.4	>0.999	148.4	5.8
3-93	88.4	4623.4	1435.5	12.6	3.9	>0.999	144.6	9.4
Part 3: sample locations and weights								
Sample	Mass (g)	Sample type			UTM (E)	UTM(N)		
Centralni West								
2-123-1	0.615	drill core, 120 m depth			619072	4343859		
JM002a	0.404	underground vein 12, Level 885						
JM021	0.405	underground vein 24, level 845						
2-124-1	0.473	drill core, 222 m depth			619072	4343859		
Centralni East								
3-100-1	0.514	open pit			620343	4343893		
3-98	0.495	open pit			620355	4343915		
3-76-1	0.435	open pit			620330	4343855		
3-78	0.405	open pit			620352	4343908		
3-93	0.535	open pit			620315	4343771		

Notes: All samples from UTM zone 38S.